

UNIVERSITY OF CAPE TOWN

THESIS PRESENTED FOR THE DEGREE OF MASTER OF  
SCIENCE

IN THE DEPARTMENT OF ASTRONOMY

---

# DETECTING THE MAGNETIC COSMIC WEB THROUGH DEEP RADIO POLARIZATION IMAGING

---

*Author:*

Lauren S. BURNHAM-KING

*Supervisors:*

Prof R. TAYLOR

Dr K. VAN DER HEYDEN

2017



# Plagiarism Declaration

*I, Lauren Burnham-King, know the meaning of plagiarism and declare that all of the work in the document, save for that which is properly acknowledged, is my own.*

Lauren Burnham-King

---

*Signature*

---

*Date*

# Abstract

The polarisation of radio emission is one of the most powerful probes of magnetic fields in the cosmos. Faraday rotation of polarized radiation provides one of the methods to observe magnetic fields. Measuring the rotation of the polarisation angle of radiation from an extragalactic source over a broad radio bandwidth allows us to infer the properties of the magnetic fields that the radiation passed through on the path to the observer. In the last few decades, the presence of structure in the matter distribution of the universe has been observed. It remains an open question whether there are magnetic fields associated with this large-scale structure. Large-scale universe simulations allow us to investigate the effect of extragalactic magnetic fields on the spatial distribution of Rotation Measure (RM) of radio sources that will be detected in deep radio images with MeerKAT. We constructed lightcones out to  $z = 1$  from large-scale universe simulations as a base for our model and assemble a routine to trace large scale structures, attach magnetic fields to the structure and construct RM observations. The aim is to explore whether deep MeerKAT continuum observations will be able to detect magnetic fields associated with large-scale structure (the so-called magnetic cosmic web).

# Acknowledgements

Firstly, thank you to my supervisors for your time, energy and input. Thank you for giving me all the tools that I needed to complete this project and for giving me opportunities to travel and meet people whom I could learn from. Russ, thank you for all of your guidance and for pointing me in the right directions. Kurt, thank you for being a sounding board whenever I hit walls or got lost.

This project was made up of many different pieces, and this led me to seek input from many sources. On the computational side, thank you to Romeel Davé for the use of the MUFASA simulations as well as for being available to guide me through using them. Thank you to Matthew Cawood for teaching me how to use his pencil beam routine and helping me troubleshoot in the initial stages. Thank you to Sean February, my contact at the CHPC, for the patience in helping me learn about the advanced computing that I needed as well as for patiently answering all of my questions.

Thank you to Luke Chamandy for your help in teaching me about magnetic fields and giving so much time to talk me through the theory. Thank you to Rainer Beck for the input on galaxy and halo magnetic fields which drastically simplified some of my challenges. Thank you to Franco Vazza who helped me to understand how magnetic fields behave in the Large-Scale Structure. Lastly, a big thanks to Jeroen Stil who taught me everything I needed to know about structure functions and who made so much time to answer every question I had.

I need to also thank my parents and husband for your support, both in helping me to stay motivated and for proofreading my work and giving such valuable feedback. I am also deeply grateful to my fellow students and friends at UCT for helping me through stressful times, supporting me in my challenges, and generally lightening the mood in the slow-moving eternities.

Finally, thank you to the SKA who funded this project and made it possible to me to get the equipment and travel made this work so much better and to the Centre for High Performance Computing (CHPC), South Africa, for providing computational resources to this research project.

# Contents

|          |  |           |
|----------|--|-----------|
| <b>1</b> | <b>Introduction</b>  | <b>1</b>  |
| 1.1      | The Cosmic Web . . . . .   | 1         |
| 1.2      | Cosmic magnetism . . . . .   | 4         |
| 1.2.1    | Magnetism in Galaxies . . . . .  | 5         |
| 1.2.2    | Magnetism in Clusters . . . . .  | 5         |
| 1.2.3    | Magnetism in LSS . . . . .   | 6         |
| 1.3      | Methods for Observing Magnetic Fields . . . . .  | 6         |
| 1.3.1    | Polarisation . . . . .   | 6         |
| 1.3.2    | Synchrotron Radiation . . . . .  | 7         |
| 1.3.3    | Faraday Rotation . . . . .   | 7         |
| 1.4      | Polarisation Surveys . . . . .   | 10        |
| 1.5      | MeerKAT and SKA . . . . .  | 11        |
| 1.6      | Outline of Thesis . . . . .  | 11        |
| <b>2</b> | <b>Tools of the Trade</b>  | <b>13</b> |
| 2.1      | Simulations . . . . .  | 13        |
| 2.2      | MUFASA and CAESAR . . . . .  | 15        |
| 2.3      | Radio Sources . . . . .  | 17        |
| 2.4      | Ray Tracing . . . . .  | 18        |
| 2.5      | Choosing the Magnetic Field Parameters . . . . .   | 18        |
| 2.6      | Initial Setup and Project Overview . . . . .   | 21        |
| <b>3</b> | <b>Radio Emission from Galaxies</b>  | <b>24</b> |
| 3.1      | Sources of Radio Emission . . . . .  | 24        |
| 3.2      | Assigning Radio Flux for Star Forming Galaxies . . . . .                                 | 26        |
| 3.3      | Identifying AGNs and Assigning Flux . . . . .  | 27        |
| 3.4      | Combining Flux from SFGs and AGN host galaxies . . . . .                                 | 29        |
| 3.5      | Observational Error on RM Measurements . . . . .   | 30        |
| <b>4</b> | <b>The Magnetic Field Parameter Space</b>  | <b>34</b> |
| 4.1      | Constructing and Ray Tracing the Pencil Beams . . . . .                                  | 34        |
| 4.1.1    | Ray Tracing Methods . . . . .  | 36        |
| 4.1.2    | Comparison of Methods to Trace Along the Ray . . . . .                                   | 37        |
| 4.2      | Intersections of the Light Rays in the Simulation . . . . .                              | 39        |
| 4.3      | Analysing the Rotation Measures . . . . .  | 40        |
| 4.4      | Choosing the Direction of $B_{\text{LSS}}$ . . . . .                                     | 42        |
| 4.5      | Effect of the $\text{RM}_{\text{LSS}}$ on the Structure Function . . . . .               | 47        |
| 4.6      | Adding in Galaxies . . . . .   | 48        |
| 4.7      | Effect of the Strength of $B_{\text{LSS}}$ on $\text{SF}_{\text{Tracing LSS}}$ . . . . . | 50        |

|                   |  |           |
|-------------------|--|-----------|
| 4.8               | Summary of the Structure Function Analysis . . . . . | 52        |
| <b>5</b>          | <b>Detecting a Signal</b>                            | <b>54</b> |
| 5.1               | Random Permutation Test . . . . .                    | 54        |
| 5.2               | Ratio of Signals and Noise . . . . .                 | 55        |
| 5.3               | Effect of Removing High-RM sources . . . . .         | 56        |
| 5.4               | Effect of Improving RM <sub>Error</sub> . . . . .    | 60        |
| 5.5               | Detectability of a stronger field . . . . .          | 62        |
| 5.6               | Error on fitting a line . . . . .                    | 63        |
| <b>6</b>          | <b>Discussion</b>                                    | <b>65</b> |
| 6.1               | Assumptions . . . . .                                | 66        |
| 6.2               | Going Forward . . . . .                              | 67        |
| <b>References</b> |  | <b>68</b> |
| <b>Appendices</b> |  | <b>75</b> |
| <b>A</b>          | <b>Data summary</b>                                  | <b>76</b> |

# List of Figures

|     |  |    |
|-----|--|----|
| 1.1 | Illustration summarising the history of our Universe (ESA & Carreau, 2013)   | 2  |
| 1.2 | Map of the galaxy distribution in the 2dF Survey (Colless et al., 2003) . . . . .  | 3  |
| 1.3 | RM map of the Milky Way (Taylor et al., 2009) . . . . .  | 9  |
| 2.1 | A slice of the Millennium Simulation output at z=0 (Springel, 2005) . . . . .  | 14 |
| 2.2 | Comparison of different methods in modeling the KH instability (Hopkins, 2015) . . . . .   | 16 |
| 2.3 | An illustration depicting the lightcone construction process (Cawood & Roy, 2014) . . . . .  | 17 |
| 2.4 | Illustration of the location of the lightcone in the simulation . . . . .  | 17 |
| 2.5 | Illustration of the process by which we choose the direction of $B_{LSS}$ . . . . .  | 20 |
| 2.6 | Schematic of the project flow . . . . .  | 22 |
| 3.1 | Radio luminosity functions from simulations, Mauch & Sadler (2007) and corrected for use . . . . .   | 27 |
| 3.2 | Fraction of galaxies in each Stellar Mass ( $M_\odot$ ) bin that host an AGN . . . . .   | 28 |
| 3.3 | Scatter plot of the Flux (Jy) vs Mass ( $M_\odot$ ) for SFG and AGNs . . . . .   | 30 |
| 3.4 | Scatter plot showing the angular positions (degrees) of sources where the darkness of the colour indicates the polarised flux density (mJy). . . . .   | 31 |
| 3.5 | Source count plot using final Polarized Flux Densities (mJy). The blue curve shows observational results from Stil et al. (2014) while the green line shows the results of identifying sources in the simulation. . . . .  | 32 |
| 3.6 | Simulation of the effect of noise on a SF (Stil et al., 2010) . . . . .  | 33 |
| 4.1 | The number of gas particles , galaxies and halos that can be found in each section of the lightcone . . . . .  | 35 |
| 4.2 | An illustration of the spatial partitioning that is used to search for particles near to the light ray . . . . .   | 38 |
| 4.3 | Left: A comparison of the time taken (s) to run different ray tracing methods as the size of the search space increases. Right: A comparison of the memory usage (MB) when running different ray tracing methods as the size of the search space increases. . . . .  | 38 |
| 4.4 | The distribution of the the fraction of t=rays intersecting gas, galaxies and halos . . . . .  | 40 |
| 4.5 | Comparison of $SF_{\text{Source Only}}$ and $SF_{S+E}$ . . . . .   | 42 |
| 4.6 | Figure showing the directions of the steps along the light rays in the first section of the simulation for a searching radii of 1 Mpc. The directions fail to identify distinct regions and are mostly symmetrical so the RM signal would be vastly reduced. . . . . | 44 |

|      |   |    |
|------|---|----|
| 4.7  | Figure showing the directions of the steps along the light rays in the first section of the simulation for a searching radii of 5 Mpc. At a larger searching radius, more distinct structure is identified. . . . .   | 45 |
| 4.8  | Figure showing the directions of the steps along the light rays in the first section of the simulation for a searching radii of 10 Mpc. The directions found at this radius are similar to those of the 5 Mpc searching radius. . . . .   | 46 |
| 4.9  | Comparison of the SFs for different directional settings of the magnetic fields   | 47 |
| 4.10 | Comparison of the scaled SFs for different directional settings of the magnetic fields . . . . .  | 48 |
| 4.11 | Comparison of the power law indices of the SFs for different magnetic field directions . . . . .  | 48 |
| 4.12 | RM map that contains the signal from the LSS and sources . . . . .  | 49 |
| 4.13 | Comparison of $SF_{S+E}$ (black) and $SF_{Tracing\ LSS}$ (blue). . . . .  | 49 |
| 4.14 | RM map of $RM_{Total}$ . . . . .  | 50 |
| 4.15 | Figure showing the $SF_{Tracing\ LSS}$ (blue) and $SF_{Total}$ (purple). . . . .  | 51 |
| 4.16 | Figure showing the power law indices of $SF_{Tracing\ Galaxies}$ , $SF_{Tracing\ LSS}$ and $SF_{Total}$ . . . . .   | 51 |
| 4.17 | Comparison of $SF_{Tracing\ LSS}$ for $B_{LSS} = 100\ nG$ (red), $B_{LSS} = 10\ nG$ (blue) and $B_{LSS} = 1\ nG$ (green). . . . .   | 52 |
| 4.18 | Comparison of the scaled SFs for different of $B_{LSS}$ . . . . .   | 52 |
| 4.19 | Comparison of the power law indices of $SF_{Tracing\ LSS}$ for different strengths of $B_{LSS}$ . . . . .   | 53 |
| 5.1  | Distribution of indices and amplitudes of the SF from shuffled values of $RM_{Tracing\ Galaxies}$ (blue), $RM_{Total}$ (green) and the value from our observations (red) at an observational error of $2\ \mu Jy$ . This plot shows the range of amplitudes and power indices that could be produced from a random combination of the RM measurements. We see that $RM_{LSS}$ affects the amplitudes of the possible SFs, but the values that we have measured are not significant within this distribution . . . . . | 55 |
| 5.2  | Histogram of indices of the SF from shuffled values of $RM_{Total}$ and the power index from our observations (red) an observational error of $2\ \mu Jy$ . .   | 55 |
| 5.3  | Histograms of $\delta$ for $SF_{Source\ Only}$ (blue) and $SF_{S+E}$ (green) and a Gaussian distribution with $\sigma = 1$ and $\mu = 0$ and area under the curve equal to the number of bins $\Delta\theta$ in the SFs (red). . . . .  | 56 |
| 5.4  | Distribution of $\sigma$ of $\delta$ for 1000 shuffles of $RM_{S+E}$ . . . . .  | 57 |
| 5.5  | Histogram of $\delta$ for $SF_{Tracing\ Galaxies}$ , $SF_{Total}$ and a Gaussian distribution with $\sigma = 1$ and $\mu = 0$ . . . . .   | 57 |
| 5.6  | Histogram of $RM_{LSS}+RM_{Source}+RM_{Error}$ (blue), $RM_{Galaxies}$ (green) and $RM_{Total}$ (red). . . . .  | 58 |
| 5.7  | Comparison of $SF_{Total}$ (blue) and $SF_{Total}$ after we cut out all galaxy outliers of $ RM_{Total}  > 100$ (green). . . . .  | 58 |
| 5.8  | Comparison of power indices of $SF_{Total}$ and $SF_{Total}$ after we cut out all galaxy outliers of $ RM_{Total}  > 100$ (green). . . . .  | 59 |
| 5.9  | Distribution of indices and amplitudes of the shuffled values and our measured value after we cut out all galaxy outliers of $ RM_{Total}  > 100$ . See Figure 5.1 for details. . . . .   | 59 |

|      |  |    |
|------|--|----|
| 5.10 | Histogram of indices of the shuffled values and our measured value , after we cut out all galaxy outliers of $ RM_{Total}  > 100$ . . . . .  | 60 |
| 5.11 | Comparison of $SF_{Tracing\ Galaxies}$ after we cut out all galaxy outliers of $ RM_{Total}  > 100$ (blue) and $SF_{Total}$ after we cut out all galaxy outliers of $ RM_{Total}  > 100$ (green). . . . .  | 60 |
| 5.12 | Histogram of $\delta$ for $SF_{Total}$ , $\delta$ for $SF_{Total}$ after we cut out all galaxy outliers of $ RM_{Total}  > 100$ and a Gaussian distribution with $\sigma = 1$ and $\mu = 0$ . . . . .  | 61 |
| 5.13 | Histogram of $RM_{Source}$ (black), $RM_{Error}$ (blue) and $RM_{0.1}$ (green). . . . .  | 61 |
| 5.14 | Distribution of indices and amplitudes of the SF from shuffled values of $RM_{Tracing\ Galaxies}$ (blue), $RM_{Total}$ (green) and the value from our observations (red) at an observational error of $0.1 \mu Jy$ . See Figure 5.1 for details. . . . . | 62 |
| 5.15 | Histogram of indices of the SF from shuffled values of $RM_{Total}$ and the power index from our observations (red) an observational error of $0.1 \mu Jy$ . . . . .   | 62 |
| 5.16 | Histogram of $\delta$ for $SF_{Total}$ at an observational error of $2 \mu Jy$ , $\delta$ for $SF_{Total}$ at an observational error of $0.1 \mu Jy$ and a Gaussian distribution with $\sigma = 1$ and $\mu = 0$ . . . . .                               | 63 |
| 5.17 | Distribution of indices and amplitudes of the shuffled values and our measured value, with an observational error of $2 \mu Jy$ and $B_{LSS} = 100 nG$ . See Figure 5.1 for details. . . . .   | 63 |
| 5.18 | Histogram of indices of the shuffled values and our measured value, with an observational error of $2 \mu Jy$ and $B_{LSS} = 100 nG$ . . . . .   | 64 |
| 5.19 | Histogram of $\delta$ for $SF_{Tracing\ Galaxies}$ , $\delta$ for $SF_{Total}$ when $B_{LSS} = 100 nG$ and a Gaussian distribution with $\sigma = 1$ and $\mu = 0$ . . . . .   | 64 |

# List of Tables

|     |   |    |
|-----|---|----|
| 2.1 | Fixed parameters for this simulation . . . . .                                | 21 |
| 2.2 | Magnetic field parameters for this simulation . . . . .                       | 21 |
| 3.1 | Range of galaxy attributes in this simulation . . . . .                       | 26 |
| 3.2 | Number of galaxies and selected AGN in each mass bin . . . . .                | 29 |
| 5.1 | Comparison of the error on the power index for different detectability tests  | 64 |
| 6.1 | Comparison of the p-value of the power-index for different shuffle tests . .  | 65 |
| 6.2 | Comparison the p-value of $\sigma$ for the different $\delta$ tests . . . . . | 66 |
| A.1 | Number of objects in each section of the cone . . . . .                       | 76 |

# Chapter 1

## Introduction

There is much evidence to support the idea that an interconnected web of dark and baryonic matter is present throughout the universe, and that the objects that we observe lie along the components of this web. However, the nature of the cosmic web is such that it has only recently been observed directly through studies of the distribution of galaxies. Observations and theory about magnetic fields lead us to believe that they should be present even at the massive scales of the Large-Scale Structure (LSS) and so future surveys are in the pipeline to search for the effects that our current theories predict. This project explores one of the ways that measurements will be made to investigate the nature of the LSS. We do this to predict the results of these surveys given our current expectations about the magnetic fields. We explore the effect that variations in the magnetic field model will have on our ability to detect the field of the LSS. We aim to constrain the characteristics of the field that the observed results can expect to find.

### 1.1 The Cosmic Web

People have been fascinated by the night sky since the beginnings of civilisation, and one of the earliest topics of wonder was the arrangement of celestial objects in the night sky. This curiosity continued as the field of astronomy began to formalise and, as we have seen to greater distances, the evidence of a sky where objects seemed to be organised in a non-random way continued to drive questions. In 1926, Edwin Hubble performed a survey of extragalactic objects to find out if there was a scale on which objects no longer looked like they contained structure and started to appear homogeneous (Hubble, 1926). In 1934, Hubble used the Shapley-Ames catalogue (Shapley & Ames, 1932) to determine that there are statistical deviations from random distributions in the positioning of the objects and so the universe is clumpy on angular scales of  $10^\circ$  or fewer (Hubble, 1934).

Large-scale filaments were first observed by de Lapparent et al. (1986) by observing many galaxies and analysing their positions in three dimensions. Similar methods led Kirshner et al. (1981) to be the first to observe a possible void when they found a large region with only a few galaxies. The theory to back up the validity of the observed structures soon followed with work from Hoffman & Shaham (1982), Icke (1984) and Bond et al. (1995). The size of surveys has always limited large-scale science, but as the size and depth of surveys has increased, we have been able to see that the universe is structured on every scale (e.g. Peebles & Groth, 1975; Davis et al., 1982; Zehavi et al., 2011; Jarrett et al., 2016).

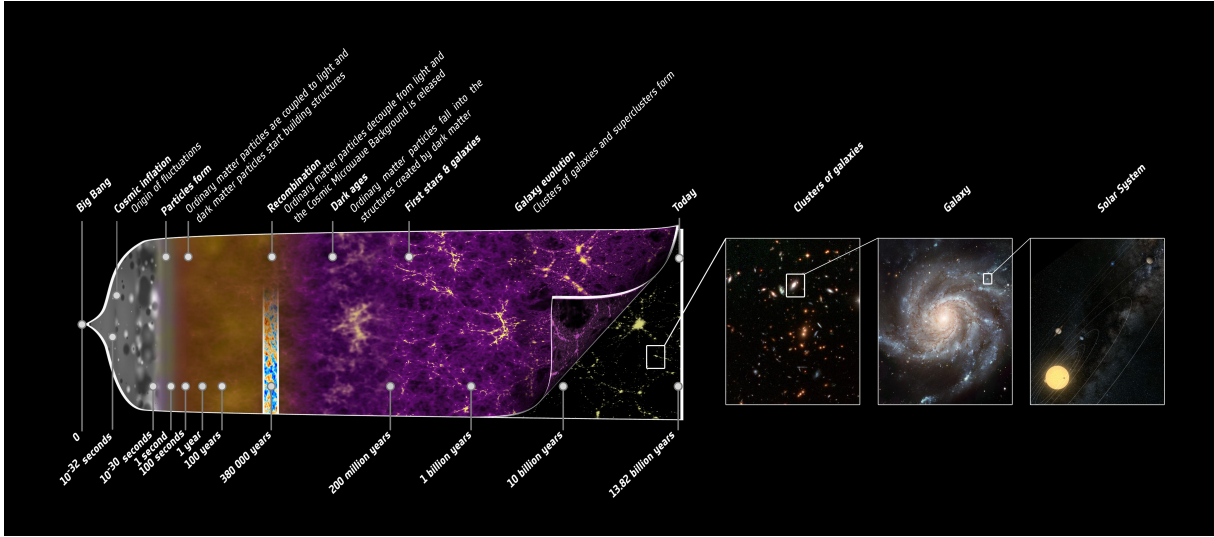


**Figure 1.1:** Illustration of the almost 14-billion-year long history of the universe showing some of the events that occurred between the big bang and what we observe today. The panels on the right side of the illustration reveal close-ups of the cosmic LSS to reveal first a cluster of galaxies, then a spiral galaxy, and finally, the Solar System (ESA & Carreau, 2013).

According to Bond et al. (1995), the observed LSS is a natural result of the expansion of the early universe if there were initial fluctuations and over-densities of matter in the early universe. Springel et al. (2006) goes on to explain how the baryon acoustic oscillations in the matter density in the primordial universe have expanded to become massive structures that form the backbone of the universe that we see today.

The theory supporting our understanding of what we observe is the Lambda Cold Dark Matter ( $\Lambda$ CDM) model (Blumenthal et al., 1984). This model is a parameterisation of the cosmological model that fits best with recent observations since it incorporates both the cosmological constant ( $\Lambda$ ) and cold dark matter.  $\Lambda$ CDM has been extended to predict an early universe which was full of radiation that underwent a period of massive inflation where the universe expanded rapidly. As this radiation cooled, the fundamental particles (such as quarks, leptons and their anti-particles) of matter were formed and combined to form matter. Dark matter is also predicted to have formed but has never been observed even though there is much indirect evidence supporting the existence of such particles (Kolb & Turner, 1994). There are a series of stages from the formation of the fundamental particles until the presence of the elements that we know today that appeared in the epoch of reionisation.

As time went on, and the universe continued to expand the space between particles, gravity acted on both dark and baryonic matter to form clumps and voids out of the initial density fluctuations that were present on every scale in the photon-baryon fluid in the early universe. This prediction of fluctuations on all scales has been confirmed by the Wilkinson Microwave Anisotropy Probe (WMAP, Bennett et al., 2012). The higher density regions led to the formation of stars and quasars, while little formed in the lowest densities. Figure 1.1 (ESA & Carreau, 2013) shows the stages of evolution in the universe from the first moments to the structures we see today. The purple region on the right shows how we expect these structures to have developed and what our current expec-

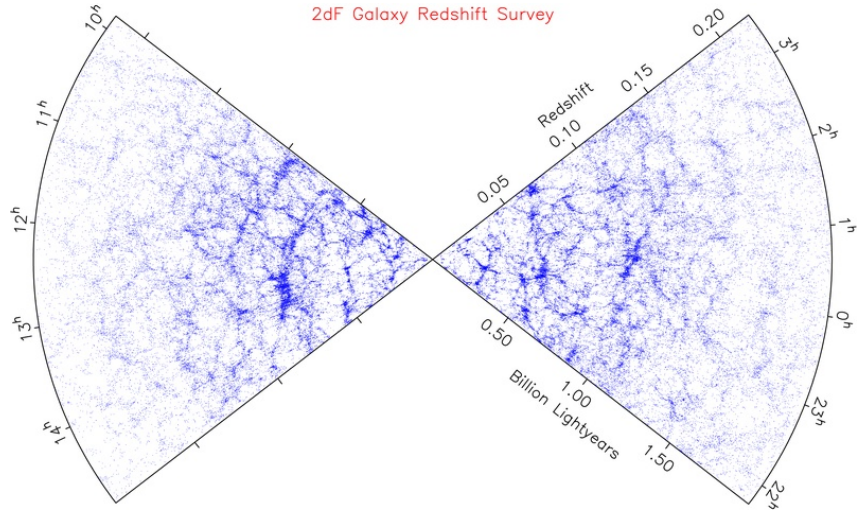


**Figure 1.2:** Figure showing the map of the galaxy distribution produced from the completed 2dF Survey (Colless et al., 2003) which is observational evidence for the existence of the LSS. Each blue dot is an observed galaxy and the structure is seen in the clustering and empty regions in the distribution.

tations are for how matter is organised in the universe. We call the low-density regions voids, and the high-density regions are termed nodes where the nodes are connected to one another through filaments. These structures that we expect to be in existence today are composed mostly of dark matter, but they can be traced by the overlying baryonic matter.

High redshift surveys have allowed studies of the clustering of the LSS (Colless et al., 2001) in detail, and the high-order clustering of filaments and voids have led to the name “cosmic web” being applied to this structure. These voids and filaments are visible when we plot the locations of galaxies in these surveys, such as Figure 1.2 (Colless et al., 2003) showing galaxy distribution produced from the completed 2dF Survey (where 2dF refers to the Two-degree Field (2dF) multi-fibre spectrograph on the Anglo-Australian Telescope). Voids are some of the largest ‘structures’ observed in the universe, and they are thought to contain very low densities due to the relative absence of galaxies in the region.

Filamentary strands of matter connecting the high-density areas where clusters are found to have galaxies located along them, but the exact compositions of the filaments themselves is unknown. Estimates on the nature of the cosmic web predict a hot intra-cluster medium (ICM) with  $T > 10^7 \text{ K}$  and a warm-hot intergalactic medium (WHIM) with  $10^5 < T < 10^7 \text{ K}$  in the filaments that connect these clusters, and both regions contain galaxies. The ICM and WHIM both contain gas that is ionised. The average electron density  $\bar{n}_e$  in the WHIM is  $10^{-5} \text{ cm}^{-3}$  and the sizes of filaments are on the order of 5 Mpc (Ryu et al., 2012). These low densities and temperatures make the filaments hard to detect.

While searching for methods to see this cosmic web, it has been realised that the galaxies are an imperfect probe of the underlying structure of the universe. Kaiser (1984) pointed out that the underlying mass will affect the distribution of objects and where they can appear, such as the fact that clusters will be found at the highest density of matter. This realisation means that galaxies and clusters are biased indicators of the underlying structure, which is composed mostly of dark matter. The large scale filaments

are currently not observable where the baryonic matter is absent.

One of the first observations of a filament that was not inferred from the position of galaxies was made by Cantalupo et al. (2014). Observations of the Lyman- $\alpha$  line for a high redshift quasar using the Low Resolution Imaging Spectrometer (LRIS) on the Keck I telescope revealed emission that went far beyond a reasonable distance for a halo and so Cantalupo et al. (2014) realised that they were seeing intergalactic gas. Caltech has built a spectrograph for the Hale Telescope at the Palomar Observatory called the “Palomar Cosmic Web Imager” which also uses Lyman- $\alpha$  that Martin et al. (2014) have used to observe evidence for filamentary gas inflow onto a quasar.

Non-imaging studies use techniques such as two-point correlations and angular correlations as measures of structure by measuring the degree of clustering that is present. These can help to determine a measure of deviation from pure randomness that the distribution is exhibiting and determining the power at different angular scales (Coil, 2013).

The fact that the LSS of the universe is primarily made up of dark matter provides a serious limitation in our search to understand it. Currently, the most successful methods of observing the LSS are a mix of observations of galaxies and clusters and statistical analysis of the observed distributions. Magnetism and gravitational effects can also be used to infer the presence of this structure.

## 1.2 Cosmic magnetism

Since the cosmic web contains ionised gas, it follows that there will be magnetic fields as the charged particles move around within it. Our aim in this project is to simulate radio polarisation observations and use these to detect the fields that are predicted to exist in the cosmic web to sample the cosmic web itself.

Up until the 1930s, magnetic fields in space were only theorised, but with the development of technologies in World War II and the advent of radio astronomy, the observations of such fields began in earnest. Hey et al. (1946) observed the first discrete radio source Cygnus A and optical methods took off when Hiltner (1949) discovered polarisation in starlight. Observations of other sources followed suit, and the results began to shape our understanding of cosmic magnetism and the idea that magnetic fields are ubiquitous in the universe (Klein & Fletcher, 2015).

Magnetic fields have been seen on almost every observable scale of the universe, but their origin and behaviour remain an area of study where there is still much to learn. There have been many studies done to research primordial fields to determine the properties and behaviour of the earliest magnetic fields. These investigations probe phase transitions (e.g. Caprini et al., 2009), the dynamo mechanism (e.g. Beck et al., 1996), early instabilities in structure (e.g. Lazar et al., 2009), and the first black holes (e.g. Rees, 2006). Understanding the primordial fields is important since voids in the LSS would not have had any other magnetic field contributors and so any field would likely resemble the original seed fields (Durrer & Neronov, 2013).

We observe magnetic fields as both ordered and turbulent on various scales. There

are significant turbulent fields seen in clusters, the nature of the fields is patchy rather than structured on scales larger than 10 kpc (Govoni & Feretti, 2004b). In galaxies, magnetic fields are observable in spiral arms and starburst regions and are present as polarised/ordered fields and non-polarised turbulent fields. Interstellar fields can drive the galaxy dynamics and determine the density and distribution of cosmic rays (Beck, 2011).

An understanding of large-scale magnetic fields is essential for fuller insight into the evolution of the universe. These fields influence the thermal conduction in clusters, confine cosmic rays, and play a part in the evolution of many astrophysical objects. Magnetic fields on a large-scale can be influenced by jets from active galactic nuclei (AGN), galactic winds, and the motion of gases in the intergalactic medium as galaxies and clusters interact. Therefore, we will never fully understand the dynamics of our universe until we understand how these fields formed and how they behave.

### 1.2.1 Magnetism in Galaxies

The nature of magnetic fields in galaxies is highly dependent on the type of galaxy. In spiral galaxies, we can find large and well-ordered fields that seem to follow the spiral arms (Sofue et al., 1986). Magnetic fields in galaxies have been modelled by Chamandy & Taylor (2015) and Pakmor & Springel (2013), while Jansson & Farrar (2012) have studied the magnetic field of the Milky Way. Sa, S0 and elliptical galaxies have less star formation than Sb or Sc galaxies. Elliptical galaxies have a very weak ordered field, as far as we know from observations (Krause et al., 2006a). Both types of galaxies show evidence of turbulent fields on a smaller scale.

Not much is known about magnetic fields in the halos of galaxies, but observations (Dumke et al., 1995; Krause et al., 2006b) reveal an ordered field parallel to the disk when close to the disk and moving to a symmetrical “X-shape” further away when viewed edge-on. This observation suggests a quadrupole field, although the current theories hold that this is an incomplete picture and that dynamo effects also play a part. The low brightness of the radio halo makes it difficult to study these fields in high detail (Beck & Wielebinski, 2013), although Bernet et al. (2008) and Bernet et al. (2013) have discussed the impact of MgII absorption on RM measurements in quasars and suggest that the presence of this process in galaxy halos implies that the halo magnetic fields may be on the order of  $\mu\text{G}$ .

### 1.2.2 Magnetism in Clusters

Clusters are large gravitationally bound objects that contain significant amounts of thermal, non-relativistic gas which, although low in density is still dense in comparison to the wider intergalactic medium. This hot gas is ionised and emits thermal X-ray radiation. Magnetic fields in clusters were first observed by Large et al. (1959) who used radio emission as a probe of the Coma cluster. Kim et al. (1990) went on to study the halo and magnetic field of the Coma Cluster and concluded that particle re-acceleration is part of the formation of the radio halo and that this would point to a strong magnetic field in the cluster medium.

There have since been many studies of clusters, relics and radio halos (as expanded on

by Govoni & Feretti (2004a) and Cassano et al. (2008)). The mostly unpolarised diffuse emission from radio halos is thought to be a result of turbulent magnetic fields in the intracluster medium (ICM), while radio relics produce emission with high polarisation levels that are attributed to shock regions in the ICM (Ryu et al., 2012). The magnetic fields in clusters can be revealed by analysing “polarised emission of radio sources located at different projected distances from the cluster centre” (Bonafede et al., 2010).

### 1.2.3 Magnetism in LSS

The current understanding of the LSS gives us a picture of clumps, voids, sheets, and filaments in the distribution of galaxies, where galaxies are found in the filaments and clusters at the intersections of these filaments (Durrer & Neronov, 2013). The current theory of magnetic fields on a massive scale is that there exist filaments of magnetic fields, similar to those seen in the dark matter simulations that are made to model it. Akahori et al. (2014) suggest that the universe may be suffused with magnetic fields on the order of  $10\text{nG}$  with an upper limit of  $100\text{nG}$  from observations of high redshift quasars (Ryu et al., 1998). These fields would have some effect on the cosmic microwave background, as well as playing a role in deflecting cosmic rays and influencing galaxy clusters (Taylor et al., 2015; Kronberg et al., 2007).

The Intergalactic Magnetic Field (IGMF) has been modelled by Marinacci et al. (2015) who used a randomly seeded magnetic field in the moving-mesh code, **AREPO** (Peebles & Ratra, 2002), to conduct Magnetohydrodynamic (MHD) simulations and trace the resultant magnetic fields. They found that the intensity of magnetic fields traces the underlying structure of the universe.

## 1.3 Methods for Observing Magnetic Fields

Magnetic fields in the universe can be observed through optical polarisation, infrared polarisation, radio polarisation, and the splitting of spectral lines from the Zeeman effect. The optical and far-infrared polarisation arises because of the alignment of dust particles to the magnetic field lines, leading to different extinction levels for different directions of the electric-field vectors of the light. Since the polarisation can be affected by scattering of light, observations have to be done in multiple colours to get accurate measurements (Beck & Wielebinski, 2013).

Radio polarisation is a result of synchrotron radiation which will polarise light linearly while magnetic fields from stars, galaxies, clusters or other structures that lie in the path of the light ray will cause a change in the polarisation angle through the mechanism of Faraday rotation (Fitzpatrick, 2008). The following sections will discuss how we quantify and measure polarisation as well as the methods we use to observe it.

### 1.3.1 Polarisation

Electromagnetic radiation is made up of oscillations in electric and magnetic fields. The orientation of the electric field vector determines its polarisation. Polarisation can be linear or circular, although any linear polarisation can be decomposed into opposite-handed circular components. Since this can change as a function of time, we describe the

polarisation of any monochromatic light wave traveling in the  $\hat{z}$  direction with the ellipse described by

$$\vec{E} = [\hat{x}E_x e^{i\phi_x} + \hat{y}E_y e^{i\phi_y}] [\vec{k} \cdot \hat{z} - \omega t], \quad (1.1)$$

where  $\phi_x, \phi_y$  are the phase angles of the complex amplitudes of the components of the light  $\vec{E}_x, \vec{E}_y$ .  $\vec{k}$  is the wavevector,  $\omega$  is the angular frequency of the light and  $t$  refers to time (s). If there is no difference between  $\phi_x$  and  $\phi_y$ , then the phase angle is steady and the wave is linearly polarised.

When astronomical sources are observed, we measure the time averaged quantity over timescales much greater than the frequency of the wave. We use the Stokes parameters

$$I = \langle E_x^2 \rangle + \langle E_y^2 \rangle \quad (1.2)$$

$$Q = \langle E_x^2 \rangle - \langle E_y^2 \rangle \quad (1.3)$$

$$U = 2\langle E_x^2 E_y^2 \cos \delta \rangle \quad (1.4)$$

$$V = 2\langle E_x^2 E_y^2 \sin \delta \rangle \quad (1.5)$$

to characterise the time-averaged signals where  $\langle \rangle$  indicate a time-averaged value (Stokes, 1852).

The Stokes parameters allow us to define the polarised flux density as

$$I_p = \sqrt{Q^2 + U^2 + V^2} \quad (1.6)$$

and the ratio of the polarised flux density to the total intensity of the flux

$$p \equiv \frac{I_p}{I} \quad (1.7)$$

gives the degree of polarisation. Most astrophysical sources have some degree of polarisation  $0 < p < 1$ .

### 1.3.2 Synchrotron Radiation

When electrons are present in magnetic fields, they experience strong forces and are forced into helical paths along the magnetic field as a result of the Lorenz force. If electrons have relativistic energy, they emit synchrotron radiation which is partly polarised, thus providing a tool to study these environments in various bands, including radio. The type of polarisation(linear/circular) that is observed is a function of the Lorenz factor and the viewing angle (Trippe, 2014). This radiation is bright, and so it affords the opportunity to estimate the strength of the magnetic field perpendicular to the line of sight (Klein & Fletcher, 2015).

### 1.3.3 Faraday Rotation

The first observation of the effect now known as Faraday Rotation came in 1845 when Michael Faraday rotated the polarisation of light in a crystal by exposing it to a magnetic field. He found that the magnetic field affected the velocities of the electric and magnetic field components of the light, hence changing the angle of polarisation that is observed. Alfvén & Herlofson (1950) suggested that cosmic radio waves were generated, in some

part, by synchrotron emission. Later Cooper & Price (1962) found that the polarisation of Centaurus A was wavelength dependent. This observation inspired the work of Gardner & Whiteoak (1966) and Burn (1966a) to study magnetic fields in the universe using Faraday Rotation because it can help us to understand the regular magnetic fields in astrophysical structures.

Faraday rotation is the rotation of the polarisation angle of light rays as they move through magnetic fields. The degree of rotation is proportional to the electron density and strength of the magnetic field component along the line of sight integrated over the distance travelled. There is a strong inverse dependence on frequency so that this effect is small in high-frequency observations, but visible in radio or low-frequency cases. By fitting the equation of Faraday rotation to observations of polarisation measurements at different frequencies, astronomers can determine the degree of rotation as a Rotation Measure (RM) and thereby make inferences about the magnetic fields through which the light ray passed (Fitzpatrick, 2008) (Fitzpatrick, 2008).

This process is complicated by the fact that sources often have more than one component, referred to as a Faraday structure. Two concepts are employed to describe this phenomenon: Faraday Depth over a distance  $r$  is defined as

$$\phi(r) = 811.9 \int \left( \frac{n_e}{\text{cm}^{-3}} \right) \left( \frac{\bar{B}_{||}}{\mu\text{G}} \right) d \left( \frac{l}{\text{kpc}} \right), \quad (1.8)$$

where  $n_e$  refers to the electron density,  $\bar{B}_{||}$  is the magnetic field parallel to the line of sight and  $dl$  is the distance increment along the path. The positivity or negativity of this value gives information about whether the field is pointing toward or away from the observer. RM is derived as

$$\chi(r, \lambda) = \alpha(r) + \phi(r)\lambda^2 \quad (1.9)$$

$$RM = \frac{\Delta\chi}{\Delta\lambda^2} \quad (1.10)$$

where  $\alpha(r)$  is the intrinsic polarisation of the source. This means that the RM describes how the observed polarisation changes over wavelength (Burn, 1966b).

Faraday rotation has been used to search for magnetic fields in clusters, superclusters and the intergalactic medium. In any observation beyond our galaxy, it is necessary to consider all sources of RM. This can be written as

$$RM_{\text{Observed}} = RM_{\text{Milky Way}} + RM_{\text{Source}} + RM_{\text{Extragalactic}} + RM_{\text{Error}} \quad (1.11)$$

where  $RM_{\text{Milky Way}}$  is the Milky Way's RM contribution,  $RM_{\text{Source}}$  is the intrinsic RM of the sources,  $RM_{\text{Extragalactic}}$  is the extragalactic component of the RM and  $RM_{\text{Error}}$  is the observational error on our measurements, as we show in Equation 1.11. We are assuming that any instrumental or atmospheric contributions have been removed, and so by “observed” we are referring to astrophysical measurements.

Extragalactic RM contributions can arise from galaxies, clusters and the intergalactic medium (IGM), disentangling the contributions to identify the source becomes a difficult problem which has been investigated by groups such as Oppermann et al. (2015) who

attempted to disentangle the contributions from extragalactic sources from those of the ISM. The lobes or nucleus of a radio source may produce a polarisation, and so one must be mindful of this fact to ensure that the same source is measured at different frequencies (Beck & Wielebinski, 2013). RM can help us to make observations about the intergalactic magnetic field (IGMF) because we can use different frequencies to determine the total RM due to a source.

On a local scale, there is a magnetic field associated with our galaxy, which means that some of the RMs that we observe come from our galaxy, rather than far into the universe. This field was investigated by Taylor et al. (2009) who produced a map of RM observations of our galaxy, shown in Figure 1.3 where the colours indicate the sign of the RMs and the sizes reflect their magnitudes.

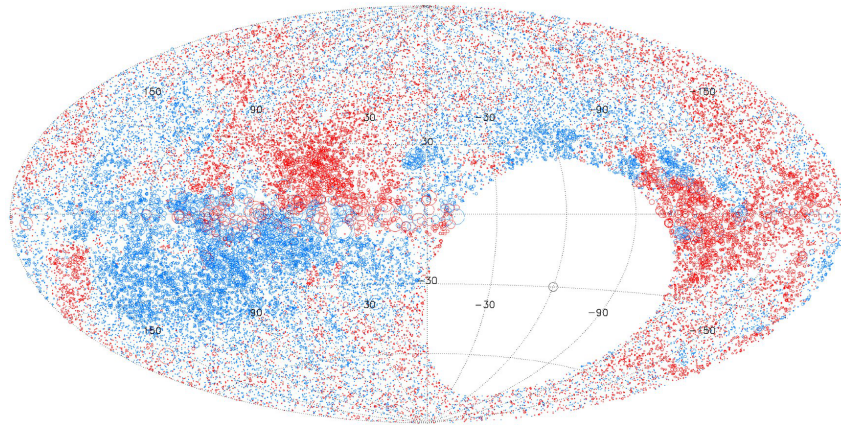


**Figure 1.3:** RM map of the Milky Way where the blue circles indicate positive RM, red circles indicate negative RM and the sizes of the circles reflect their magnitudes (Taylor et al., 2009).

There are many techniques for finding the RM in observations and Sun et al. (2014) compare a few of these in the 1100- 1400 MHz band. They discuss open-ended methods such as Faraday synthesis, wavelets and compressive sampling, as well as model-fitting where they make a comparison of all of the methods and their relative accuracies. The results of their method comparison results provide lower limits for all uncertainties in RM measurements that have been cited in publications to date.

With the advent of new large-scale radio observatories such as the SKA and LOFAR, groups like Bonafede et al. (2015) and Stepanov et al. (2008) are looking at the feasibility of studying magnetic fields in and around galaxy clusters. They create models of galaxy component fields and cluster magnetic fields and produce mock RM observations. These models allow them to derive observation constraints on cluster sizes and templates for future observations.

RM synthesis is the process of recovering the Faraday Depth from multichannel observations of polarised radio data, and is an important tool in observations of RMs. This method makes use of Faraday Dispersion,

$$P(\lambda^2) = \int_{-\infty}^{\infty} F(\phi) e^{2\phi\lambda^2} d\phi \quad (1.12)$$

where  $F(\phi)$  describes the complex polarised surface brightness per unit Faraday depth and  $P(\lambda^2)$  refers to the complex polarised surface brightness (Brentjens & de Bruyn, 2005).

The method of RM synthesis makes use of the fact that this equation transfers easily into Fourier space. Fourier methods are widely used in radio observations to go from the  $uv$  plane (Braun & Walterbos, 1969) to imaging, and so many methods are transferable and allow us to find the physical situation from the observables.

## 1.4 Polarisation Surveys

There have been many surveys that looked at the polarised sky, prioritising either large areas of the sky (wide) or small areas at high sensitivity (deep) observations. Wide area surveys from SKA pathfinders and precursors include the National Radio Astronomical Observatory (NRAO) Very Large Array (VLA) Sky Survey (NVSS, Condon et al., 1998), the Galactic Arecibo L-band Feed Array Continuum Transit Survey (GALFACTS, Taylor & Salter, 2010) and the Polarisation Sky Survey of the Universe's Magnetism (POSSUM, Gaensler et al., 2010) surveys. Deep surveys include the Dominion Radio Astrophysical Observatory Deep Planck Fields (DRAO DPF, Grant et al., 2010), the Australia Telescope Large Area Survey with the Australia Telescope Compact Array (ATCA) (ATLAS, Kolb & Turner, 1994) and Expanded Very Large Array DPF surveys (EVLA DPF, Owen & Morrison, 2008).

The MeerKAT International GigaHertz Tiered Extragalactic Exploration (MIGHTEE) plans to have wide- and deep-field surveys with better sensitivity than preceding surveys. The key goals of these surveys are to use polarisation as a probe of AGN environments, provide insight into weak lensing, investigate LSS, study cluster magnetic fields and understand the evolution of magnetic fields.

NVSS is a wide-field polarisation survey conducted on the VLA which was released in 1998. They observed  $\Omega = 10.3 \text{ sr}$  ( $3.28\pi$ ) of the sky at 1.4 GHz. The lowest sensitivity that was reached was 2.5 mJy, and over 1.8 million sources were detected. GALFACTS is another wide-field polarisation survey that was done using Arecibo. They observed over  $12000 \text{ deg}^2$  of the sky at 1.4 GHz. The RMS noise was on the order of  $100 \mu\text{Jy}$  and over  $10^5$  sources were detected.

The POSSUM polarisation survey will use the Australian Square Kilometre Array Pathfinder (ASKAP), and the early science is currently being carried out. They will observe over  $30 \text{ deg}^2$  of the sky at 1130-1430 MHz. The sensitivity is expected to be  $10 \mu\text{Jy}$  and over 3 million sources are expected to be observed.

The DRAO DPF survey covered  $15.16 \text{ deg}^2$  at 1.4 GHz. They detected 958 sources with a sensitivity of  $55 \mu\text{Jy beam}^{-1}$  in Stokes I and  $45 \mu\text{Jy beam}^{-1}$  in Stokes Q and U. The ATLAS survey performed on ATCA was a deep, wideband, radio continuum survey that covered  $6.3 \text{ deg}^2$  and found 3034 sources down to  $\sim 15 \mu\text{Jy}$  noise levels.

## 1.5 MeerKAT and SKA

The Square Kilometer Array (SKA) is an international project that seeks to construct the world's largest radio telescope with a collecting area of one million square meters (SKA South Africa, 2017). The project has its headquarters at Jodrell Bank Observatory, near Manchester, UK. The telescopes will be based in South Africa and Australia, and the final array is expected to offer us a view into the universe deeper than we have seen before. The SKA phase 1 (SKA1) construction is planned to begin in 2020, with operation commencing a few years later. It is expected that the SKA may be able to answer key questions about the origin, evolution, dynamics and extent of magnetic fields in the universe (Taylor et al., 2015).

The Pathfinder projects in SKA Africa began with the KAT-7 project which is comprised of 7 dishes. This project has been live for some time, observing nearby galaxies, and it has provided much insight into the technologies that need to be developed for the larger project.

The South African precursor to the SKA is the MeerKAT project. It will be an array of 64 receivers, of which the first Array Release of 16 dishes was completed in July 2016. The intention behind this project is to begin to implement and test technologies and systems that will be running on the full array. Eventually, the MeerKAT array will become part of the mid-frequency component of SKA1.

Key science projects on the MeerKAT array comprise projects such as LADUMA which is a deep HI survey, and MHONGOOSE which looks at nearby galactic objects. The project that is pertinent to this work is the MIGHTEE survey, part of which will look at the polarised sky.

MIGHTEE will collect both wide- and deep-field observations (in collaboration with LADUMA). The wide-field will have a sensitivity of  $2 \mu\text{Jy}$  and cover  $20 \deg^2$  and the deep field will have a sensitivity of  $0.1 \mu\text{Jy}$  and cover  $1 \deg^2$ . The resolution of the beam is  $8.5''$  in Tier 1 (Jarvis et al., 2017).

One of the goals of MIGHTEE is to produce a dense RM grid which will reveal many probes that can be used to investigate the properties of the magnetic field in the LSS. The purpose of this project is to develop predictions about what will be observed by MIGHTEE surveys.

## 1.6 Outline of Thesis

The polarisation of radio emission is one of the most powerful probes of magnetic fields in the cosmos, and Faraday Rotation provides a useful method to observe magnetic fields. If magnetic fields are present at the largest scales and associated with the LSS, they will produce Faraday Rotation in the signal of polarised radio sources behind the structure. We can infer the properties of the magnetic fields that the radiation passed through from the extragalactic radio source to the observer by measuring the rotation of the polarisation angle of radiation over broad radio bandwidths.

In this project, we use large-scale n-body universe simulations to investigate the effect of extragalactic magnetic fields on the spatial distribution of RM of radio sources comparable to those that will be detected in deep radio images with MeerKAT. We aim to investigate the feasibility of observing magnetic fields with LSS and whether these are detectable within the sensitivity limitations of the telescope. Through this, we hope to inform MIGHTEE observations to detect magnetic fields associated with LSS (the so-called magnetic cosmic web).

In Chapter 2 we look at the research methods and outline how we went about solving the various sections of the problem. We review the existing simulations and explain why we chose our particular simulation and how we constructed a lightcone to mimic an observed field of view. We also outline why we needed to use information from the simulation to assign radio luminosities to the galaxies and thus choose radio sources. We describe how we went about finding the best method to trace the light from those sources to an observer, as well as the challenges that we encountered in running computations on the large datasets. We discuss the choices we made regarding the strength and direction of magnetic fields in the simulation and explain how we analyse the RM results of tracing through the fields in the simulation. We end with an overview of the parameters of the simulation as well as a schematic of what steps we performed in the execution of this project.

After this, we explain in more detail the process of choosing radio sources in the lightcone in Chapter 3. We go into detail about how we assigned radio emission from the star formation rates and how we used galactic masses to statistically assign AGN properties because information about the galaxy morphology and observational properties was not part of the simulation products.

In Chapter 4, we begin to look at the results of our method. In Section 4.1, we look at the issues faced in this project regarding the large data sets and computational expense, both in computing time and memory, of the project. We look at ray tracing and what these methods are typically used for, and then we compare the different methods that would be useful for this project and explain why we chose the method that we used.

We then show the number of objects that each ray interacted with and consider the effect of different searching radii in choosing the direction of highest density on our predicted observations. We then study the effect of varying the strengths of the field and dependence on electron density. We explore the effect that filamentary fields alone would have on the analysis of the observations investigate the effect on the analysis when galaxy magnetic fields are incorporated.

Chapter 5 explores whether it will be possible to detect these signals using various statistical methods. We also investigate whether there are methods of improving detectability in a given observation.

In Chapter 6, we discuss the future possibilities of this area of study and how the limitations that we experienced in this work can be improved upon in the future.

# Chapter 2

## Tools of the Trade

Telescopes are improving, both in terms of resolution and collecting area as technology improves. Over the past 25 years, we have seen the advent of new domains of astronomy in the infrared and x-ray wavelengths, and major advances in our ability to see deep into the universe in both radio and optical wavelengths. Although there have been previous surveys of cosmic magnetism that go wide and deep (Section 1.4), MIGHTEE will survey more of the polarised sky than ever before with much higher sensitivity than the wide area surveys.

To determine whether the results from MIGHTEE will allow us to detect the presence of magnetic fields in the universe, we develop simulated observations using large-scale simulations of the universe. Making these simulated observations involved the construction of lightcones, tracing of light rays, and the insertion of magnetic fields. Using simulations is an effective way to test methods before the data arrives.

### 2.1 Simulations

The earliest large-scale universe simulations were predominantly gravitational N-body dark matter simulations. More recent simulations have included gas and stars in the models. Many simulations are done with an aim to study how our models of galaxy formation compare to observations as well as the emergence of large scale structure from the primordial universe.

Perhaps the most well-known simulation is the Millennium Simulation (Springel, 2005) which is a “massively parallel TreeSPH code, capable of following a collisionless fluid with the N-body method, and an ideal gas by means of smoothed particle hydrodynamics (SPH)”. The simulation took 28 days to run, using 343000 hours worth of CPU-time on 512 processors. An example of the output is shown in Figure 2.1 which shows a  $15 \text{ Mpc } h^{-1}$  thick slice of the dark matter distribution of the Millennium Simulation output at  $z=0$ , where the strands indicate filaments in the large scale structure, and clusters are shown by the bright nodes.

There are now many large-scale simulations in existence, such as Illustris (Vogelsberger et al., 2014), EAGLE (Schaye et al. (2015), Crain et al. (2015)), MassiveBlack-II (Khandai et al., 2015) and MUFASA (Davé et al., 2016). These are developed as galaxy formation simulation models and use a variety of numerical techniques such as moving-

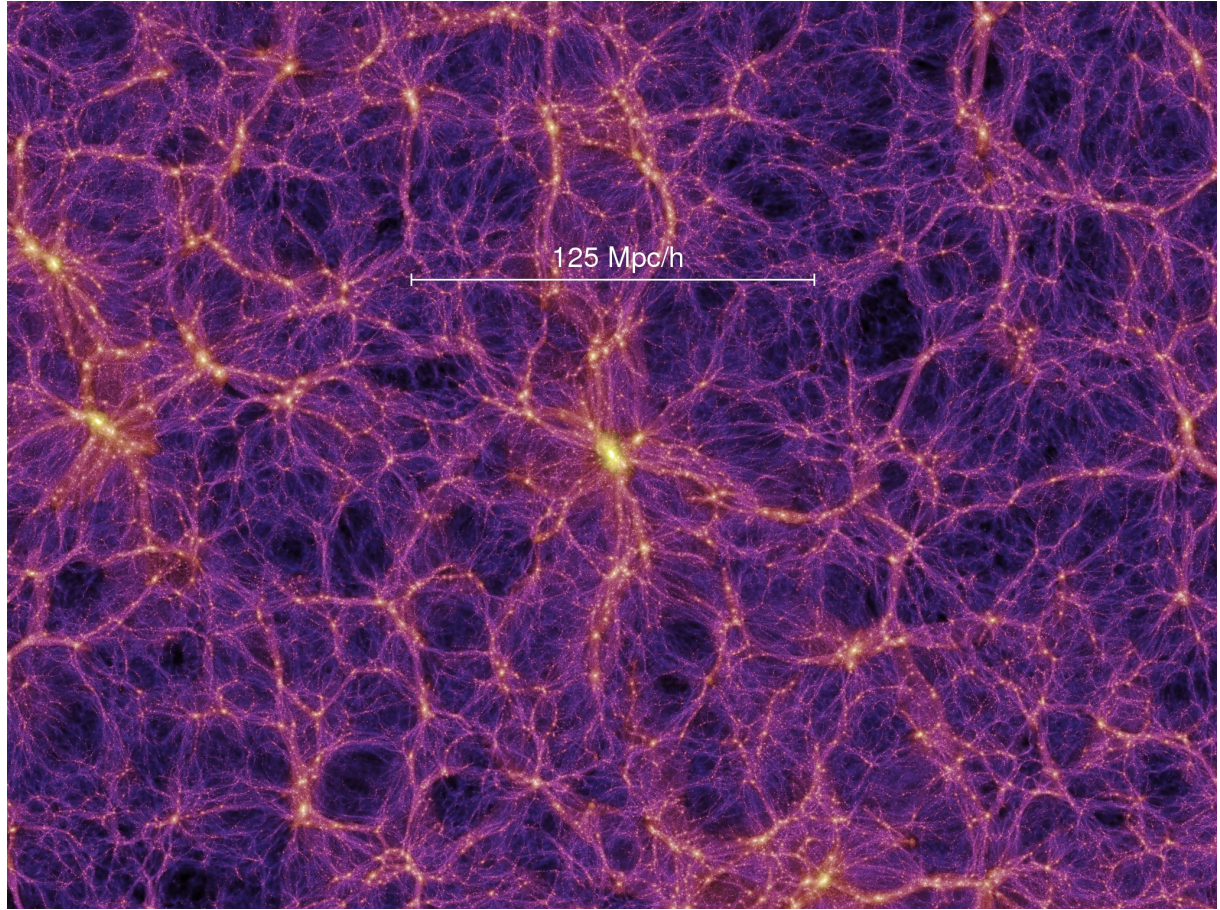


**Figure 2.1:** A  $15 \text{ Mpc} h^{-1}$  thick slice of the dark matter distribution of the Millennium Simulation output at  $z=0$  (Springel, 2005). The brightness of the strands indicates the density of matter, with a galaxy cluster at the center of the slice.

mesh methods, smooth particle hydrodynamics(SPH) and meshes finite-mass methods on large-scale, and sub grid representations to account for star formation and feedback.

Any galaxy formation model needs to fuel star formation, contain stellar feedback and galactic outflows, and feedback from black hole accretion (e.g. Somerville & Davé, 2014; Salmon et al., 2015; Naab & Ostriker, 2016). The Galaxy Stellar Mass Function (GSMF) is hailed as the benchmark for testing this kind of simulations because the observations of this function have been completed up to  $z \sim 3$  by groups such as the Cosmic Assembly Near-IR Deep Extragalactic Legacy Survey (Koekemoer et al., 2011);(Grogin et al., 2011). These observations allow for the testing of the simulations to assert their effectiveness in modelling the true evolution of the universe.

A further adaption to the suite of simulations comes from the use of magnetohydrodynamic (MHD) methods that trace the magnetic field in an electrically conductive fluid. Vazza et al. (2014) produced large MHD simulations with the aim to “study the amplification of cosmic magnetic fields during structure formation, and derive the typical magnetic field strengths in galaxy clusters and filaments [and] investigate the role of other astrophysical sources of magnetisation (galaxies and AGN) towards a self-consistent modeling of cosmic magnetism in large-scale structures”. Although some would claim that the scale of the fields that such a simulation could produce are too large to be realistic, it can help

us to study the behaviour of field strength and direction because divergence of the field is held at 0.

## 2.2 MUFASA and CAESAR

To trace the structure of the large-scale universe, and because we are tracing out to different redshifts, we need to consider the evolution of structure on many scales according to Lambda Cold Dark Matter ( $\Lambda$  CDM) theory. We need a simulation that will reflect an accurate distribution and evolutionary stage of the region of space through which light is being traced.

To achieve our aims, we choose to employ the MUFASA cosmological hydrodynamical simulations (Davé et al., 2016). Their  $50h^{-1}\text{Mpc}^3$  simulation found good agreement with the observed GSMF evolution and can reproduce it as well or better than other existing simulations at any redshift. They also found good agreement to observations for the cosmic star formation rate, density evolution and cosmic stellar mass growth. These simulations can successfully reproduce observed galaxy features over most of cosmic time and provide a good base for the ray tracing that we do in this work. Each snapshot contains roughly  $2.5 \times 10^8$  particles.

The MUFASA simulations make use of a GIZMO meshless-finite-mass (MFM) code (Hopkins, 2015). The strength of this approach is that it takes advantage of the strengths of both SPH and moving-mesh methods. It makes use of a Lagrangian methodology which means that it follows the fluid and has an adaptive resolution. This method allows adaptive time stepping and maintains conservation of momentum. Figure 2.2 illustrates the difference in the new method through the modelling of the Kelvin-Helmholtz instability since it is a good test of fluid-mixing behaviour. The top panel shows how well the MFM model captures the rolls.

Galaxies and halos in the simulations were identified using CAESAR software (Robert Thompson, 2017) in the same process as employed by the team who developed the simulations. CAESAR is a data reduction suite that processes the outputs from GADGET code. It returns the positions and attributes of galaxies and halos from the MUFASA snapshots. From this point on, we use the three categories gas (which traces the LSS), galaxies and halos to describe the components of the simulation and each is distinctly located in space since we exclude any gas within the galaxies or halos from the LSS gas.

The snapshots and CAESAR output are cut into a lightcone out to a redshift of  $z = 1$  using a routine adapted from M. Cawood (Cawood & Roy, 2014). An illustration of the process of cutting a lightcone from stitched snapshots is shown in Figure 2.3.

We do this for two reasons. Firstly, the lightcone mimics the field of view that will be seen in the MIGHTEE observations. Secondly, by identifying which galaxies, halos and gas particles are in the lightcone up front, it is easy to define a line from the radio source to the observer and trace along it. The lightcone cuts through a number of snapshots as the redshift increases, and it traces a vector at an angle to the sides of the cone to avoid repeating the structure in the snapshots along the line of sight (LOS). Figure 2.4

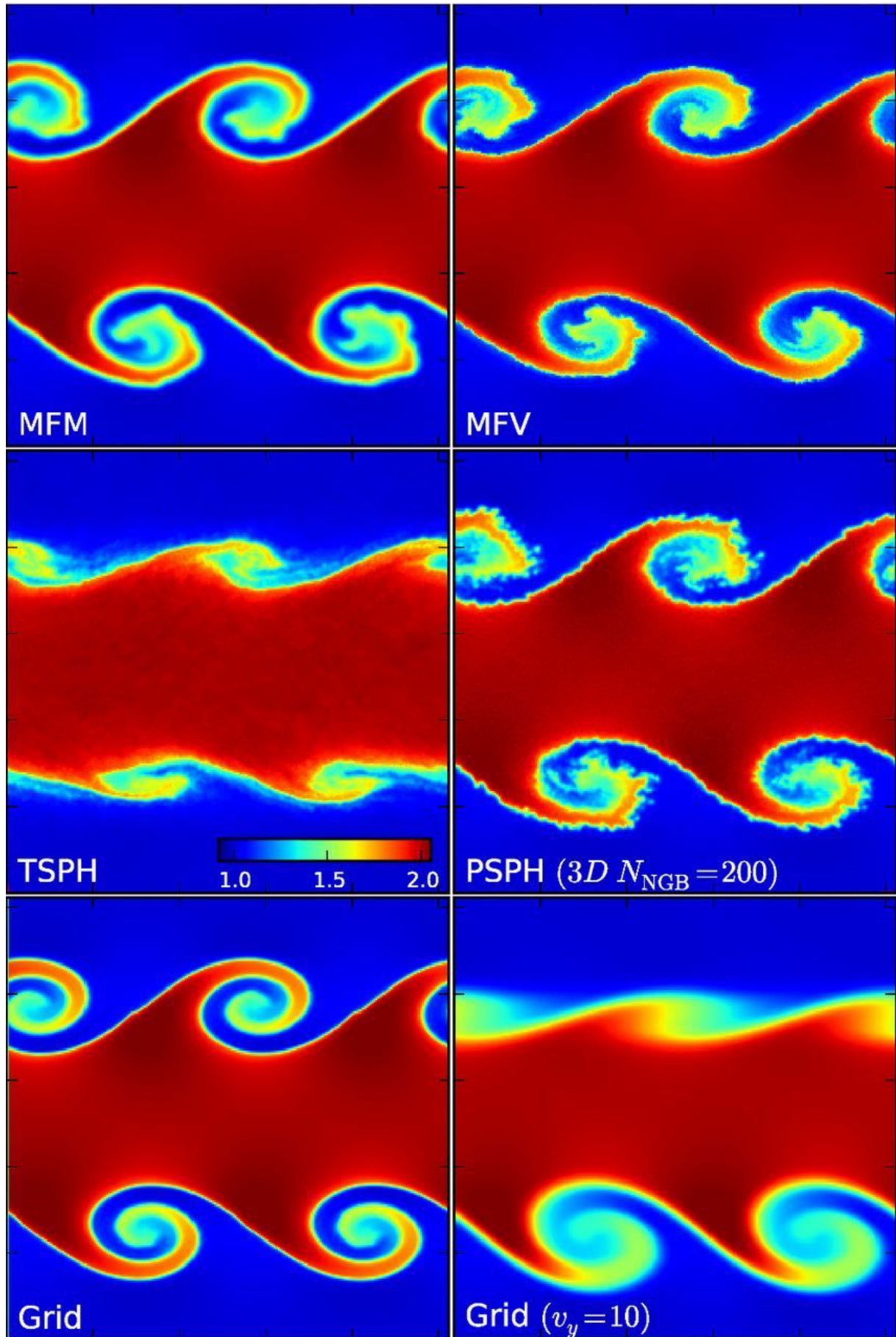


**Figure 2.2:** Tests of various models on the KH instability at  $t = 2.1$ , where the rolls should be going non-linear. The simulations we use employ the MFM method (top left), and the rolls are well captured here (Hopkins, 2015).

shows the gas distribution and location of the first section of the cone in the context of the simulation.

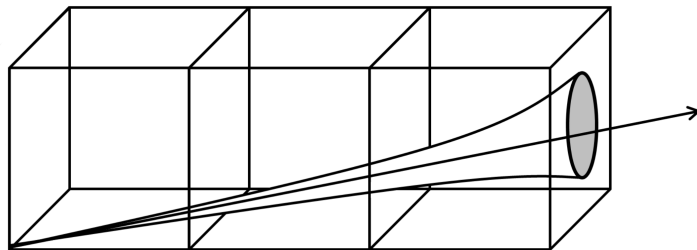


**Figure 2.3:** An illustration depicting the lightcone construction process. The lightcone volume is extracted from a series of stacked simulation cubes, according to a relation between pencil beam-width and frequency (Cawood & Roy, 2014).

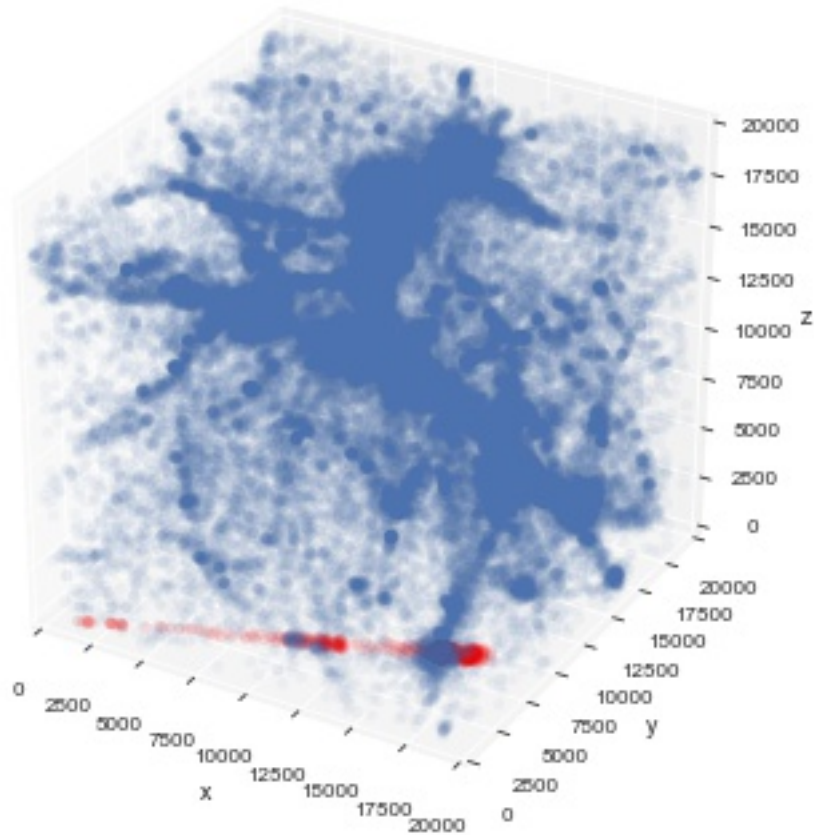


**Figure 2.4:** The red data points represent the gas in the lightcone that we extract from the gas distribution in the larger simulated data cube which is represented by the blue data points.

## 2.3 Radio Sources

When one measures Faraday Rotation, a background radio source is needed so that the effect of the magnetic fields on rotation measure along the path to the observer can be

probed. Our simulation contains galaxies with attributes such as mass, size and star formation rate. The absence of morphological information means that we need to find methods for identifying active galactic nuclei (AGN) and star-forming galaxies and assigning radio luminosities and polarisation. The star-forming galaxies are simpler, with a relation from Bell (2003) giving us a way to derive the radio luminosity directly from the star formation rate. Identifying AGN requires us to separate the galaxies by mass bin and check what fraction of galaxies we can expect to be AGN (Best et al., 2005). After this, we sample a radio luminosity function (Mauch & Sadler, 2007) to assign the luminosities. This process is described in more detail in Section 3.

Once the sources are identified, each source is initialised with an intrinsic RM ( $\text{RM}_{\text{Source}}$ ) sampled from a normal distribution with  $\mu = 0 \text{ rad m}^{-2}$  and  $\sigma = 6 \text{ rad m}^{-2}$  (Schnitzeler, 2010).

## 2.4 Ray Tracing

The term “ray-tracing” most often refers to the graphics problem of rendering a scene under certain light conditions. We are not considering what the viewer would see in optical light, but rather in the resultant polarisation of the light. For our problem, we are using light as a probe of magnetism and ignoring any deflection, refraction or reflection. We assume that light is travelling in a straight line and is non-interacting with the medium in any way except through Faraday Rotation.

We define the light rays by calculating the path that the light would take from each radio source to the observer. The ray is sampled every 10 kpc so that no objects will be missed. The code runs through each segment of the ray and samples the local environment to calculate the RM contribution. We do not have to account for any curvature of the light ray due to expansion since the cone is defined in the comoving units  $\text{Mpc}/h$ . We also do not consider any curvature of the light rays due to gravity.

To calculate an observed RM, we have to know what objects the light passes through along its path. Finding all the intersections can be very computationally intensive, and we find that using kdTrees is an efficient way to search for gas, galaxies and halos that were close enough to affect the polarisation of the light. This is further explained in Section 4.1.2.

## 2.5 Choosing the Magnetic Field Parameters

We previously mentioned that MUFASA is not an MHD simulation and this means that there are no magnetic fields in the simulation. To measure the effect of magnetic fields in the objects that the light rays intersect with, we need to add them to the simulated data. Inserting magnetic fields is not a simple task because real magnetic fields obey divergence laws that limit how the magnetic field can be oriented.

In the LSS we paint our magnetic field ( $B_{\text{LSS}}$ ) such that the average value is on the order of the strength of the magnetic fields predicted by Akahori & Ryu (2010) of

$B \sim 10 \text{ nG}$ , and aligned along the filaments (Ryu et al., 1998). We consider  $B_{\text{LSS}}$  to be locally static and so there is no time dependence in the model. We calculate the Faraday effect of gas, galaxies and halos separately. For the gas particles, we average properties of the nearby particles to calculate the effect on that segment of the light ray. We ensure that we sample only the gas that lies outside of clusters or galaxies and assign a magnetic field

$$|B_{\text{LSS}}| = 1 \times 10^6 (B_0 \times n_e) \quad (2.1)$$

to the gas which is proportional to its density where  $n_e$  ( $\text{cm}^{-3}$ ) is the electron density,  $B_0$  ( $\mu\text{G}$ ) the strength of  $B_{\text{LSS}}$  (a parameter that we will later explore) and the scale factor normalises the electron density so that  $B_{\text{LSS}}$  distribution averages to  $B_0$ . Since we know the electron density of the gas that we pass through, this method provides a way to tie  $B_{\text{LSS}}$  to ionised gas in the simulation. Although there is no physical motivation for this form, it provides a simple way to constrain  $B_{\text{LSS}}$  to the expected magnitudes.

Galaxies have magnetic fields and sometimes the gas from within a galaxy can get ejected by supernovae and galactic winds, pulling the associated magnetic field with it ( $B_{\text{Outflow}}$ ). Donnert et al. (2008) suggests that this can be a significant source of magnetic fields in the IGM. The gas ejected from galaxies is far more metal-rich (elements heavier than helium) than gas that has not been in a galaxy. We account for this ejected material by assigning higher magnetic fields to the LSS gas when metallicity is above 0 according to

$$B = B_{\text{LSS}} \left( \frac{\rho}{\rho_{\text{scale}}} \right)^{\alpha} \quad (2.2)$$

where  $\rho$  is the density,  $\rho_{\text{scale}}$  is a density scaling factor that is set to  $10^4$  times the average gas density in the simulation, and  $\alpha = \frac{2}{3}$  (Stasyszyn et al., 2010).

The direction of  $B_{\text{LSS}}$  in this simulation is a challenge. We test a field fully aligned with the LOS pointing towards the observer ( $B_{\text{Aligned}}$ ), a magnetic field with the direction randomly chosen at every step ( $B_{\text{Random}}$ ), and a more realistic field based on simulations ( $B_{\text{LSS}}$  will refer to this realistic direction).

In order to choose a field direction, we need to know something about the nature of the underlying structure, since we wish to have the case where  $B_{\text{LSS}}$  follows a filament. The simulation does not identify the filaments, so we used the hierarchical structuring of the data that allowed for a search of the nearest neighbour (this is the method used to trace the ray discussed in Section 2.4).

This method allows us to find all of the particles within a chosen radius. From the ray tracing we know the density of each step along the light ray, and so once we find a step with a non-zero density, we locate the direction of the maximum density by finding all nearby gas particles and normalising the direction vectors according to

$$\hat{V} = \frac{\vec{V}}{|\vec{V}|} \quad (2.3)$$

before adding to find the resultant direction. The normalisation ensures that the magnitude of the vectors to distant particles does not skew the direction vector towards some neighbouring filament or dense region. This method allows us to determine the general direction of the filament, and this process is illustrated in Figure 2.5 which shows the LOS

vector and magnetic field direction at one point along the ray.

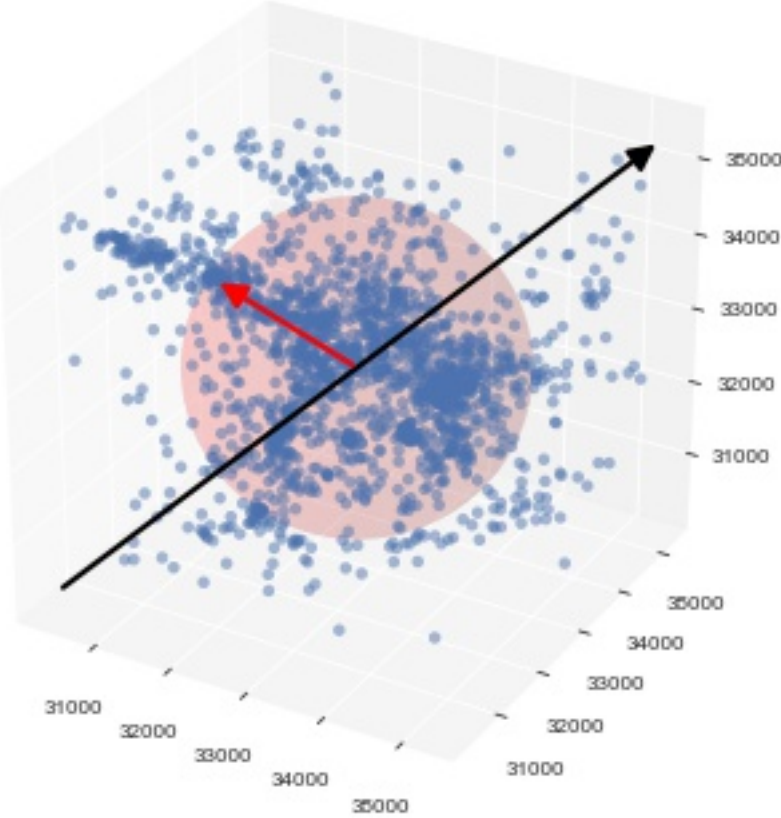


**Figure 2.5:** Illustration of the process by which we choose the direction of  $B_{LSS}$ . The black arrow represents the LOS, and the red arrow is the direction of  $B_{LSS}$  at a certain point along the LOS. This process is repeated every 10kpc along the ray.

The galaxies and halos from the CAESAR output come with some basic attributes, but no observational or morphological information. Therefore we have chosen a few basic characteristics to identify which objects are likely to have magnetic fields that will contribute to the RM signature.

In the simulations, galaxies with  $SFR > 10^{-11}$  are star forming galaxies, and all others are considered passive galaxies. Of course, passive galaxies would have some low level star formation, but since galaxies with low SFR will not be detectable, the cut is reasonable, and results in a list of 210927 passive galaxies and 402641 star forming galaxies. Therefore, we have chosen to consider only galaxies that are central to their halo with positive star formation rates as galaxies which could contribute to the RM that we observe. In order to choose magnetic fields for the galaxies ( $B_{\text{Galaxy}}$ ), we would have liked to use model magnetic fields for galaxies, but we were missing a number of the parameters we would need to do this accurately (e.g. morphology, internal structure and realistic density profiles). We instead used the results from Donnert et al. (2008), Han et al. (1998), Gaensler et al. (2005) and Feain et al. (2009) who probed the magnetic fields of galaxies using background sources. We found the standard deviation of their RM ( $\sigma_{\text{RM}}$ ) measurements and used it to randomly sample a normal distribution with  $\mu = 0$  and  $\sigma = \sigma_{\text{RM}}$  to obtain a

RM measurement for the galaxy ( $RM_{\text{Galaxy}}$ ). We therefore do not obtain values for  $B_{\text{Galaxy}}$ .

For the halos around the galaxies, we refer to observations made by Soida et al. (2011) where they found the halos of star forming galaxies such as NGC 5775 to have some Faraday Rotation, but with an X-shaped magnetic field. Since our concern is the effect of these fields on RM as it passes through, we use the fact that the symmetrical shape of the field will cancel out any net change in RM through the light ray. Therefore we assume a quadrapolar symmetrical field which leads to a net RM contribution of  $0 \text{ rad m}^{-2}$ . We exclude all non-central galaxies and halos that do not contain galaxies from our consideration.

Turbulent fields are present on many scales, but these contribute little to the RMs due to the direction-dependence of the fields in the Faraday Rotation mechanism and the fact that turbulent contributions often sum to 0.

## 2.6 Initial Setup and Project Overview

The fixed parameters for this simulation are summarised in Table 2.1

**Table 2.1:** Fixed parameters for this simulation

| Parameter  | Value    |
|--|----------|
| Maximum redshift   | 1.0      |
| Maximum distance (Mpc/h)   | 1072.73  |
| Number of radio sources (From Section 3.4)                                   | 2675     |
| Line of sight vector through simulation<br>lightcone opening angle (degrees) | [18,2,3] |
| Path length $dl$ (Mpc/h)   | 1.0      |
|  | 0.01     |

The magnetic field parameters begin with the configuration shown in Table 2.2.

**Table 2.2:** Magnetic field parameters for this simulation

| Equation   | Parameter                         | Value                              |
|--|-----------------------------------|------------------------------------|
| $B_{\text{LSS}}$ Strength ( $\mu\text{G}$ ) (Equation 2.1) | $B_0$                             | $1.0 \times 10^{-2}$               |
| $B_{\text{Outflow}}$ parameters (Equation 2.2)             | $\alpha$<br>$\rho_{\text{scale}}$ | $\frac{2}{3}$<br>$1.0 \times 10^4$ |

A flow diagram for the project is shown in Figure 2.6 to summarise the flow of the project since it has many different components.

Using the simulation snapshots from MUFASA, we calculate which particles, galaxies and halos would fall within the boundaries of a pencil beam observation and save the positions and useful attributes of the objects to new files that make up the lightcone.

Next, we look through the galaxies within the lightcone and assign radio luminosities to both star-forming and AGN radio sources and adjust these for the polarised flux and this provides us with a list of source positions and fluxes. Defining the light rays from

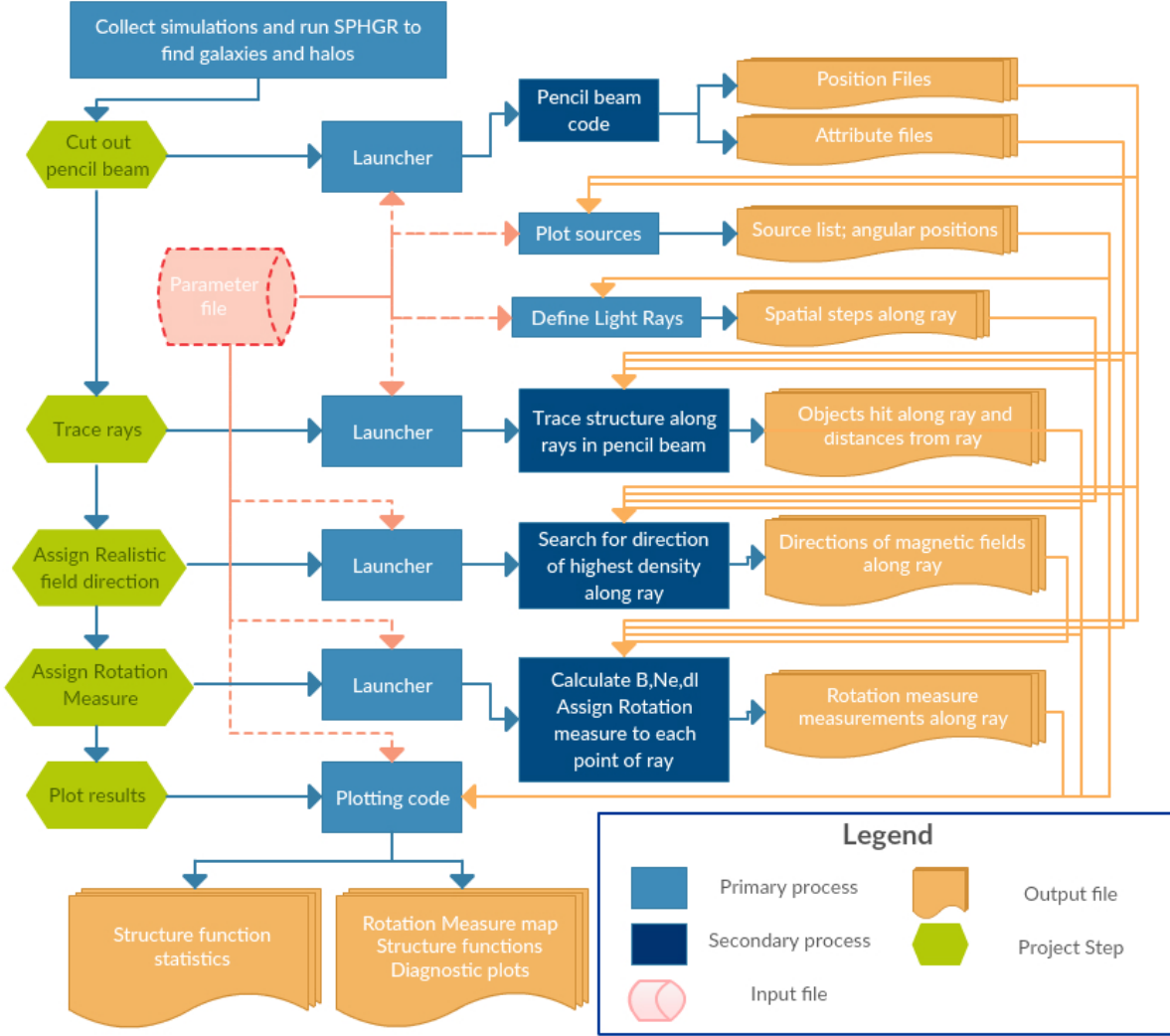


**Figure 2.6:** Schematic of the project flow. Launcher processes spawn parallel instances of the secondary processes. The yellow arrows indicate where the data is pulled into a processing step.

these source positions involves defining a vector from the source to the observer and cutting it into sections of 10 kpc long each to simplify the process of stepping through the rays and finding objects nearby. We save these light rays in sets of 100 and separately for each section because they can become large and memory is a limitation in this project.

We write an algorithm that makes use of the kd-tree method to find objects near to each section of the light ray as well as calculate the distances between the object and location along the ray. We need the distance between object centre and position on the light ray to find the density of a particle where it intersects the ray. We save a list of objects intersecting with each step of the light ray and the distances from the ray.

Next, comes one of the most data intensive challenges of the project where we find the direction of the magnetic field for each step along the light ray. We again use the kd-tree's nearest neighbour features to find all gas particles within a searching radius and then normalise the direction vectors to the nearby particles before calculating the resultant direction of highest density. We save the value of  $\hat{B} \cdot dl$  in these files.

The last step in calculating the RM as per Equation 1.8 is the magnitude of the magnetic field and the electron density. We step again along the ray and find the electron density from the distance from the gas particle and use this to set the strength of the magnetic field as well. Now that we have the magnetic field, electron density and path length, we can calculate a final RM value at each step along the ray which we save to a new file.

The last step in the process is to plot and analyse the results for each set of parameters. We aim to quantitatively compare the results and determine whether the LSS signal is detectable.

# Chapter 3

## Radio Emission from Galaxies

### 3.1 Sources of Radio Emission

The study of radio sources beyond our planet began as an accident when, in 1932, Bell Telephone Laboratories found that they had a problem with radio static on their short-wave transmissions. They asked one of their radio engineers - a physicist named Karl Guthe Jansky - to identify the sources of the interference. Jansky built an antenna and managed to attribute the signal to thunderstorms for the most part, but he was left with a steady signal that rose and fell periodically. In time, he discovered that this period was the same as a sidereal day and that this source must be linked to the rotation of the earth. This observation led to the revelation that the centre of the Galaxy was the source of this radio signal.

At the time, physicists dismissed the result because their theory did not seem to back it up, and it held no application for Bell. Grote Reber, a professional radio engineer, was the only one who showed interest and he took up a project to build a radio telescope in his backyard and confirm Jansky's result. He managed to achieve this and published his results in 1940, but World War II had begun by this time. Astronomy had to take a back foot but the advances in radio technology that marked this period were a springboard for the radio astronomy to come (Condon & Ransom, 2016).

The sources of radio signals are many, and so studying the sky in the radio wavelengths offers insight into a wide variety of astrophysical phenomena. Due to the long wavelengths of radio signals, there is less scattering and interference from dust and our atmosphere. Observing in radio wavelengths can enable us to see deeper into objects than optical light allows. The radio emission that we observe comes from the coherent movement of ionised gas, low energy atomic transitions (e.g. HI), quantized rotation of polar molecules and high-level recombinations. In fact, every object is a thermal radio emitter at some level, which can be a help or hindrance since these objects can show up in observations of background sources (Condon & Ransom, 2016).

The primary “continuum” mechanisms behind celestial radio emission are free-free radiation and synchrotron radiation, which are both results of emission from the acceleration of a charged particle. Free-free radiation is mostly thermal emission, which means that the sources are in local thermodynamic equilibrium. In ionised clouds, the strong electrostatic forces between ions will cause them to rearrange themselves to cause the cloud

to be neutrally charged within the Debye length. As electrons pass by positive ions, they experience an acceleration which causes radiation. The emission is called free-free since the charges are free before and after the interaction. Synchrotron radiation refers to the emission that results from charged particles with relativistic energies that are accelerated by magnetic fields (Ginzburg & Syrovatskii, 1965).

On a Galactic scale, radio emission can be found in the Sun and the continuum emission of other stars and pulsars, in regions of gas ionised by hot stars, and in supernova remnants. The radio sources that we consider in our simulation are found on a much larger scale. We observe extragalactic sources in radio wavelengths either as point or extended sources, depending on the angular resolution of the telescope and distance to the object. In reality, all of these sources are extended, because extragalactic sources are often galaxies, jets or clusters. The source of radio emission from galaxies can arise from either star formation regions or AGNs.

The universe is structured in a web-like structure where galaxies are found along the filaments and in the intersections of the filaments. The presence of the cosmic web means that the distribution and characteristics of the galaxies in the lightcone will be tied into this structure. Many studies have been done to investigate the relation between SFR and radio luminosity. We choose to make use of one of the more recent studies done by Bell (2003) to identify star-forming galaxies (SFGs).

The process is more complicated for the AGNs since no direct AGN-related information is given in the simulations. Without any direct luminosity information or morphology, we have to find less direct ways to determine the distribution of AGNs. Best et al. (2005) investigated the mass distributions of galaxies that have an AGN and developed a relation between the mass of a galaxy and the probability of that galaxy hosting an AGN. This allowed us to determine the fractions of galaxies per mass with AGN, after which it was possible to use the relations described by Mauch & Sadler (2007) to assign luminosities.

Sources in this simulation are found using the galaxies throughout the whole cone. To be identified as a radio source, a galaxy must have a high enough luminosity to generate a flux density above the sensitivity limit of the telescope. The sensitivity limit of MeerKAT is  $2 \mu\text{Jy}$  (Jarvis et al., 2017) for the wide-area radio component of MIGHTEE. For the deep field, a limit of  $0.1 \mu\text{Jy}$  is expected. We consider the wide-field case unless otherwise specified, due to time constraints. We use this flux limit to identify sources.

There were two methods used to assign luminosities to galaxies. First, we looked at the SFR given by the simulation to convert these to radio luminosities. The second source of radio luminosity is AGN sources. The information that is used to perform these calculations is pulled in from the galaxy information produced by the `caesar` routine (see Section 2.2) and the useful attributes that we have from the simulation for each galaxy are given in Table 3.1.

In order to calculate the fluxes of objects, we need their luminosity distances. For this, we use

$$D_L = (1 + z)D_M \quad (3.1)$$

to convert from a comoving distance ( $D_M$ ) to luminosity distance (Hogg, 2000).

**Table 3.1:** Range of galaxy attributes in this simulation

| Attribute   | Minimum value      | Maximum value         |
|---|--------------------|-----------------------|
| Star formation rate [ $M_{\odot} \text{ yr}^{-1}$ ] | 0.0                | 306.83                |
| Stellar mass [ $M_{\odot}$ ]                        | $7.05 \times 10^8$ | $1.43 \times 10^{12}$ |
| Comoving distance [Mpc/h]                           | 43.75              | 2389.95               |
| Redshift [z]  | 0.015              | 1.046                 |

## 3.2 Assigning Radio Flux for Star Forming Galaxies

Condon (1992) and Bell (2003) have defined relations between star formation rates and radio luminosity. We adopt the relation

$$\psi(L) M_{\odot} \text{yr}^{-1} = \begin{cases} 5.52 \times 10^{-22} L_{1.4 \text{ GHz}} & L < L_c \\ \frac{5.52 \times 10^{-22}}{0.1 + 0.9(L/L_c)^{0.3}} L_{1.4 \text{ GHz}} & L \geq L_c \end{cases} \quad (3.2)$$

by Bell (2003) to assign radio luminosities to galaxies. Here  $\psi(L)$  refers to SFR ( $M_{\odot} \text{ yr}^{-1}$ ) and  $L_c = 6.4 \times 10^{21} \text{ W Hz}^{-1}$ . We invert the relation to find  $L$  as a function of  $\psi$ .

The case for  $L < L_c$  is easily inverted, but the relation for  $L \geq L_c$  does not have an inverse function that is easily implemented analytically. We numerically invert the function using an interpolation from the `scipy.interpolate` package. The results from converting our SFR values to luminosities yields a minimum of  $3.79 \times 10^{15} \text{ W Hz}^{-1}$  to  $5.56 \times 10^{23} \text{ W Hz}^{-1}$ . We ignore the 0-value SFR entries which are assumed to be passive galaxies.

We use the radio luminosity function (RLF) from Mauch & Sadler (2007) to compare the theoretical luminosity function to the one that we are obtaining from the simulation. The M&S RLF is locally derived, so we perform this test from the whole  $z=0$  snapshot of the simulation. The  $H_0$  parameters for the simulation and the M&S result differ by  $2 \text{ km s}^{-1} \text{ Mpc}^{-1}$  but, since the relations are derived at  $z=0$ , the effect should be negligible. The results of the shift for the  $z=0$  case is shown in Figure 3.1 where we show our original RLF, the shifted RLF and the theoretical RLF from Mauch & Sadler (2007). It is evident that there is a major vertical shift between these curves, but the turnover point at  $10^{22} \text{ W Hz}^{-1}$  is seen on both curves which rules out an error in the conversion from SFR to luminosity which would have introduced a shift to the left or right.

The SFR values come directly from the simulation where the distribution of SFR matches well with observations. The conversion to radio luminosity is obtained from a relation that is based on observations. We do not understand the cause of this discrepancy, but the turnover values for both relations lie at the same luminosity. However, to standardise our luminosity distribution to observations we calculate the average multiplicative difference ( $\delta\phi$ ) between the models for the luminosities for which the curves should match up. The point on the RLF that we aim to match is chosen to be between the low-luminosity resolution limit of the simulation where the SFR drops sharply ( $10^{20} \text{ W Hz}^{-1}$ ) and the turnover in the luminosity function.

We then choose  $\frac{1}{\delta\phi}$  of the number of sources where the SFR values are kept, and we set the rest to 0 which has the effect of shifting the RLF, as is shown in the Figure. This

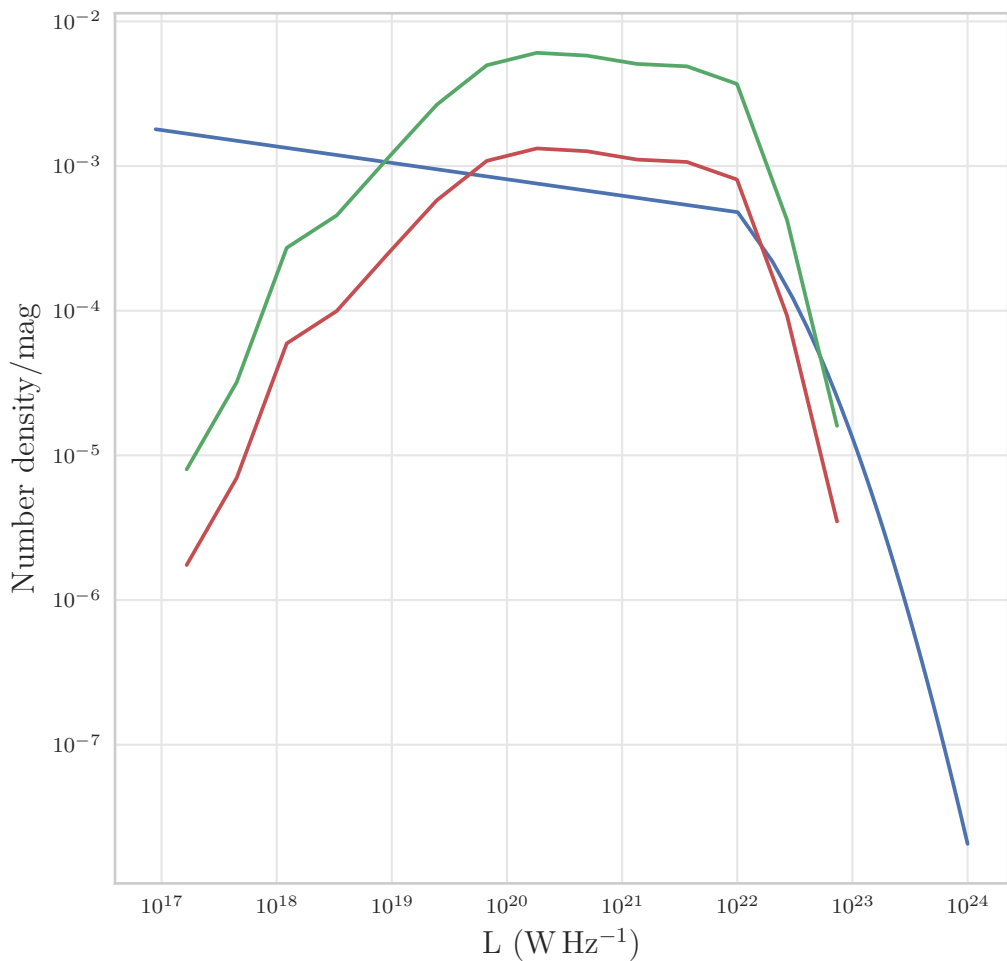


**Figure 3.1:** Radio luminosity functions from Mauch & Sadler (2007) (blue), the SFR- $L$  conversion in the simulation (green), as well as the corrected function that is used for the rest of the project (red) which has been scaled down by a factor of 4.58.

change was seen to have a large difference in correcting the source count plot obtained for the final sources.

Once the luminosities are known, we can use the distance (m) of each object to convert the luminosity to flux using

$$F = \frac{L(1+z)^\alpha}{4\pi D_L^2} \quad (3.3)$$

where the spectral index  $\alpha = 0.7$  which refers to the two-point spectral index between the frequencies at the source frame ( $\nu$ ) and observer's frame ( $\nu_0 = \frac{\nu}{1+z}$ ) (Condon, 1988).

### 3.3 Identifying AGNs and Assigning Flux

These sources are less straightforward to assign since there is no information in the simulation relating to morphology or colour. We use the fraction of galaxies, per stellar mass, that have high enough luminosities to be radio-loud AGN from Best et al. (2005) given

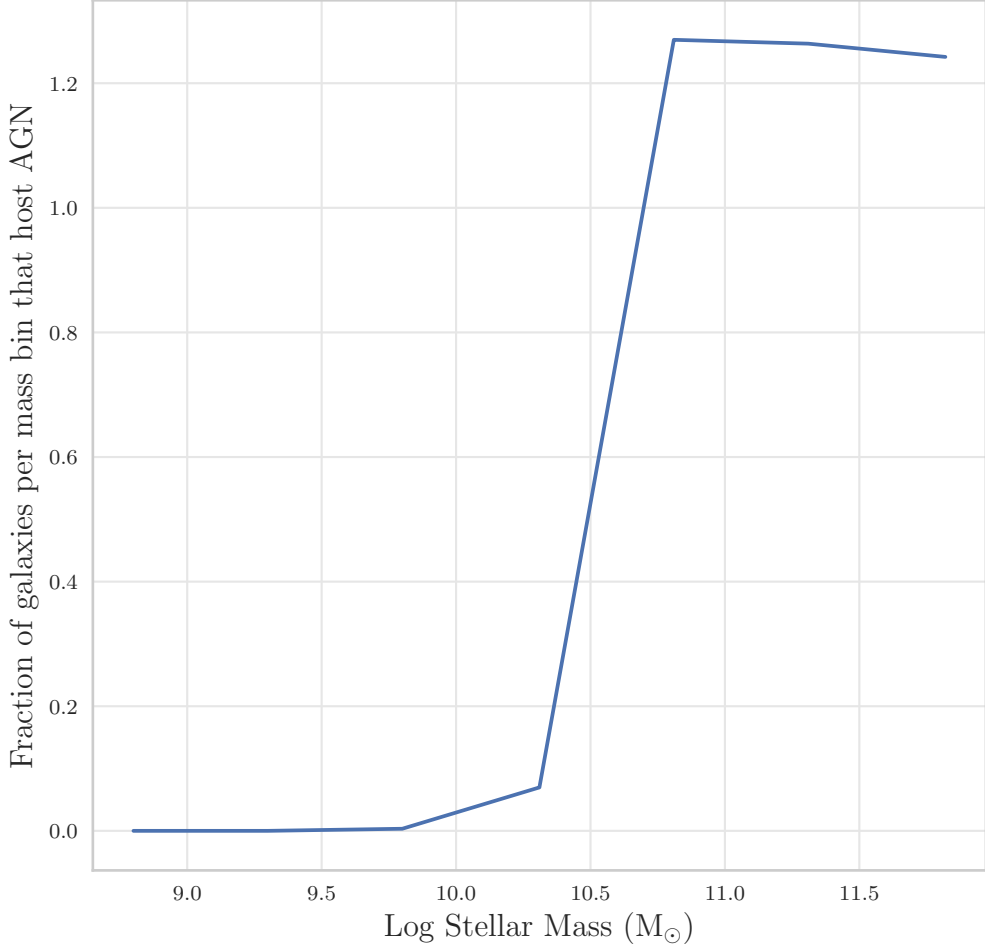


**Figure 3.2:** Fraction of galaxies in each Stellar Mass ( $M_{\odot}$ ) bin that are identified as hosting an AGN determined from the relation described by Best et al. (2005).

by

$$f_{\text{radio-loud}} = f_0 \left( \frac{M_{\odot}}{10^{11} M_{\odot}} \right)^{\eta} \left[ \left( \frac{L}{L_*} \right)^{\beta} + \left( \frac{L}{L_*} \right)^{\gamma} \right]^{-1} \quad (3.4)$$

to select a subset of galaxies in each mass bin to consider as AGN.

We use the best-fit parameters from Best et al. (2005) which are  $f_0 = 0.0055 \pm 0.0004$ ,  $\eta = 2.5 \pm 0.2$ ,  $\beta = 0.35 \pm 0.03$ ,  $\gamma = 1.54 \pm 0.11$  and  $L_* = (2.5 \pm 0.4) \times 10^{24} \text{ W Hz}^{-1}$ . Using this equation gives us a fraction of galaxies per mass bin that host an AGN. There are 2097 AGNs selected in total. The number of AGNs per mass bin are plotted in Figure 3.2. The number of mass bins that we divide our sample into has the effect of influencing the high-luminosity end of the final source count curve and so testing leads us to choose 7 mass bins for the AGN samples and the number of AGN per mass bins is shown in Table 3.2.

We use the RLF from Mauch & Sadler (2007) in order to assign luminosities to the AGN sources. The function is given as

$$\phi(P) = \frac{C}{\left( \frac{P_*}{P} \right)^{\alpha} + \left( \frac{P_*}{P} \right)^{\beta}} \quad (3.5)$$

**Table 3.2:** Number of galaxies and selected AGN in each mass bin

| Mass bin ( $M_{\odot}$ )     | Number chosen | Number in bin | Fraction of bin |
|------------------------------|---------------|---------------|-----------------|
| $8.54 < \log(M) \leq 9.04$   | 0             | 283217        | 0               |
| $9.04 < \log(M) \leq 9.55$   | 0             | 148011        | 0               |
| $9.55 < \log(M) \leq 10.05$  | 3             | 89408         | 0.0034          |
| $10.05 < \log(M) \leq 10.55$ | 44            | 63134         | 0.070           |
| $10.55 < \log(M) \leq 11.06$ | 326           | 25676         | 1.27            |
| $11.06 < \log(M) \leq 11.56$ | 48            | 3799          | 1.26            |
| $11.56 < \log(M) \leq 12.07$ | 4             | 322           | 1.24            |

and the parameters for this relation are  $C = 10^{-5.50 \pm 0.25} \text{ mag}^{-1} \text{Mpc}^{-3}$ ,  $\alpha = 1.27 \pm 0.18$ ,  $\beta = 0.49 \pm 0.04$  and  $P_* = 10^{24.59 \pm 0.30} \text{ WHz}^{-1}$  and we sample a luminosity range from  $10^{22} - 10^{27} \text{ WHz}^{-1}$ .

After we sample the luminosities, we use Equation 3.3 to calculate the fluxes, which result in final fluxes in the range of  $10^{-5} - 10 \text{ Jy}$ , where the exact values are affected by the randomness of sampling.

### 3.4 Combining Flux from SFGs and AGN host galaxies

The fluxes for the two different classes of sources are shown in Figure 3.3. The AGN have much higher fluxes in general and SFGs make up the fainter sources.

We find the fluxes for both types of sources, we add the fluxes per galaxy and identify all of the galaxies which meet the threshold of  $5\sigma$  detection for sensitivity limit for the wide-field survey. This gives us a flux cut of  $10 \mu\text{Jy}$  which leaves us with  $\sim 34000$  radio sources to consider if we were observing the total intensity. At the sensitivity of the deep-field survey there would be  $\sim 69000$  radio sources with a total intensity  $> 0.5 \mu\text{Jy}$  for an observation with the same survey area.

Each of these sources has a fractional polarisation which we obtain from Beck & Gaensler (2004). This relation was derived for AGN and Stil et al. (2008) points out that the degree of polarisation will be less for star forming galaxies. There is currently no relation that we can use to find the polarisation for the star forming galaxies and so we use the results from Beck & Gaensler (2004) across our whole galaxy sample. Once we multiply the flux by the percentage polarisation, only  $\sim 10\%$  of sources have a bright enough polarised flux to be observed, and this leaves us with 2675 sources. The distribution of sources is shown in Figure 3.4 and the source count plot for the polarised flux density is shown in Figure 3.5 with the AGN-only source counts from Stil et al. (2014). Our source counts are in good agreement over  $1 \mu\text{Jy}$ , but our source counts are too high for the lower fluxes and this is a result of the fact that many of our lower flux sources are SFGs which are not present in the source counts from Stil et al. (2014).

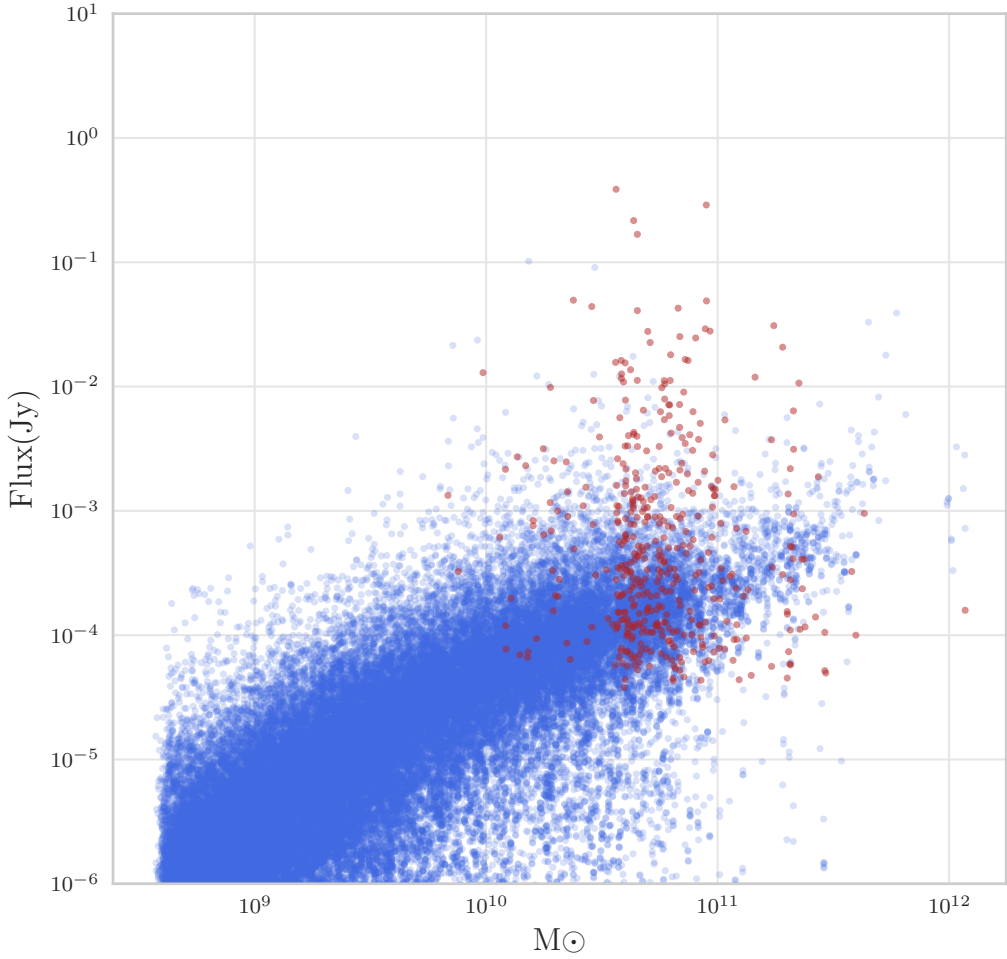


**Figure 3.3:** Scatter plot of the Flux (Jy) vs Mass ( $M_\odot$ ) for SFGs (blue) and AGNs (red).

### 3.5 Observational Error on RM Measurements

Observations of RMs will be subject to measurement errors which are random and show up as a flat structure function, raising the level of the whole structure function. A good example is illustrated in Figure 4.9 by Stil et al. (2010) where the authors demonstrate the effect of noise on a structure function from the Galactic RM. The variance of RM from observational error will be a function of polarised flux density and we must include this effect in our analysis.

The RM can be derived from the slope of the polarization position angle,  $\phi$  as a function of  $\lambda^2$ . If we have  $N$  measurements  $(\phi_i, \lambda_i^2)$  that have been taken over equal bandwidth channels  $\delta\nu$ , the error on RM can be derived from the error on a fit to the slope. The error per channel on the Stokes Q and U flux is  $\sigma = \sigma_n \times \sqrt{N}$  where  $\sigma_n$  is the theoretical noise of an observation using data from the entire bandwidth. The error on the position angle  $\phi$  from Stokes Q and U can be given by

$$\sigma_\phi(\text{rad}) = \frac{\sigma}{2p} = \sqrt{N} \left( \frac{\sigma_n}{2p} \right) \quad (3.6)$$

where  $p$  is the polarised flux density.

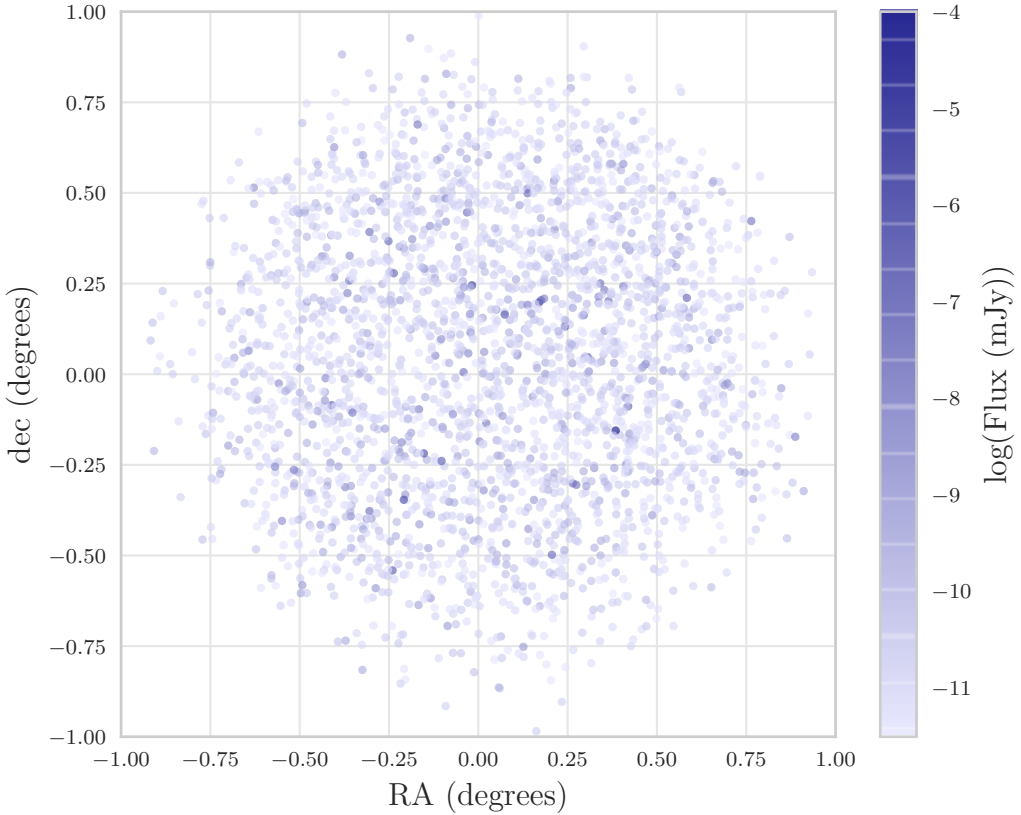


**Figure 3.4:** Scatter plot showing the angular positions (degrees) of sources where the darkness of the colour indicates the polarised flux density (mJy).

The standard error of linear regression slope for the line  $y = mx + c$  is given by

$$\sigma_m (\text{rad m}^{-2}) = \sqrt{\frac{\frac{1}{N-2} \sum_{i=1}^N \epsilon_i^2}{\sum_{i=1}^N (x_i - \bar{x})^2}} \quad (3.7)$$

where  $\epsilon_i$  is the residual between the data and best fit line for point  $i$  (Hinders & Craine, 2014). If the deviations occur due to a normal error distribution of data points, we can manipulate it according to

$$\frac{1}{N-1} \sum_{i=1}^N \epsilon_i^2 = \sigma_\phi^2 = N \sigma_n^2 \quad (3.8)$$

Setting  $x_i = \lambda_i^2$  and  $\bar{x} = \bar{\lambda}^2$ , we can reach the equation for the observational error given by

$$\sigma_m (\text{rad m}^{-2}) = \frac{\sigma_n}{2p} \sqrt{\frac{1}{\frac{1}{N} \sum_{i=1}^N (\lambda_i^2 - \bar{\lambda}^2)^2}} \quad (3.9)$$

Each source will have a flux-dependent error on the measurement. The error on each source is calculated using Equation 3.9 where  $p$  is the polarized flux density of the source and  $\sigma_n = 2 \mu\text{Jy}$  for the MIGHTEE wide-field survey across the expected frequency range (centered at 700MHz). The number of channels  $n = 700$  and the range of wavelengths goes from 18.7 to 33.3 cm. This results in errors with a standard deviation on the order of 1.

If we consider the deep field where  $\sigma_n = 0.1 \mu\text{Jy}$  over the same bandwidth and number of channels, the errors have a standard deviation on the order of  $10^{-1}$ .

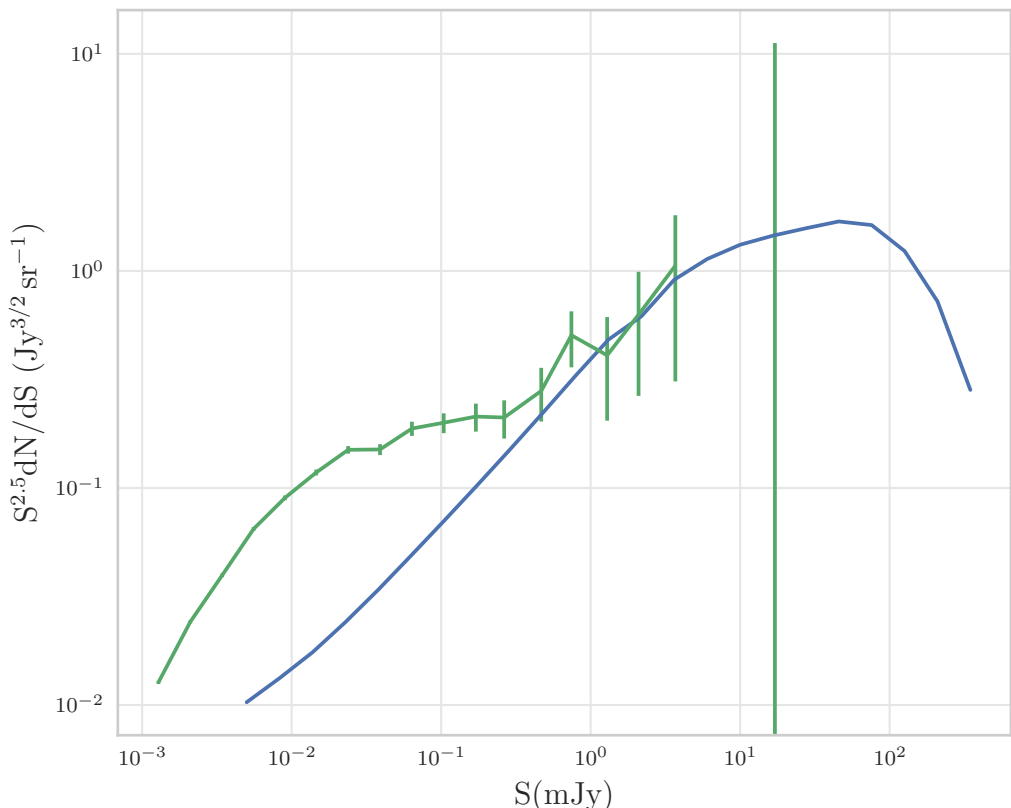


**Figure 3.5:** Source count plot using final Polarized Flux Densities (mJy). The blue curve shows observational results from Stil et al. (2014) while the green line shows the results of identifying sources in the simulation.

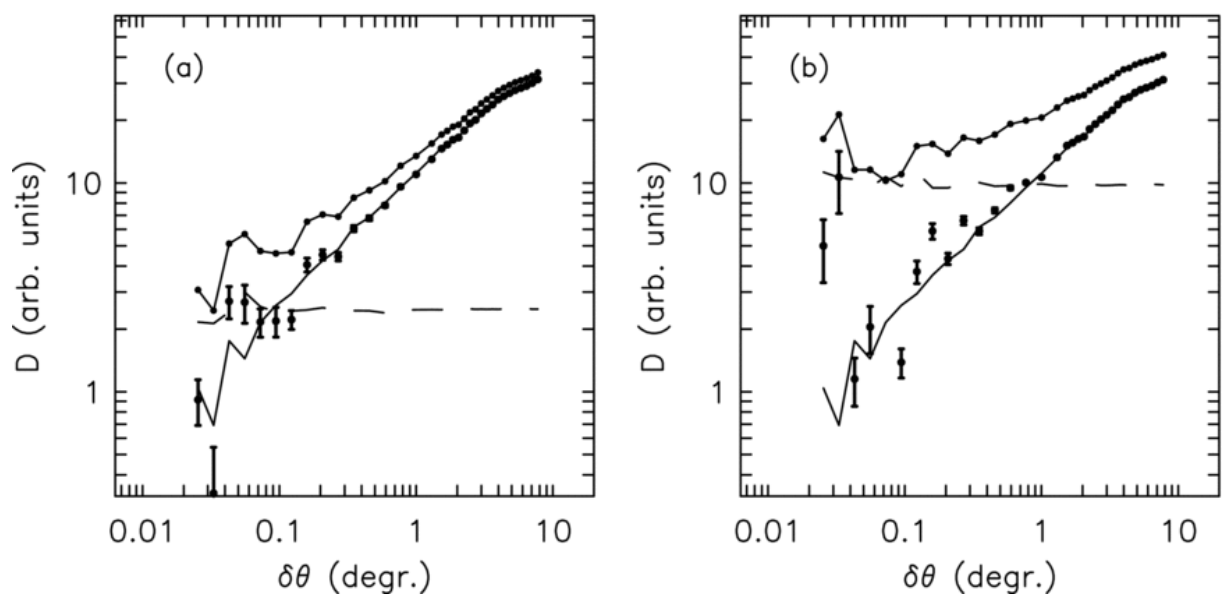


**Figure 3.6:** Simulation of the effect of noise on a SF, assuming two different levels of RM errors. The upper solid curves with dots represent the measured SFs with noise. The dashed curves show the power calculated from the adopted errors. The points with error bars represent the SF after subtracting the noise power. The SF made with the original 1978 noiseless data points is represented by the lower solid curve (Stil et al., 2010).

# Chapter 4

## The Magnetic Field Parameter Space

The MIGHTEE survey will observe the polarisation angles of many objects over different wavelengths and this will allow them to fit a RM value to the results. We are simulating the result that will be observed once the angle has been converted to a rotation measure.

### 4.1 Constructing and Ray Tracing the Pencil Beams

Simulations of the large-scale structure in the universe produce large volumes of data, and managing these large volumes presents challenges. We made use of the resources at the Center for High-Performance Computing (CHPC) to process these large datasets. As we mentioned in Section 2.2, the simulation output is a 24 GB file stored in the Hierarchical Data Format 5 (HDF5) (Folk et al., 2011) format. This file contains information about stars, gas and dark matter in the  $50 \text{ Mpc}^3$  volume cube at different times in the history of the universe. We build a lightcone by calculating the boundaries of the cone using the opening angle which becomes the threshold for choosing whether a particle is kept or discarded. This process requires stitching these cubes together laterally to make a large enough radius to incorporate the opening angle of the cone, as well as sequentially along the line of sight to construct the cone up to a redshift of  $z = 1$ .

Constructing the lightcone is a data-intensive process because each gas particle, galaxy and halo must be checked to see if it falls within the lightcone or not. This process is repeated for subsequent snapshots for increasing redshift. In order to reach a redshift of  $z = 1$ , 46 snapshots are processed along the lightcone, and up to 9 cubes are tiled for the higher redshift sections. For this project, we use only the gas particles. Figure 4.1 shows how many gas particles, galaxies and halos are in each section of the cone (Table A.1 in Appendix A gives specific details).

Due to the data volumes, processing the data is a time-consuming initiative. For this reason, we use only gas particles and discard the dark matter and stars. Cutting out a lightcone reduces the size of the data for the early sections of the cube, but the sections at high redshift saw little to no scale-down in size. Galaxies and halos are post-processed and Figure 4.1 shows how much smaller the quantity of these are in comparison to the number of particles. The files for galaxies and halos are on the order of MBs, and so these are not a large problem from a data perspective.

Even with these data reductions, we have 500 GB worth of data to process along the

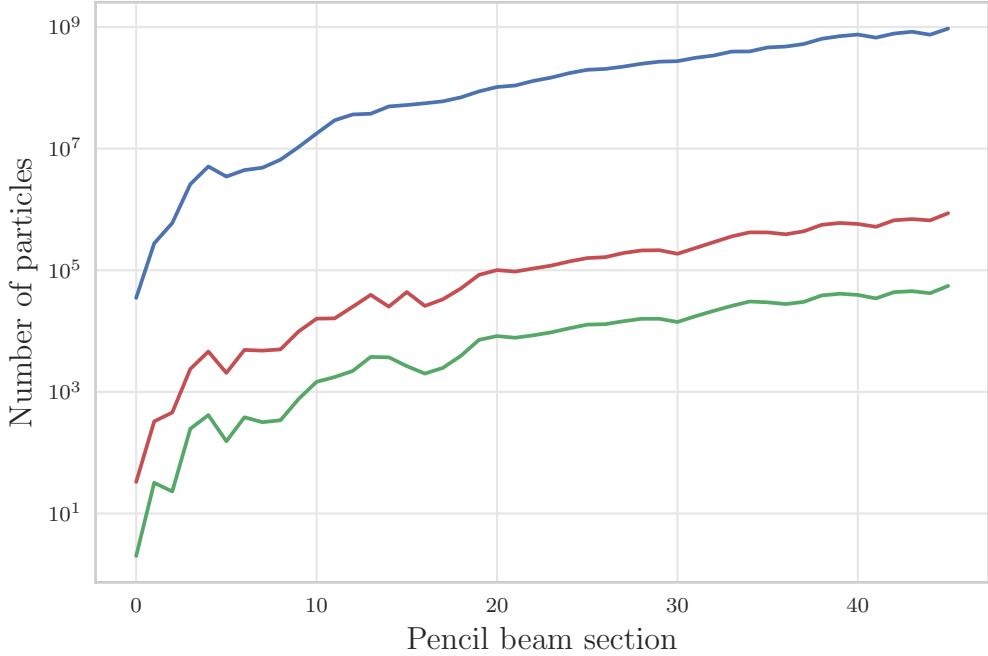


**Figure 4.1:** The number of gas particles (blue), galaxies (green) and halos (red) that can be found in each section of the lightcone

lightcone, and so we organised our pipeline in such a way that each section of the cone is processed separately and the final results are stitched together at the end. This strategy allows us to process the data in such a way that the most data that would have to be dealt with at any one time is 36 GB.

Another challenge of the data sizes is that we have to search finely along a ray within each section for a large number of sources which is a time-consuming process. It is, however, easy to parallelise and so we can run each section for a subset of 100 sources at a time and pull everything back together at the end. The choice of 100 sources per batch is made to balance the computational load. Since each step of the work needs to read in the gas, galaxy and halo information, it is a waste of computing resources to do it for every source, but the files containing the ray information are not small either. Grouping too many sources together could cause the process to quit due to memory overload. There are also specific time limits per job at the CHPC which imposed a limit on the number of sources that could be processed together.

These two divisions of the data resulted in the need to process

$$46 \text{ sections} \times 27 \text{ source subsets} = 1242 \text{ files}$$

per step, and there are multiple steps as shown in Figure 2.6. The code is parallelized by the launcher file in each step and executed using the `mpi4py` package. All of the code is run on the CHPC, and their FAT nodes are used to process the larger or more computationally heavy components of the project.

All of these steps turn a task that is computationally unreasonable into one that can be automated, parallelized and executed within the time frame of this project.

There remains another large challenge which is the tracing of the rays within each section. The intervals along the ray that are computed are 10 kpc apart, and the cubes are 50Mpc long in each dimension. The interval between steps on the light ray results in  $\sim 5000$  computations per section. We explored possible methods to do this effectively before choosing the method that we employed.

### 4.1.1 Ray Tracing Methods

Techniques in ray tracing are used extensively in the field of optics and in computer graphics, where the process of tracing along rays of light was called ray-casting. Ray-casting was developed by Appel (1968) and their intention was to shoot light rays from the eye onto a scene and determine which objects were hit by the light. The first analysis of the technique came from Roth (1982) where he analysed the efficiency of the methods and suggested new ones. Since this is a spatial, not graphics problem, a better term for what this work involves may be “ray shooting”.

Many methods have been developed to approach the problem of searching through space, and the best method is often determined by the specifics of the problem at hand. In the case of a computer game, the objects are moving, and so the algorithm needs to take movement as well as position into account. In physical examples, the objects that the ray hits will have some shape and volume and so it becomes a computational geometry problem. In our case, the objects are modelled as non-moving spheres, and we are given their central position and radii. Therefore, the problem does not require us to consider the relative movements or perform complex analysis of the geometry of the intersection.

There are a number of studies that employ ray tracing in the field of micro-lensing, such as Thompson et al. (2010) who used GPU hardware to create micro-lensing magnification maps and Wambsganss (1999) and Schneider & Weiss (1988) who simulated the lensing due to large objects in a simulation. Often these studies use reverse-sampling, whereby they reverse engineer the light rays so that only those that hit/interact with an object are calculated. This method is not applicable to this project since the light does not terminate upon its interaction with an object and it is expected to intersect with many objects along the path.

I explored a variety of methods to search the lightcone and sample the contribution to the magnetic field. One method is to collapse the space onto a 2-dimensional plane along the axis of searching and then simply sample points on that plane. The difficulty here is to collapse the cone along the axis of the centre of the cone and avoid computational error in calculating the rotated vectors. A second method is to voxellate the lightcone and bin the objects that fall into each voxel so that a column through the cone can simply be added. The loss here is in the resolution of the search. The third method is to compute the distance between the ray and each object in the cone. The last option is to subdivide the space so that the searching area is limited to only those objects that are likely to be hit by the ray.

### 4.1.2 Comparison of Methods to Trace Along the Ray

For this work, we need to trace along a light ray and identify the gas particles, galaxies and halos that it intercepts. This tracing quickly becomes a computationally-intensive problem when we are dealing with a large volume and high-resolution searching.

In the process of deciding which methods to use, we begin with a brute force method approach where every particle in space is tested against each piece of the light ray. Calculating every possible distance is the most basic, but least efficient approach since the search has

$$\mathcal{O}(\text{number of points in ray}) \times \mathcal{O}(\text{number of points in space})$$

time complexity.

The next method makes use of the `cdist` package in the `scipy` suite. This method broadcasts two arrays of spatial points against one another and calculates the distance between them, and so we call it the broadcast method. From the resultant matrix, it is easy to pull out the combinations that are close enough together to fall within their smoothing lengths which is the physical extent of each object. This method is fundamentally the same as the BFM method because there are still the same number of calculations, but it is optimised by `scipy` to be much faster. It uses a large amount of memory in RAM once the number of data points exceeds  $10^6$ , as can be seen by

$$\begin{array}{c} n \text{ points along ray} \\ \left\{ \begin{bmatrix} d_0^1 & \dots & d_0^m \\ \vdots & \ddots & \vdots \\ d_n^1 & \dots & d_n^m \\ d_n^1 & \dots & d_n^m \end{bmatrix} \end{array} \quad (4.1)$$

*m particles in cube*

where the size of the array for  $10^6$  particles would contain  $\sim 10^9$  entries. With the number of data points in this simulation, which can far exceed  $10^6$ , BM arrays quickly became unfeasible to store in RAM and make computations in a reasonable time frame.

The third method that we assess is the `kdTree` package in the `scipy` suite. This method uses spatial partitioning to construct a search tree out of the distribution of particles in space. Once a tree is constructed, it is much faster to find nearby particles because particles in a completely different region of space need not be considered. The time complexity of building the tree is  $\mathcal{O}(n \log n)$  and searching is  $\mathcal{O}(\log n)$  if  $n$  =number of points in space. This method of cutting space into segments and storing the distribution in a tree is illustrated in Figure 4.2.

We test the brute force method (BFM), broadcasting (BM) and tree methods (TM) on a range of sample spaces with randomly generated points ranging from  $10^2$  to  $10^8$  points and a ray with  $10^5$  points. The tests allow us to study how the speed of searching scales with increasing size of the simulation. The results of the time taken per number of particles in space is shown on the left panel of Figure 4.3. The BFM is the slowest, and the trend is showing that this method becomes too slow very quickly. The BM is much faster, but the memory challenges of storing such a large array make it an unfit solution.

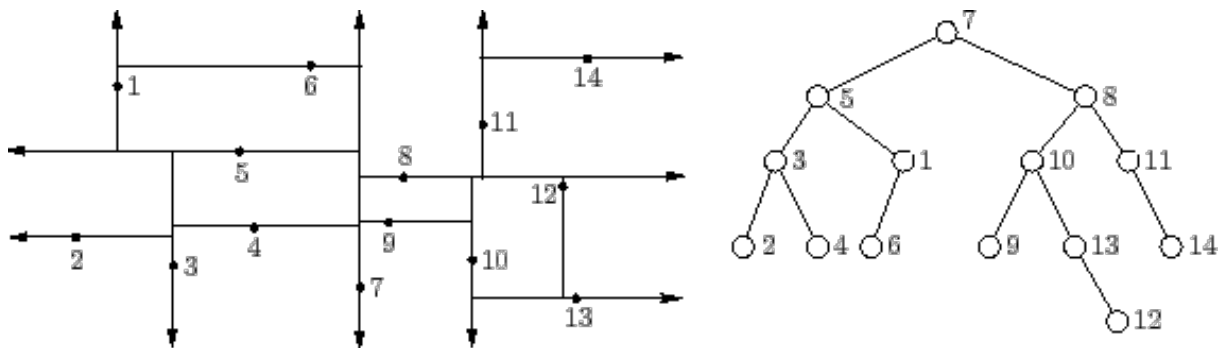


**Figure 4.2:** An illustration of the spatial partitioning that is used to search for particles near to the light ray. The data distribution is split in half at each step (left) and the result is stored in a tree (right). (LaValle, 2006)

The memory usage per number of particles is shown for each method on the right panel of Figure 4.3. The TM is the best since the construction of the tree rises slowly in time, and the time taken is an order of magnitude lower than the BM. The building of the tree begins to take a lot of memory, but the time benefits are significant.

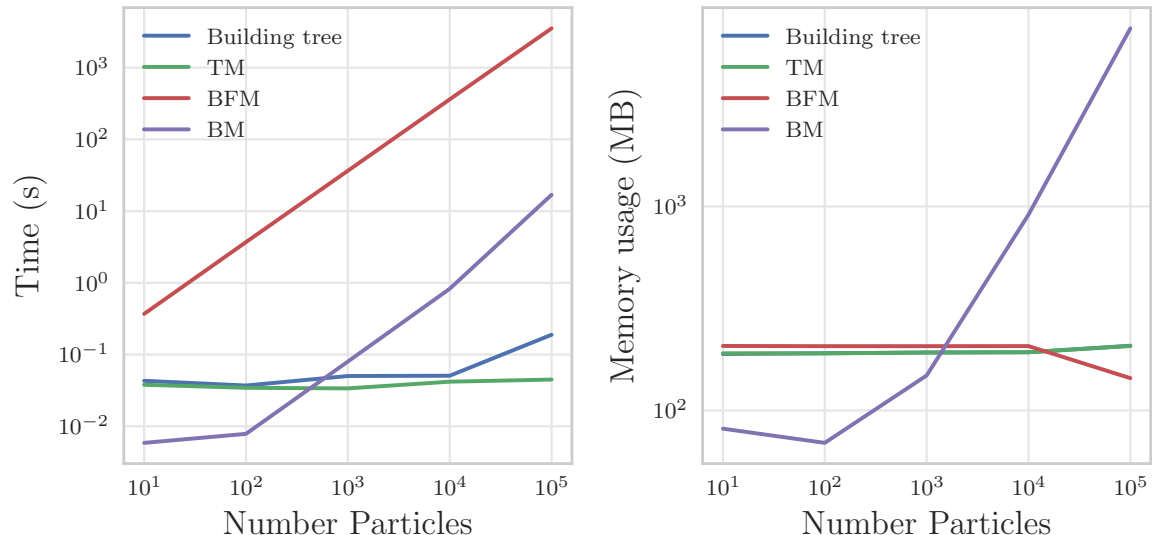


**Figure 4.3:** Left: A comparison of the time taken (s) to run different ray tracing methods as the size of the search space increases. Right: A comparison of the memory usage (MB) when running different ray tracing methods as the size of the search space increases.

Since the size of the data scales up so fast, and the methods of analysis are complex, this project is done using the Lengau Cluster at the CHPC which has nodes of 128 GB RAM each. Some of the largest sections, as well as the code that searches for the direction of highest density, and thus magnetic field direction, are too data-intensive for even these nodes, so they are run on the larger 1TB nodes.

## 4.2 Intersections of the Light Rays in the Simulation

We have discussed our methodology and how we have prepared the simulations, but before we consider the detectability of the magnetic fields in the LSS, we need to determine how to analyse the RMs and how our choice of magnetic field directions and strengths will affect our analysis.

We simulate the sources in the volume of the lightcone as explained in Chapter 3 and trace the rays from these sources to the observer through the cone to give us RM measurements for each source. As mentioned in Equation 1.11, RM measurements are composed of many different contributions. In modeling these, we omit  $\text{RM}_{\text{Milky Way}}$  since we are not choosing a specific line of sight from earth, and we break up  $\text{RM}_{\text{Extragalactic}}$  into  $\text{RM}_{\text{LSS}} + \text{RM}_{\text{Galaxy}}$ .

The contributions to the RM measurement in each light ray come from 4 places. The sources have some intrinsic RM signal ( $\text{RM}_{\text{Source}}$ ) that is expected to be random in its distribution in space. We have modelled this as a random sampling from a normal distribution with  $\mu = 0 \text{ rad m}^{-2}$  and  $\sigma = 6 \text{ rad m}^{-2}$ . There is also a contribution from observational error ( $\text{RM}_{\text{Error}}$ ) associated with each source, as discussed in Section 3.5. The error contribution for a given source is taken as a random sample from a normal inner distribution with  $\mu = 0$  and  $\sigma = \sigma_m$  as given by Equation 3.9.

Galaxies along the light ray contribute to the total RM ( $\text{RM}_{\text{Galaxy}}$ ) because they contain ionised gas and magnetic fields. The method used to assign these magnetic fields was discussed in Section 2.5. The RM signal from the light rays moving through the magnetic field outside of galaxies in the LSS provides the signal that we are searching for ( $\text{RM}_{\text{LSS}}$ ).

In summary, the observed RM in our results is made up of

$$\text{RM}_{\text{Total}} = \text{RM}_{\text{Source}} + \text{RM}_{\text{Error}} + \text{RM}_{\text{LSS}} + \text{RM}_{\text{Galaxies}} \quad (4.2)$$

and we will look at these in various combinations to quantify the effect that they have on whether we can isolate the effect of  $\text{RM}_{\text{LSS}}$  in our analysis. We are simulating the results of the RM that would be measured from the fit of polarisation angle against wavelength in observations and so we did not consider the effect of the change in wavelength over changing redshift. Since the wavelength that is observed has changed by a factor of  $\frac{1}{1+z}$ , the RM results that we obtain are likely to be an upper limit. Hammond et al. (2012) looked at RMs for high redshift sources and determined that there was no strong correlation between redshift and rotation measure and so there is a possibility that the redshift effect is small.

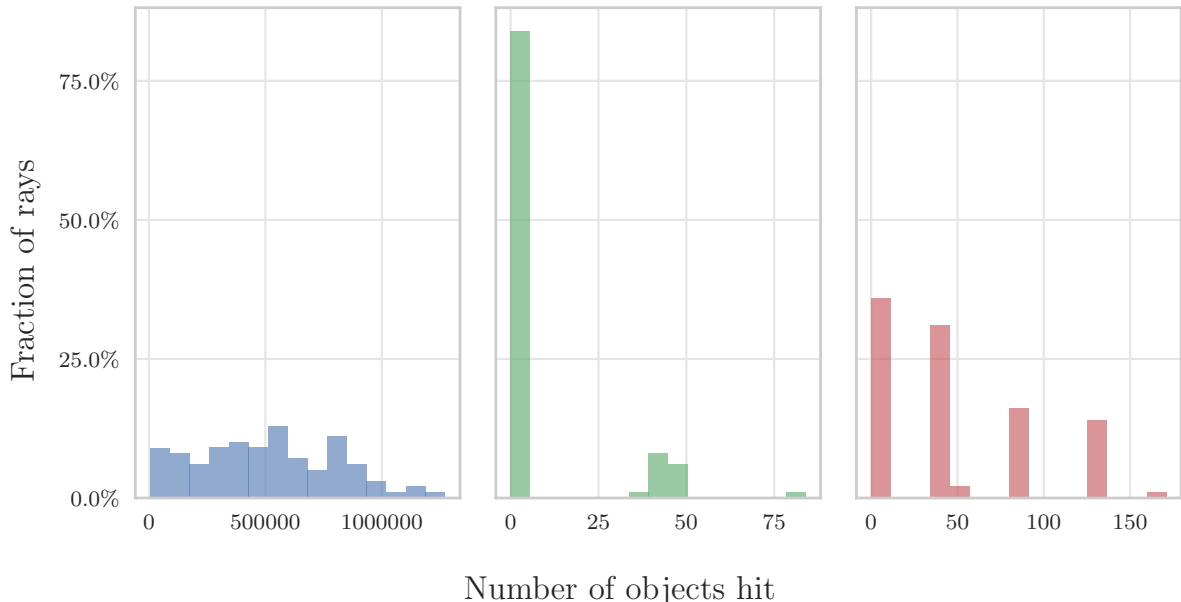
The first consideration is the likelihood of hitting gas, galaxies or halos in the simulation (the distinction between these was described in Section 2.2). We keep track of the number of objects that a light ray passed through along its path and this can help us to understand how much of an influence these different objects will have on the final RM measurements.

Figure 4.4 shows the distribution of the number of objects hit by light rays in the simulation. Most rays hit less than  $5 \times 10^5$  gas particles, most rays hit no galaxies although a

few rays hit tens of galaxies, and around 60% of the rays intersect with tens to hundreds of halos. As we explained in Section 2.5, we do not consider the halo magnetic fields on the assumption that their fields are symmetric and thus the Faraday Rotation will be scattered and have no net contribution along the path.

The gas in the simulation is clumped into masses in units of  $1 \times 10^{10} M_{\odot}/h$  with smoothing lengths of up to  $900 \text{ kpc}/h$ . Outside of the galaxies and halos, the density is low which is why the number of particles that are hit by a light ray can be close to 0 (the distinction between gas and other objects is explained in Section 2.2). If a ray does not come within the smoothing length of a particle, it will not see the particle, and therefore it could be possible to pass near many gas particles and not detect any of them.

Galaxies and halos are also modelled spherically, but this assumption has little impact on the results since so few objects are hit along the path. The galaxy RMs are not dependent on the properties of the galaxy, and we consider the halo magnetic fields to be symmetrical and thus not contribute to the RM as we explained in Section 2.5.



**Figure 4.4:** The distribution of the the fraction of rays intersecting gas (left), galaxies(middle) and halos(right). The first bin in each histogram begins at 0.

### 4.3 Analysing the Rotation Measures

We are searching for an impact of the magnetic field in the LSS on the distribution of RMs on the sky, and so we use statistical techniques to quantify the measure of structure in comparison to a random distribution. A commonly used technique is to use the “two-point correlation function” (Peebles, 1980) which “traces the amplitude of galaxy clustering as a function of scale” (Coil, 2013). Similar methods have been used for RMs to produce “structure functions” since the 1980s (Simonetti et al. (1984); Simonetti & Cordes (1986);

Minter & Spangler (1996)).

The minimum angular scale that can be probed for structure is dependent on the area density of sources, since random errors increase for angular separation bins with fewer object pairs (Stil et al., 2010). We use a Structure Function (SF) defined as

$$S(\Delta\theta) = \langle [\text{RM}(\theta) - \text{RM}(\theta + \Delta\theta)]^2 \rangle \quad (4.3)$$

to probe the structure in our simulation. Here  $\Delta\theta$  is an angular separation on the sky between two sources and  $\langle \rangle$  indicates an average value for all source pairs with a given  $\Delta\theta$ .  $S(\Delta\theta)$  is a measure of the power of the observed structure as a function of angular separation (Simonetti et al., 1985). SFs have been used for analysing rotation measures in the interstellar medium (Han, 2004), extragalactic objects (Feain et al., 2009), the Milky Way (Stil et al., 2010), and turbulence in synchrotron-emitting media (Lazarian & Pogosyan, 2015).

According to Han (2004), two samples drawn from normal distributions with a mean of zero and dispersion of  $\sigma$  should yield a flat structure function with amplitude  $2\sigma^2$ . We call this amplitude the expectation value, and since this represents a probability density function of a Gaussian, less than a third of the points should be more than one standard deviation away from this value. The angular distribution of sources in space is known from the simulation, and  $\text{RM}_{\text{Source}}$  is randomly sampled from normal distributions at each position as described in Section 3.5. We expect  $\text{RM}_{\text{Source}}$  to produce a flat SF since there is no relationship between each  $\text{RM}_{\text{Source}}$  and its angular position.

Figure 4.5 shows the SF for the sources from  $\text{RM}_{\text{Source}}$  ( $\text{SF}_{\text{Source Only}}$ ) and a SF which contains  $\text{RM}_{\text{Source}} + \text{RM}_{\text{Error}}$  ( $\text{SF}_{\text{S+E}}$ ). The error bars in the figure show the error on the mean  $\sigma_\mu$  for each bin  $\Delta\theta$  which are calculated using

$$RMS = \sqrt{\frac{\sum^n (S_i - \mu)^2}{n}} \quad (4.4)$$

$$\sigma_\mu = \frac{RMS}{\sqrt{n-1}} \quad (4.5)$$

The measurements are binned according to their angular separations, and so the errors are a function of the error of the sources in each bin and the number of sources per bin. At the sensitivity of MeerKAT observations,  $2 \times 10^{-6}$  Jy, the observational errors are of the same order as those of the intrinsic RM measurements. The method of assigning these errors is discussed in Section 3.5. Since the resolution of the MIGHTEE beam is  $10''$ , we discard the angular separations below  $20''$  in the construction of our SF.

To quantify differences between these SFs, we fit a slope to the log  $S$ -log  $\Delta\theta$  plots in the form of a power law that is defined as

$$f(\Delta\theta) = a \Delta\theta^k \quad (4.6)$$

where  $a$  is the amplitude,  $\Delta\theta$  is the angular separation bin, and  $k$  is the index (slope) of the fit (Han, 2004). These fits and their associated errors are calculated using the `scipy.optimize.leastsq` package which makes use of a variance-covariance matrix where the diagonal elements can be used to determine the error on the measurement.

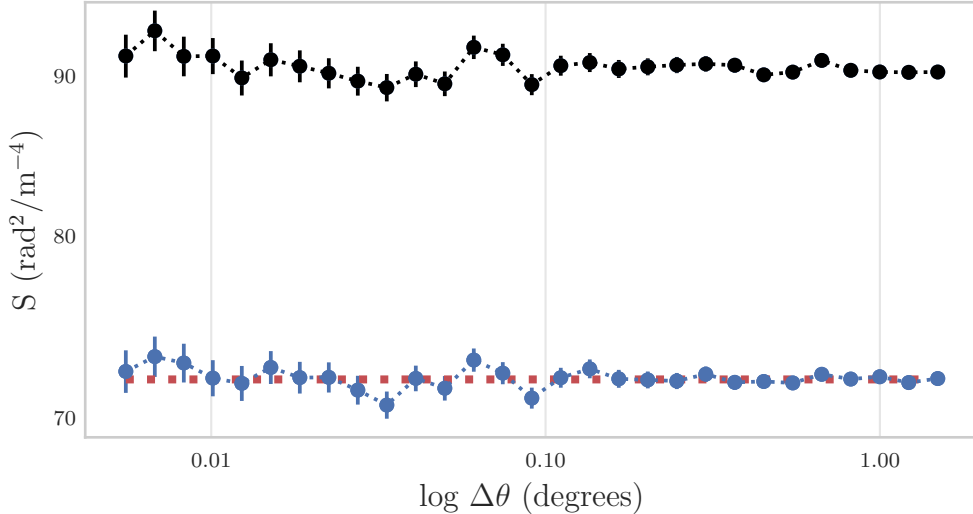


**Figure 4.5:** Comparison of  $SF_{\text{Source Only}}$  (blue) and  $SF_{S+E}$  (black) and the expectation value for  $SF_{\text{Source Only}}$  (red). The error bars show  $\sigma_\mu$  per angular separation bin  $\Delta\theta$ .

The amplitude of an SF is based on the strength of the RM signals, and we can predict the change in amplitude when a randomly sampled signal is added. A flat slope will indicate equal power at all scales, which is what we see in  $SF_{S+E}$  and a non-zero slope will indicate the presence of increasing or decreasing structure as a function of angular separation. The contribution from  $RM_{\text{LSS}}$  will add a signal to the SF that depends on the strength and direction of  $B_{\text{LSS}}$ .

We first explore the parameters used to find the direction of the “realistic  $B_{\text{LSS}}$ ” by varying the radius within which the highest-density direction is calculated. Finding the optimal radius would optimise both the chance of identifying a filament and computational expense since there are  $\sim 5000$  steps along the light ray in each of the ray sections that fall between the source location and observer. At each of these steps, the direction of highest density is computed from the vectors to each particle, and this can lead to many calculations for every step in a high-density region.

Once we identify the direction of highest density, we vary the strength of  $B_{\text{LSS}}$  to see what effect this has on the SF and to provide comparisons and upper or lower limits for the field to be used in comparison with future observations. Based on the research mentioned in Section 2.5, we assume a field strength on the order of 10 nG with a linear dependence on the electron density.

## 4.4 Choosing the Direction of $B_{\text{LSS}}$

The  $RM_{\text{LSS}}$  observed as a result of Faraday Rotation in the LSS is dependent on the angle between the direction vector of the  $B_{\text{LSS}}$  compared to the direction vector along the light ray. Only the component of the magnetic field that is parallel to the ray will affect  $RM_{\text{LSS}}$ , as is shown in Equation 1.8. To investigate the effect of the directionality of the field, we examine the cases of  $B_{\text{Aligned}}$ ,  $B_{\text{Random}}$ , and  $B_{\text{LSS}}$  which takes the large-scale structure into account.

In order to choose  $B_{\text{LSS}}$  with a realistic direction, we use the method discussed in Section 2.5. We identify a radius within which a filament can be recognised, but not so large that it incorporates multiple structures or becomes computationally impossible to calculate. Figures 4.6, 4.7 and 4.8 show the colour-coded directions of the field along the rays for a 1, 5 and 10 Mpc radius in the first section of the lightcone for a subset of the rays.

At a searching radius of 10 Mpc, we approach the limits of what can be computed at any reasonable timescale as there are many particles in that volume for every step along the light ray.

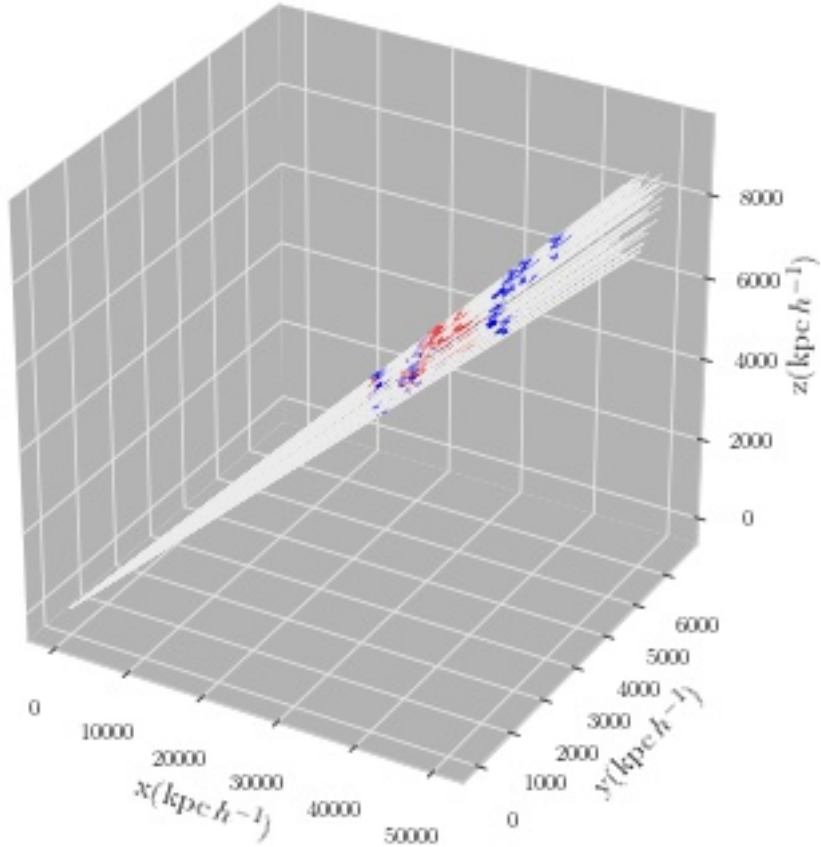
The 3D plots showing the lightcone (lightcone plots) are scatter plots of the steps along a subset of the light rays that show the value of  $\hat{B} \cdot dl$  colour coded to indicate how much of the magnetic field will be seen and whether it will be contributing positively or negatively to the RM. Red indicates  $B_{\text{LSS}}$  in the direction of the observer, blue indicates field in the direction of the source and white indicates  $B_{\text{LSS}}$  perpendicular to the LOS or a region where the magnetic field is 0 due to electron density being 0 at that point. This is obviously not the case for physical systems, but there will be no rotation where the electron density is 0, so the model is sound. In each plot, three distinct regions can be seen, with two of the regions possibly being composed of two structures and the initial assumption is that these distinct regions are separate structures in the LSS that the light rays are moving through.

The lightcone plots for a 1 Mpc search radius indicate that the field directions are not completely uniform in the four distinct regions. The histogram for the 1 Mpc searching radius shows only two distinct directions strongly present in these light rays. Most directions are present in the field, but only strongly positive and negative directions are abundant. It is possible that there are two very large filaments and some smaller ones in this volume and that the light rays that are not shown in the lightcone plot would show this.

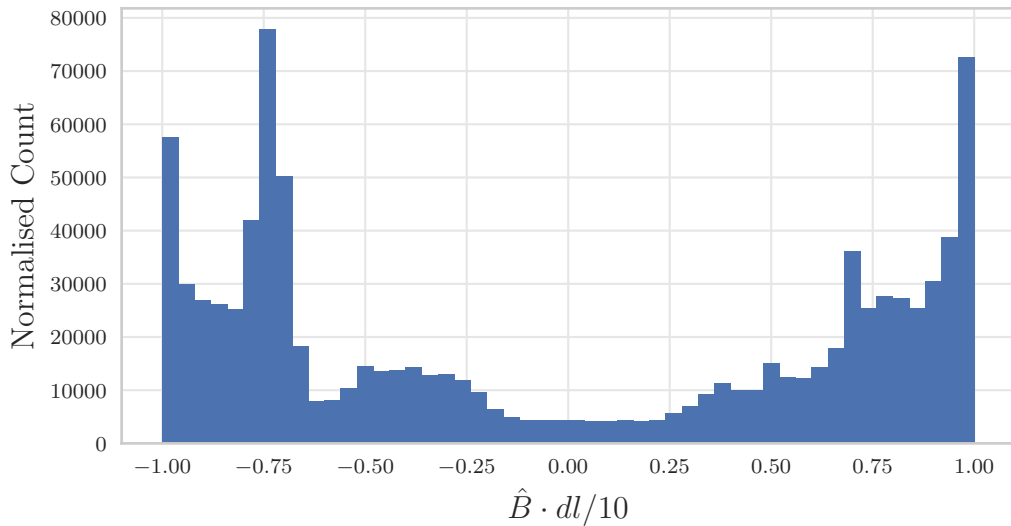
At 5 Mpc, we see two distinct regions of similar colours which imply coherent directions in the two regions and the histogram confirms that there are distinct directional structures that are detected along the light rays. This is shown by the four peaks in the histogram. A similar lightcone plot and four-peak histogram are seen at 10 Mpc, where the structures are only slightly more distinct. This shows that the directions from a 1 Mpc searching radius reflect sub-structures rather than the filaments.

Using a search radius of 10 Mpc turns the denser regions of the lightcone into a computationally-intensive problem. The distributions of 5 Mpc and 10 Mpc look similar and show no significant change in moving to the larger searching radius. Therefore we use a searching radius of 5 Mpc.

Figure 4.9 shows how the SF differs for various field directions. The method used to produce these plots is explained in Section 2.5. As expected, the  $B_{\text{Aligned}}$  has a much higher amplitude SF than that of the other figures. The SF for  $B_{\text{Aligned}}$  puts the full magnetic field strength along the path length, and so this provides an upper limit on the SF that we could observe.  $B_{\text{Random}}$  has equal possibility of showing us the positive signal

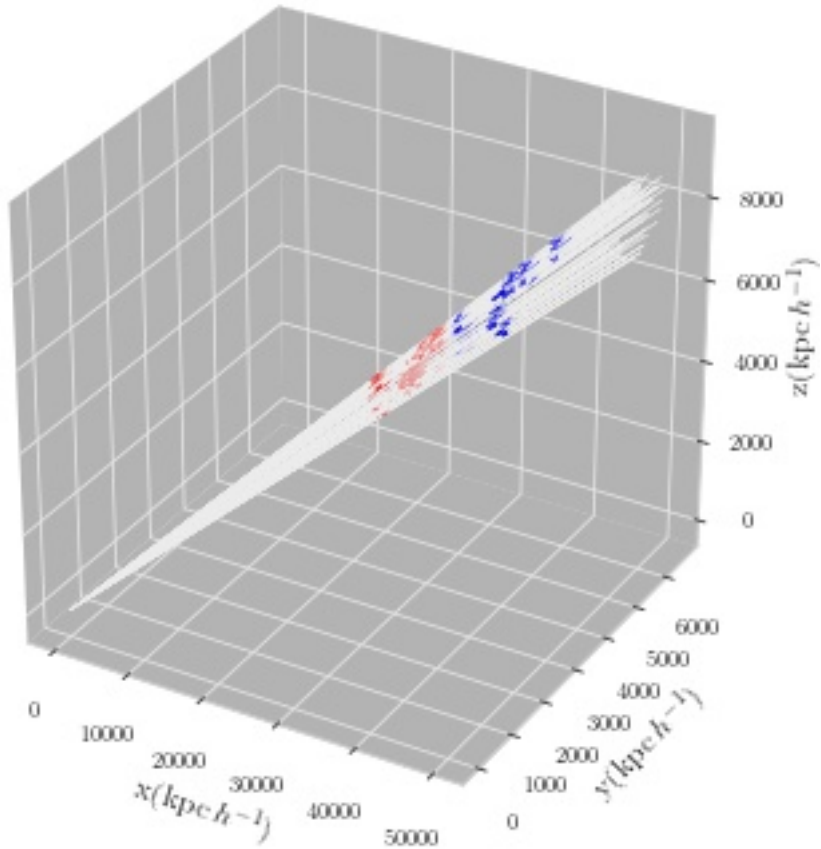


(a) Figure showing the light rays coloured by the direction of highest density when searching with a radius of 1 Mpc. Red indicates  $B_{LSS}$  in the direction of the observer; blue indicates field in the direction of the source and white indicates  $B_{LSS}$  perpendicular to the LOS.

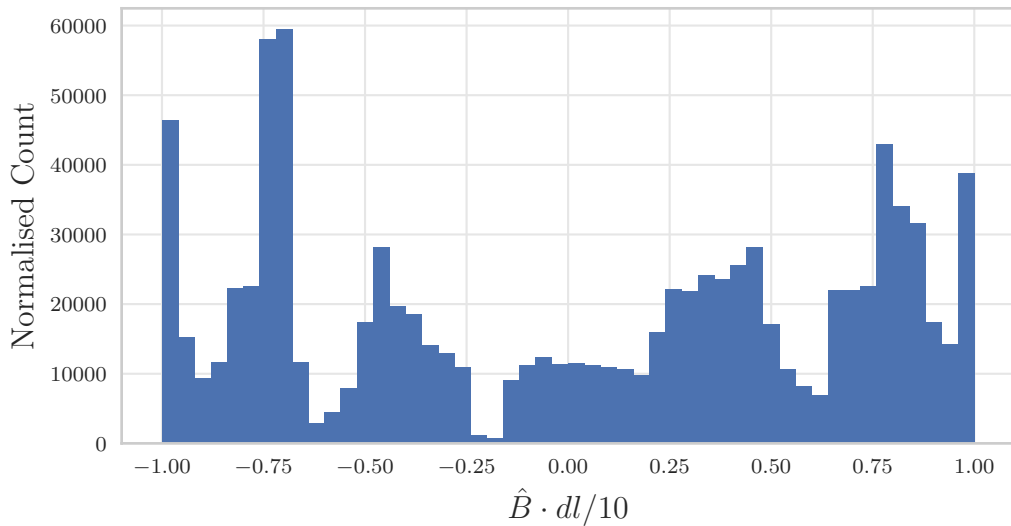


(b) Histogram showing the range of directions found in the cone when the searching radius is 1 Mpc. On the x-axis, 1 indicates  $B_{LSS}$  in the direction of the observer and -1 indicates field in the direction of the source.

**Figure 4.6:** Figure showing the directions of the steps along the light rays in the first section of the simulation for a searching radii of 1 Mpc. The directions fail to identify distinct regions and are mostly symmetrical so the RM signal would be vastly reduced.

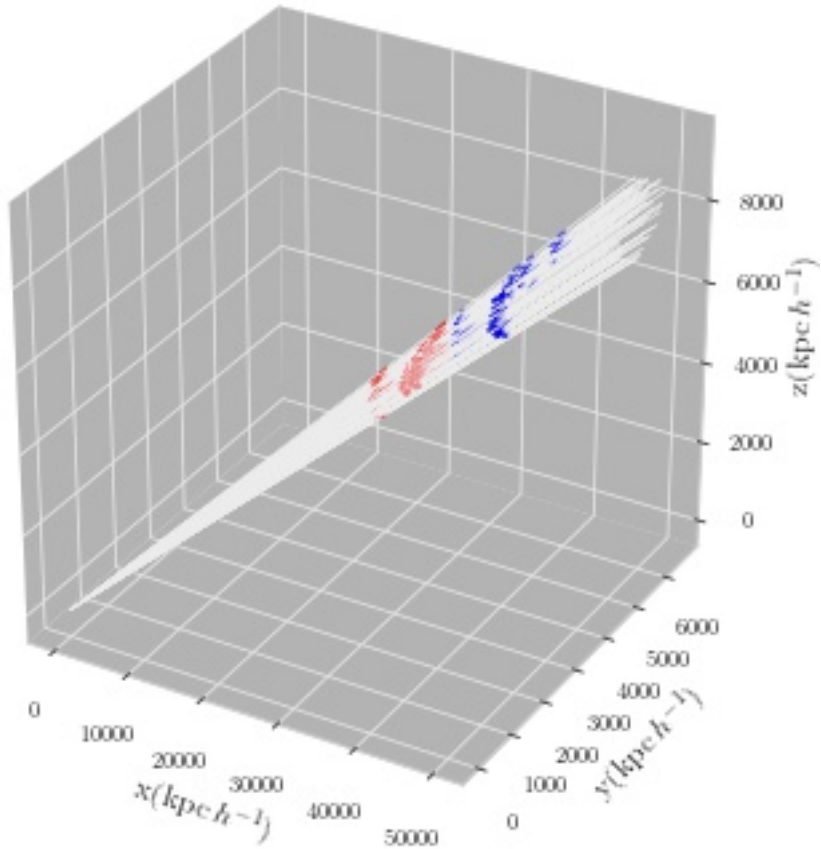


(a) Figure showing the light rays coloured by the direction of highest density when searching with a radius of 5 Mpc. Red indicates  $B_{LSS}$  in the direction of the observer; blue indicates field in the direction of the source and white indicates  $B_{LSS}$  perpendicular to the LOS.

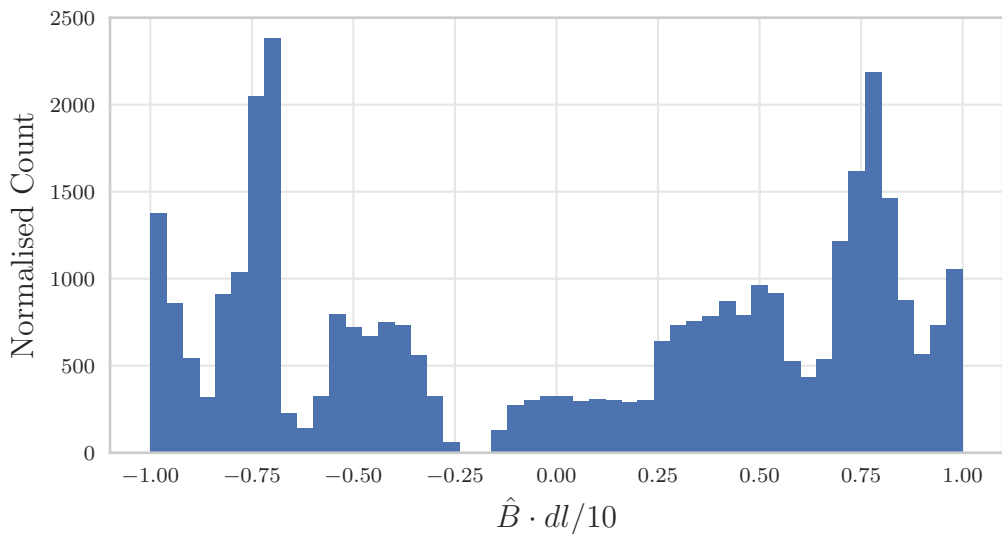


(b) Histogram showing the range of directions found in the cone when the searching radius is 5 Mpc. On the x-axis, 1 indicates  $B_{LSS}$  in the direction of the observer and -1 indicates field in the direction of the source.

**Figure 4.7:** Figure showing the directions of the steps along the light rays in the first section of the simulation for a searching radii of 5 Mpc. At a larger searching radius, more distinct structure is identified.



(a) Figure showing the light rays coloured by the direction of highest density when searching with a radius of 10 Mpc. Red indicates  $B_{\text{LSS}}$  in the direction of the observer; blue indicates field in the direction of the source and white indicates  $B_{\text{LSS}}$  perpendicular to the LOS.



(b) Histogram showing the range of directions found in the cone when the searching radius is 10 Mpc. On the x-axis, 1 indicates  $B_{\text{LSS}}$  in the direction of the observer and -1 indicates field in the direction of the source.

**Figure 4.8:** Figure showing the directions of the steps along the light rays in the first section of the simulation for a searching radii of 10 Mpc. The directions found at this radius are similar to those of the 5 Mpc searching radius.

as it does of showing us a negative signal and so it is, as expected, a low signal compared to the  $B_{\text{Aligned}}$  field.  $B_{\text{Random}}$  provides a lower-limit of sorts because any realistic signal will have some mutual alignment between rays for some sections of the ray and so the expectation is that  $B_{\text{LSS}}$  has a higher correlation. The SF amplitude for  $B_{\text{LSS}}$  sits between the SFs for  $B_{\text{Aligned}}$  and  $B_{\text{Random}}$ .

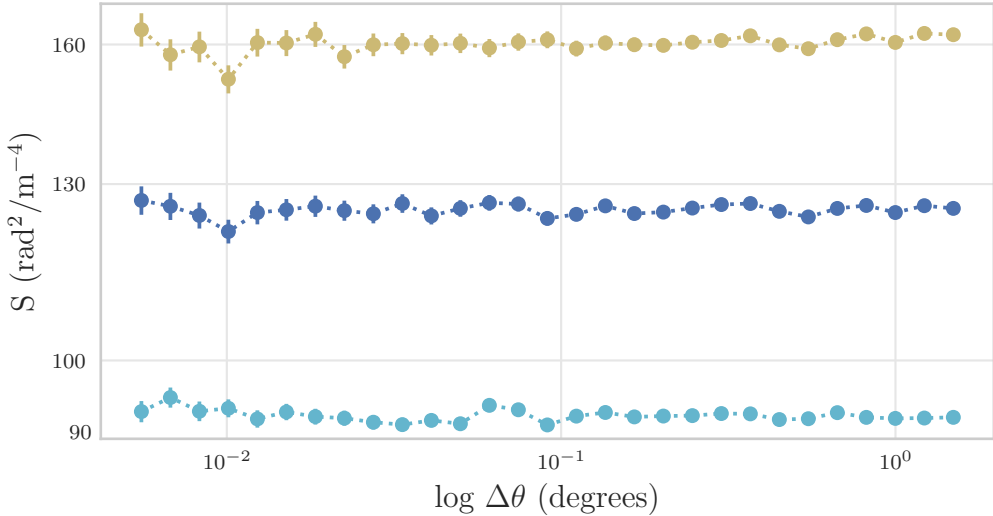


**Figure 4.9:** Comparison of SF with  $B_{\text{LSS}}$  (dark blue), SF with  $B_{\text{Random}}$  (light blue) and SF with  $B_{\text{Aligned}}$  (yellow).

Figure 4.10 shows the SFs scaled to the same order of magnitude to compare the shapes more easily. The slope of  $B_{\text{Aligned}}$  should reflect some of the underlying structure in the simulation, and so it is not promising that the slope appears to be flat. Seeing this, however, it is not surprising that the other two directional SFs look flat (we already know that the  $SF_{S+E}$  is a flat function, as we discussed in Section 4.3). The extra noise in the SF around  $0.1^\circ$  could indicate that the structure is adding power at these angular separations and the fact that the aligned field shows the most noise supports this possibility.

We fit a power law to the SFs to quantify the difference between the slopes, and find the amplitude and index of the fit according to the discussion in Section 4.3. The results of that fit are shown in Figure 4.11 where the increase in nonlinearity in Figure 4.10 has led to an increased error on the slope for the SFs with  $B_{\text{LSS}}$  and  $B_{\text{Aligned}}$ .

## 4.5 Effect of the RM<sub>LSS</sub> on the Structure Function

We combine  $\text{RM}_{\text{Source}}$ ,  $\text{RM}_{\text{Error}}$  and  $\text{RM}_{\text{LSS}}$  where  $B_{\text{LSS}}=10 \text{ nG}$  with a 5 Mpc searching radius. We plot the final RM values in Figure 4.12. The size of the circles is determined by the relative magnitude of the RM, and the colour is determined by the sign, where blue indicates positive RM and red indicates a negative RM. This plot is comparable to a small section of all-sky RM maps such as those seen in Figure 1.3.

We derive a SF from these RM measurements ( $SF_{\text{Tracing LSS}}$ ) as shown in Figure 4.13. We can see that the amplitude is greatly changed, but the slope is still similar despite

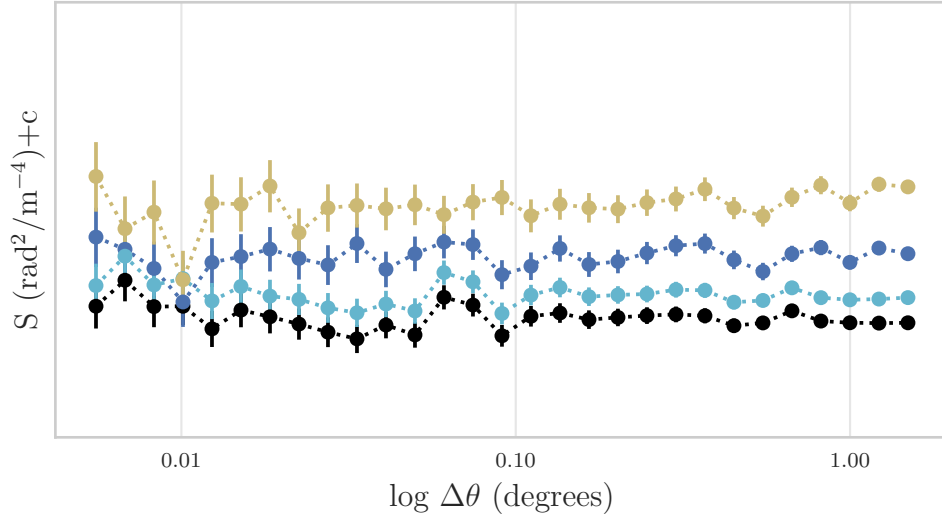


**Figure 4.10:** Comparison of  $SF_{S+E}$  (black) against the SF with  $B_{\text{LSS}}$  (dark blue), SF with  $B_{\text{Random}}$  (light blue) and SF with  $B_{\text{Aligned}}$  (yellow), where  $c$  is an arbitrary shift in each curve that allows scaling for comparison.

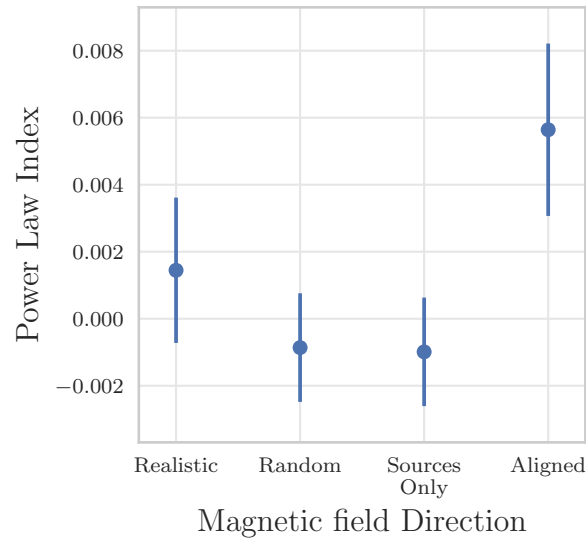


**Figure 4.11:** Comparison of the power law indices of the SFs for different magnetic field directions.

the extra signal in the SF. As discussed earlier,  $SF_{\text{Tracing LSS}}$  has significantly more noise around  $0.1^\circ$  than  $SF_{S+E}$ .

## 4.6 Adding in Galaxies

Up to this point, we have looked only at  $\text{RM}_{\text{Source}}$ ,  $\text{RM}_{\text{Error}}$  and  $\text{RM}_{\text{LSS}}$  and we showed a RM map of the expected observed RM if only  $\text{RM}_{\text{Source}}$ ,  $\text{RM}_{\text{Error}}$  and  $\text{RM}_{\text{LSS}}$  are present. We now consider  $\text{RM}_{\text{Galaxies}}$  to explore the effect that these have on the SF. This consideration is important because observations made in the future will have RM contributions from all of these signals, and we want to know whether it is possible to distinguish the

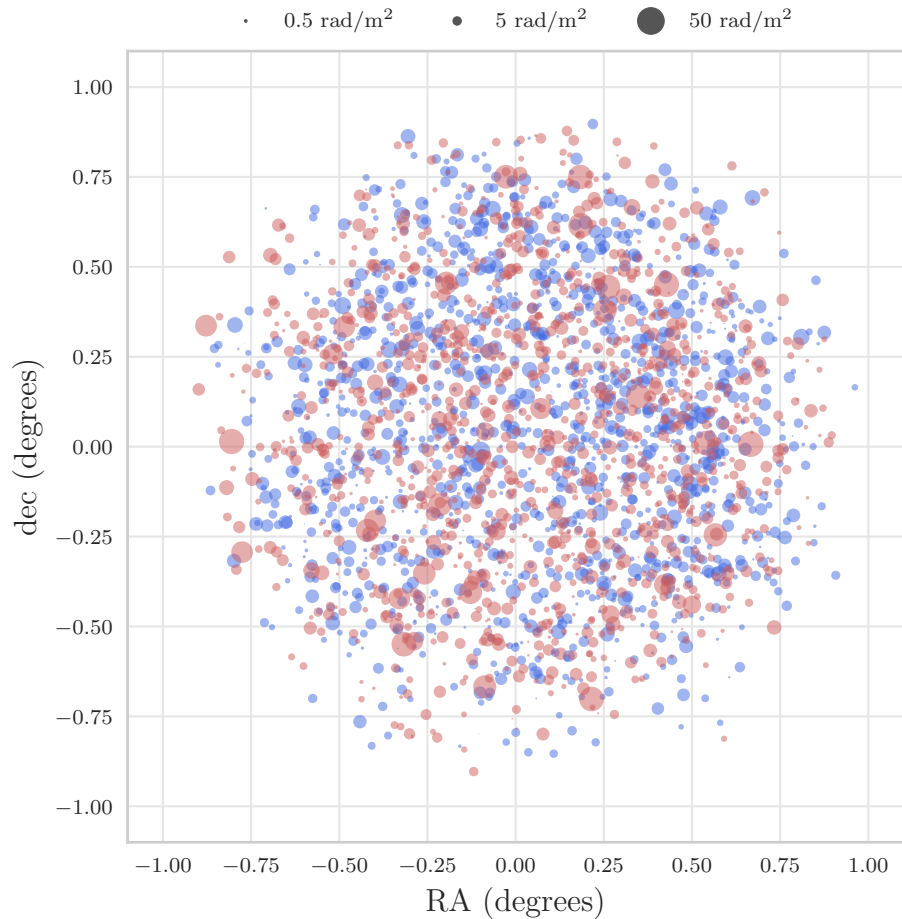


**Figure 4.12:** RM map of  $RM_{LSS} + RM_{Source} + RM_{Error}$ . Blue circles indicate positive RM, red circles indicate negative RM, and the size of the circles indicate the relative magnitude of the RM.

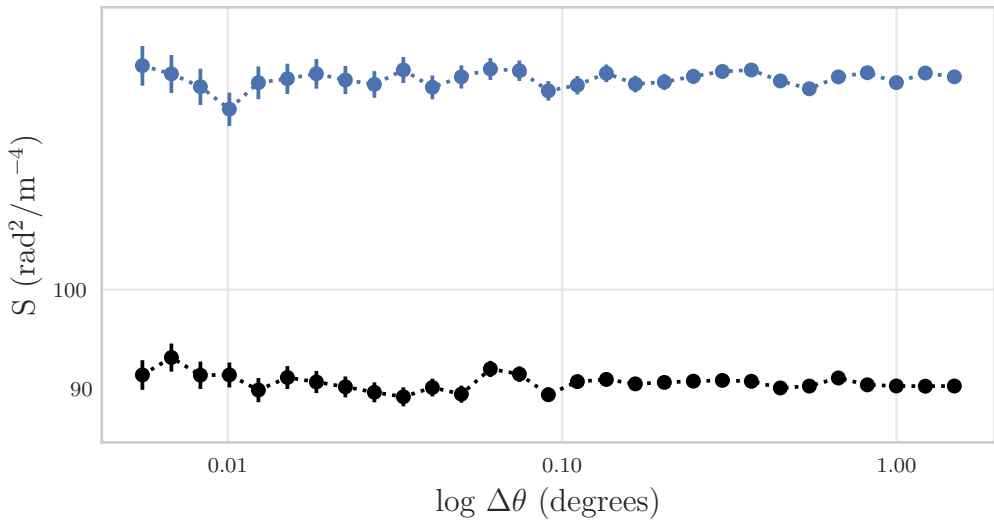


**Figure 4.13:** Comparison of  $SF_{S+E}$  (black) and  $SF_{Tracing\ LSS}$  (blue).

presence of  $RM_{LSS}$  in an observation.

Now that we have seen the effect of  $RM_{LSS}$  on the SF, we can look at the effect of

$\text{RM}_{\text{Galaxies}}$ . Since these galaxies follow the LSS, they may dominate the signal. Figure 4.14 shows the RM map when  $\text{RM}_{\text{Galaxies}}$  is added to the other signals ( $\text{RM}_{\text{Total}}$ ), and it is clear that some large RM signals have been detected along some light rays.

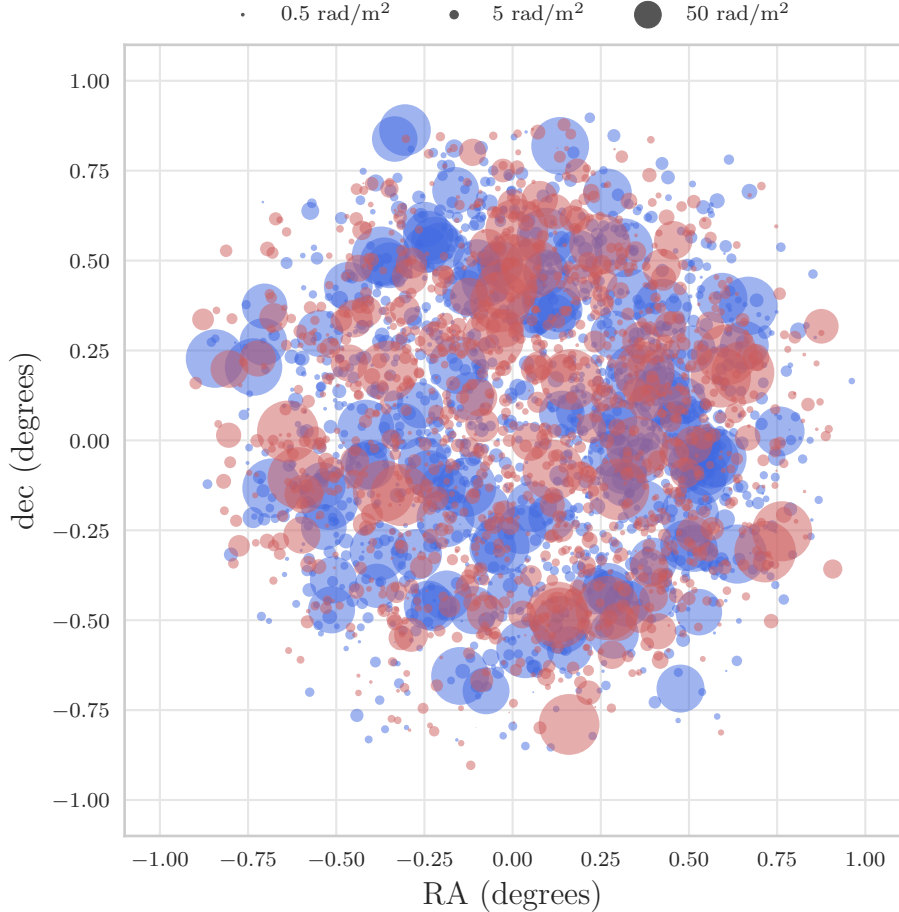


**Figure 4.14:** RM map of  $\text{RM}_{\text{Total}}$ . Blue circles indicate positive RM, red circles indicate negative RM, and the size of the circles indicate the relative magnitude of the RM.

The SF with only galaxies added to  $\text{SF}_{\text{S+E}}$  ( $\text{SF}_{\text{Tracing Galaxies}}$ ) is plotted against  $\text{SF}_{\text{S+E}}$  and the SF with all signals added together ( $\text{SF}_{\text{Total}}$ ) in Figure 4.15. It appears that the large signals in  $\text{RM}_{\text{Galaxies}}$  are randomly distributed enough to add a flat signal to the structure function.

Figure 4.16 shows the power law indices for  $\text{SF}_{\text{Tracing Galaxies}}$  and  $\text{SF}_{\text{Total}}$ .  $\text{RM}_{\text{Galaxies}}$  acts as a large source of noise and obscures the effect of  $\text{RM}_{\text{LSS}}$  on the power index. The power law index of the slopes is 0 within the error once  $\text{RM}_{\text{Galaxies}}$  is added.

## 4.7 Effect of the Strength of $B_{\text{LSS}}$ on $\text{SF}_{\text{Tracing LSS}}$

In Section 2.5 we discussed the expectations for the strength of magnetic fields in  $B_{\text{LSS}}$  which lie in the region of  $\sim 10$  nG. Figure 4.17 shows the effect on the SF when the

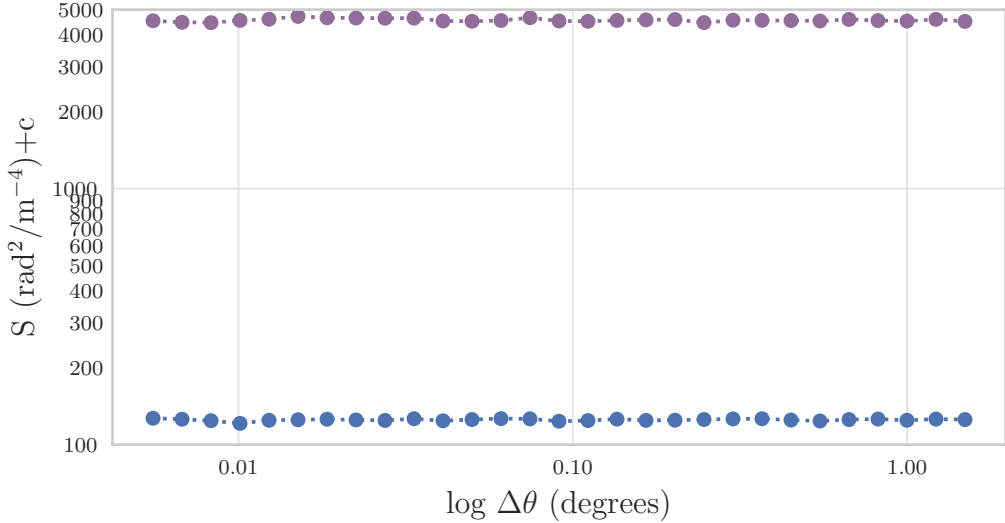


**Figure 4.15:** Figure showing the  $SF_{Tracing\ LSS}$ (blue) and  $SF_{Total}$ (purple).

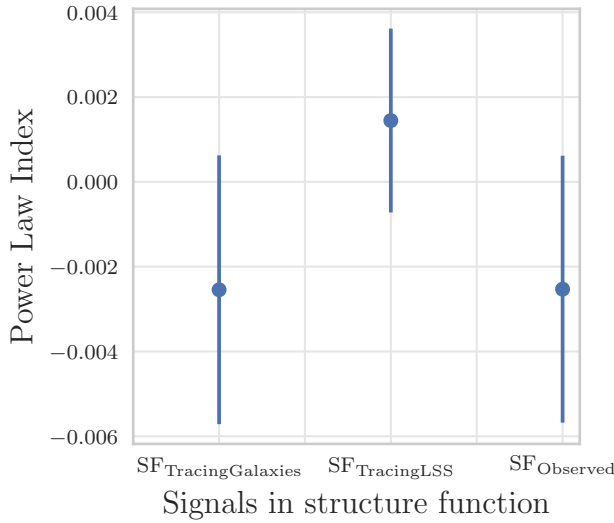


**Figure 4.16:** Figure showing the power law indices of  $SF_{Tracing\ Galaxies}$ ,  $SF_{Tracing\ LSS}$  and  $SF_{Total}$ .

strength is changed.

The effect of the changing the strength of  $B_{LSS}$  on the slope of  $SF_{Tracing\ LSS}$  is not immediately clear from the SFs, but there are some angular separations which show more power in certain bins when the field strength is increased. This makes  $SF_{Tracing\ LSS}$  less flat than  $SF_{S+E}$ . Figure 4.18 shows the effect on  $SF_{Tracing\ LSS}$  when the strength is changed, scaled to improve comparison. It is clear that the shape of the SF becomes less flat with increased magnetic field strength.

To quantify how the SF changes for different magnetic field strengths, we again use the power-law fit to  $SF_{Tracing\ LSS}$  function. This power law fit lets us obtain Figure 4.19 which shows the power law indices of  $SF_{Tracing\ LSS}$  for each magnetic field strength. There is little difference between the slopes for magnetic fields at 1 nG and 10 nG, but these slopes are higher than that of a 100 nG field or the  $SF_{S+E}$ . It is clear that the index can

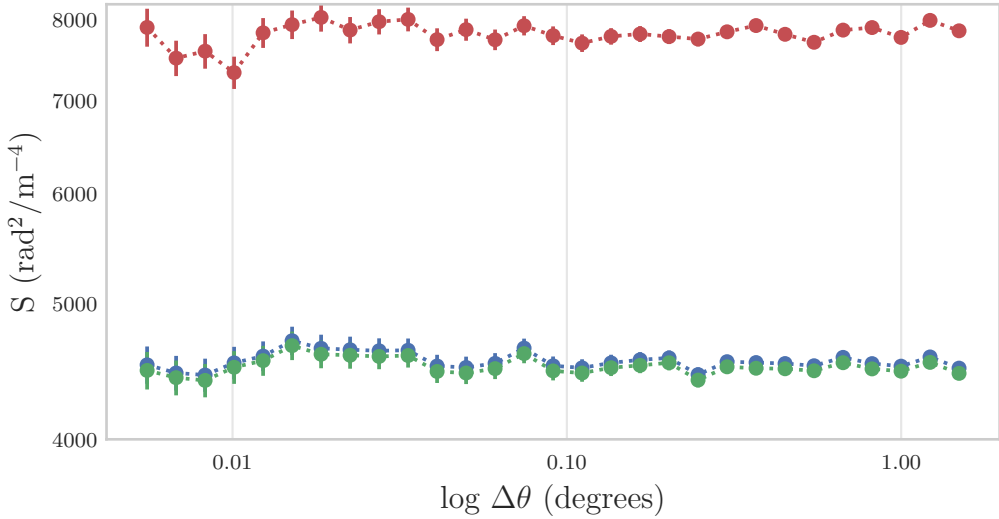


**Figure 4.17:** Comparison of  $SF_{\text{Tracing LSS}}$  for  $B_{\text{LSS}} = 100 \text{ nG}$  (red),  $B_{\text{LSS}} = 10 \text{ nG}$  (blue) and  $B_{\text{LSS}} = 1 \text{ nG}$  (green).

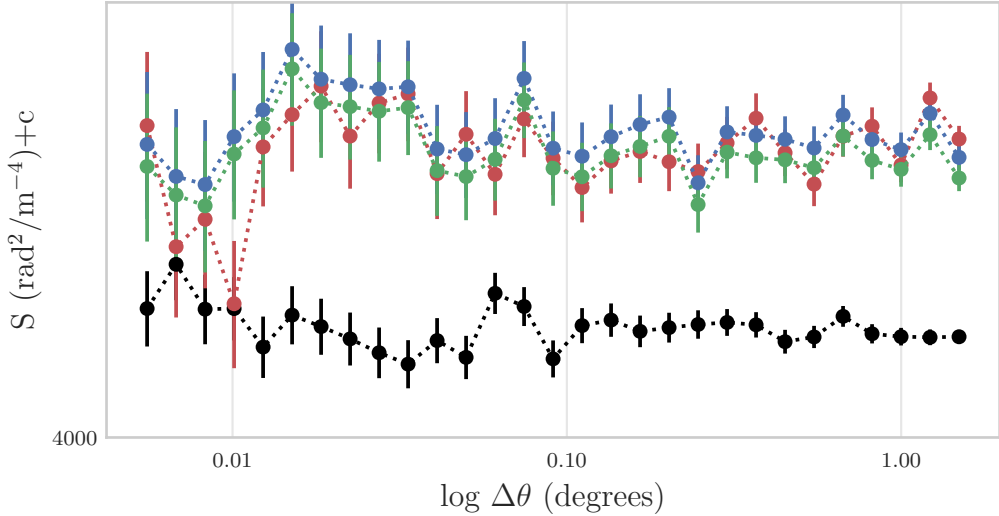


**Figure 4.18:**  $SF_{\text{Tracing LSS}}$  for  $B_{\text{LSS}} = 100 \text{ nG}$  (red),  $B_{\text{LSS}} = 10 \text{ nG}$  (blue) and  $B_{\text{LSS}} = 1 \text{ nG}$  (green), here  $c$  is an arbitrary shift in each curve that allows scaling for comparison.

be affected by the presence of the LSS field, compared to  $SF_{S+E}$ .

## 4.8 Summary of the Structure Function Analysis

This exploration has shown us how  $SF_{\text{Tracing LSS}}$  is affected by the presence of  $B_{\text{LSS}}$  at different strengths. These results show that the power index is sensitive to the strength of the underlying field.

This chapter has also shown us that the field strength can impact on the index of the power law fit for strong enough fields. The direction of the underlying field also impacts the power law index. The next area of discussion explores how likely it is that we will be

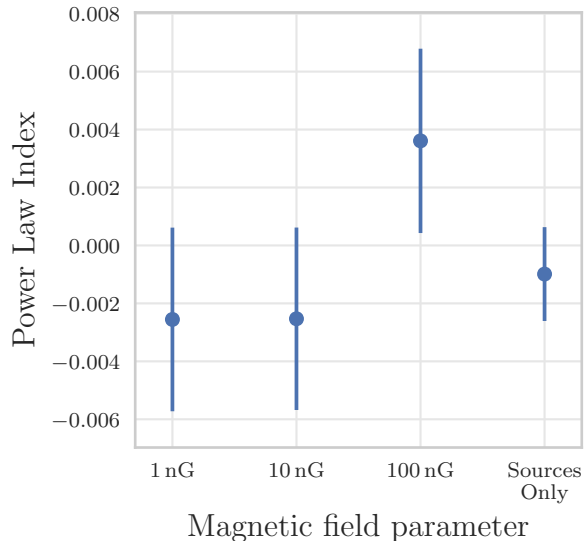


**Figure 4.19:** Comparison of the power law indices of  $SF_{Tracing}$  LSS for different strengths of  $B_{LSS}$ .

able to observe these fields. From this point forward, we assume a 10 nG magnetic field strength as we discussed in Section 2.5. The signal is very difficult to detect because of the weakness of the signal compared to the noise, so we need more sensitive detections.

# Chapter 5

## Detecting a Signal

In Chapter 4, we have discussed the possible SFs that we could expect to obtain with future observations, but there is still the question of whether we can conclusively determine, from observations alone, whether we are picking up a RM from the large-scale structure.

When dealing with real observed data,  $SF_{S+E}$  will not be known which means that we need to develop some approaches to detect if there is a signal from  $B_{LSS}$  present in the data. Since the  $SF_{S+E}$  will produce a flat SF, any significant deviation from a flat SF is evidence of a signal. The detectability of the  $RM_{LSS}$  is a function of  $RM_{Error}$ ,  $B_{LSS}$  and the number of sources observed.

Two methods to search for the signal from the LSS are to look for a change in the slope or to see if we can distinguish a difference in the ratio between signal and errors in the SF before and after the  $RM_{LSS}$  is added.

### 5.1 Random Permutation Test

In order to test the significance of the signal that we have observed, we need to see how this signal compares to a null hypothesis that there is no relationship between the positions and the RM signal at those positions. We do this by testing how likely it is that this signal would be found by some random permutation of the data. We do this using a random permutation, or shuffle, test. In this test, we shuffle the RM signals between the observed positions and recalculate the SF. If we do this many times and calculate the slope for each SF, we obtain a distribution of slopes.

We can plot a histogram of the resulting distribution and derive a p-value to determine the significance of what we see in our data. A p-value will lie between 0 and 1, and in this case, it represents the probability of finding a steeper slope than the one that is observed. Since we have both positive and negative slopes, we will use a 2-sided test and so the p-value is calculated by determining what fraction of values lie outside the measured value in the distribution. Small p-value ( $p \leq 0.05$ ) will indicate that our signal is significantly different from a null hypothesis (T. Hey and P. Walters, 1988).

We performed this test for the signals that we explored in Chapter 4 where the magnetic field strength is  $\sim 10$  nG and randomly reassign the observed RM signals to the angular positions 1000 times. Figure 5.1 shows the distribution of amplitudes and power

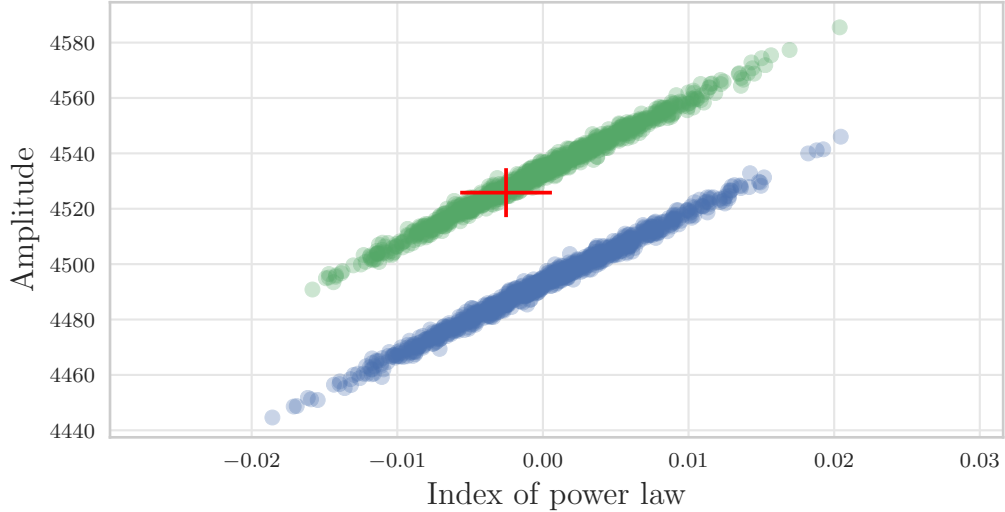


**Figure 5.1:** Distribution of indices and amplitudes of the SF from shuffled values of RM<sub>Tracing Galaxies</sub> (blue), RM<sub>Total</sub> (green) and the value from our observations (red) at an observational error of 2 μJy. This plot shows the range of amplitudes and power indices that could be produced from a random combination of the RM measurements. We see that RM<sub>LSS</sub> affects the amplitudes of the possible SFs, but the values that we have measured are not significant within this distribution

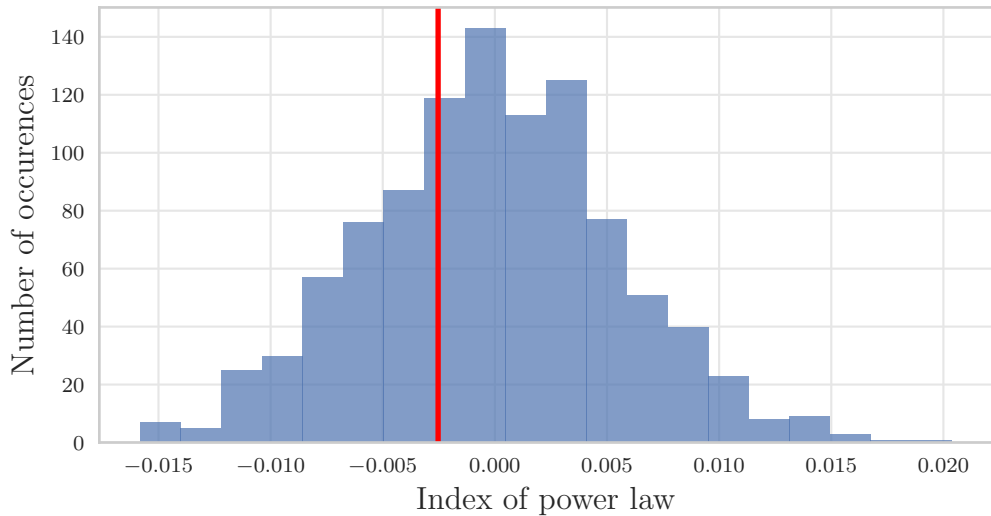


**Figure 5.2:** Histogram of indices of the SF from shuffled values of RM<sub>Total</sub> and the power index from our observations (red) at an observational error of 2 μJy

law indices ( $a, k$  in Equation 4.6) that are fit to the SFs of the shuffled data and how the index and amplitude in SF<sub>Total</sub> compares. Figure 5.2 shows where our index compares to those that are sampled and the p-value is 0.33 which indicates that there is no significant slope to the SF in this case.

## 5.2 Ratio of Signals and Noise

To test for the presence of a signal from the variance of the distributions we calculate the ratio between the signal's deviation from the mean ( $S - \langle S \rangle$ ) and the error on the mean

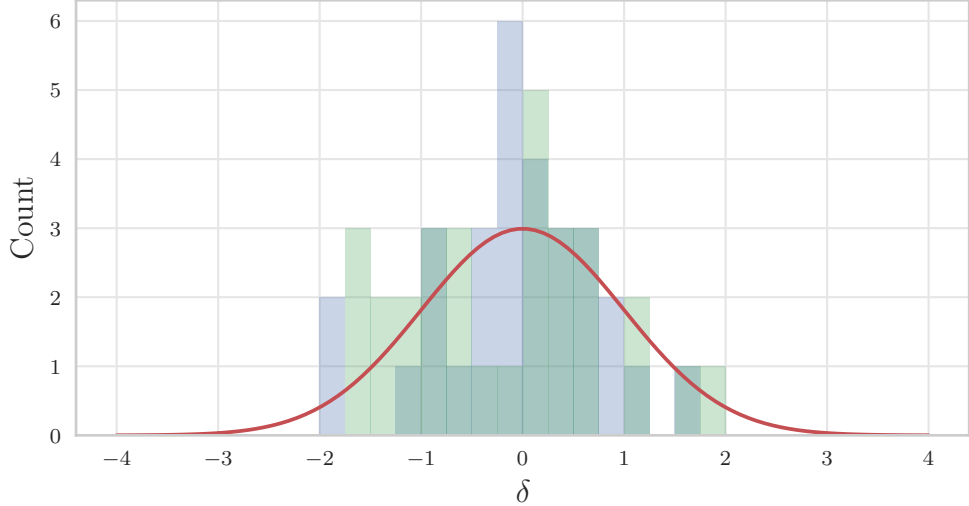


**Figure 5.3:** Histograms of  $\delta$  for  $SF_{Source\ Only}$  (blue) and  $SF_{S+E}$  (green) and a Gaussian distribution with  $\sigma = 1$  and  $\mu = 0$  and area under the curve equal to the number of bins  $\Delta\theta$  in the SFs (red).

$(\sigma_\mu)$  for each  $\Delta\theta$  bin in the SF. By calculating  $\delta = \frac{S - \langle S \rangle}{\sigma_\mu}$ , we can quantify how the signal that has been added to the SF differs from a pure noise signal. For the null hypothesis, we expect a normal error distribution in  $\delta$  with a standard deviation of 1. We should find that there is a higher standard deviation in the distribution of  $\delta$  in the SF when signals that are not purely noise are present.

Figure 5.3 shows the distribution of  $\delta$  from  $SF_{Source}$  and  $SF_{S+E}$ . Adding  $RM_{Error}$  to  $RM_{Source}$  does not affect the  $\sigma$  of the histogram of  $\delta$  since  $RM_{Error}$  changes the amplitude of the SF uniformly. The results of these plots indicate that  $\delta_{Source\ Only}$  has  $\sigma = 0.77$  and  $\mu = -0.082$  while  $\delta_{S+E}$  has  $\sigma = 1.25$  and  $\mu = -0.24$ .

To determine what constitutes a significant deviation from this  $\sigma$ . We re-sampled  $RM_{Source} + RM_{Error}$  500 times and then calculated  $SF_{S+E}$  for each of these. We calculated the distribution of  $\delta$  for each test and calculated the resultant  $\sigma$  values. This distribution of  $\sigma$  is shown in Figure 5.4. The mean of this distribution is  $\bar{\sigma} = 1.15$  and the standard deviation is  $s = 0.38$ . For any  $\sigma$  found in the other SFs, we can calculate a p-value from the distribution in Figure 5.4 to determine if it is significant.

The effect of the change in the  $\sigma$  of the histogram of  $\delta$  when we add  $RM_{LSS}$  is not clear when we compare the histograms of  $\delta_{Tracing\ Galaxies}$  and  $\delta_{Total}$  in Figure 5.5.  $\delta_{Tracing\ Galaxies}$  has  $\sigma = 1.04$  and  $\mu = -0.21$  while  $\delta_{Total}$  has  $\sigma = 1.05$  and  $\mu = -0.21$ . The p-value for  $\delta_{Tracing\ Galaxies}$  is 0.56 and the p-value for  $\delta_{Total}$  is 0.54 which indicates that the  $\sigma$  is not significantly different between these distributions and neither is significant.

### 5.3 Effect of Removing High-RM sources

We know from Chapter 4 that a small number of galaxies intersect light rays, but that they can produce large RM values. The presence of these large signals can increase the er-

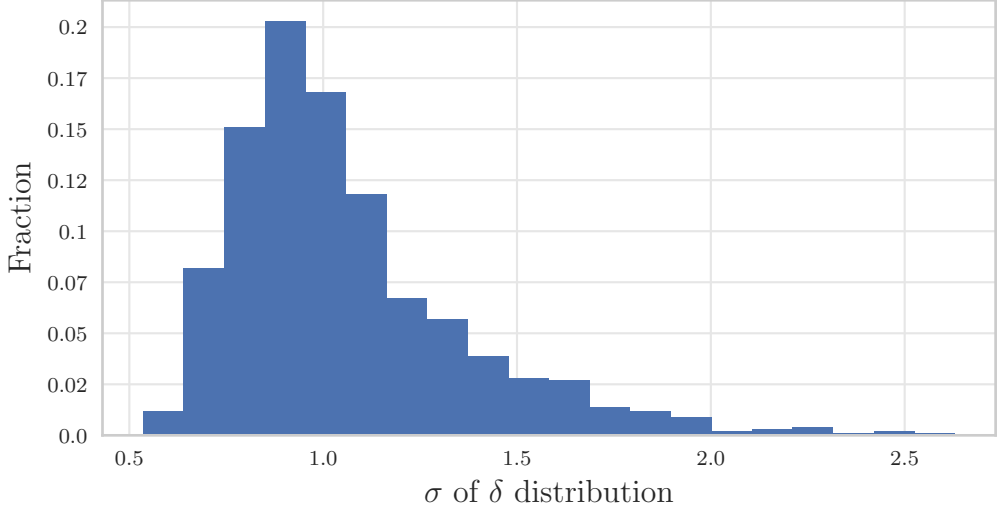


**Figure 5.4:** Distribution of  $\sigma$  of  $\delta$  for 1000 shuffles of  $RM_{S+E}$ .

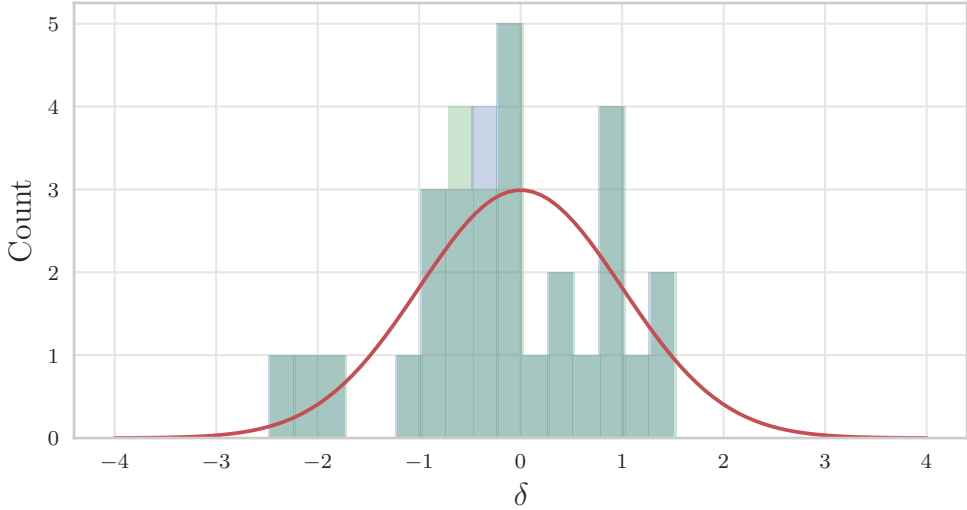
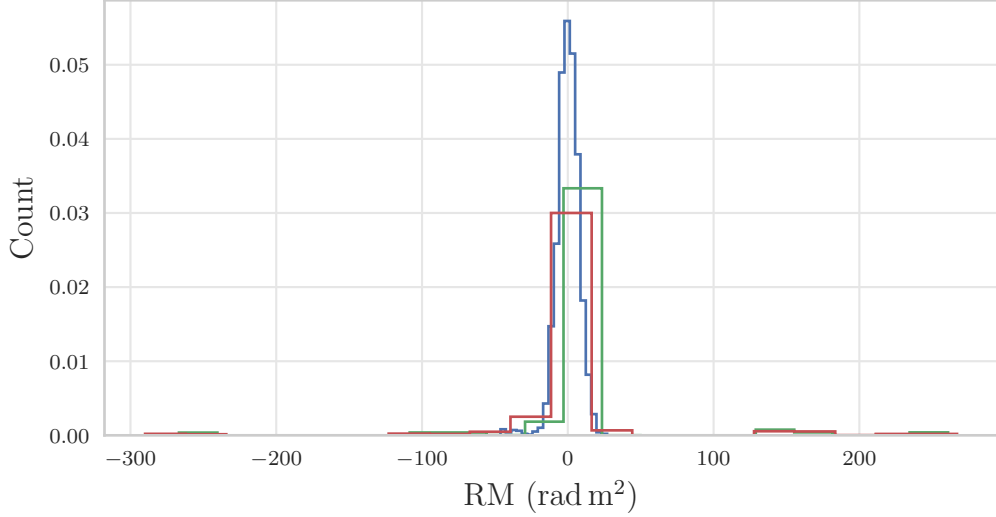


**Figure 5.5:** Histogram of  $\delta$  for  $SF_{Tracing\ Galaxies}$  (blue) where  $\sigma$  has a p-value of 0.56,  $SF_{Total}$  (green) where  $\sigma$  has a p-value of 0.54 and a Gaussian distribution with  $\sigma = 1$  and  $\mu = 0$  (red).

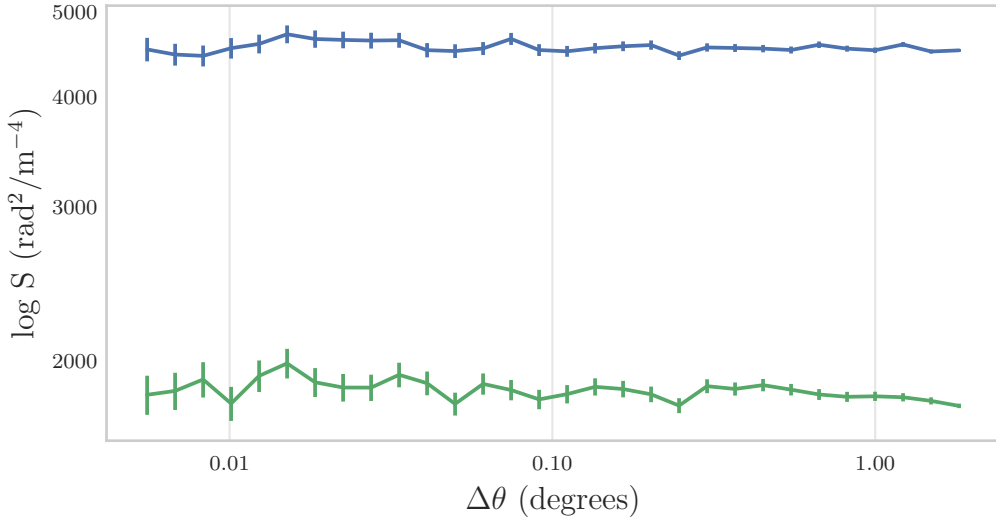
rror in the SF. Figure 5.6 shows the distribution of  $RM_{LSS} + RM_{Source} + RM_{Error}$ ,  $RM_{Galaxies}$  and  $RM_{Total}$ . It is clear that the spread of the signal from galaxies is much higher and appears to have some high and low RM outliers. These are likely from the rays that hit multiple galaxies since the magnetic fields in the LSS is not predicted to produce large RM values.

If we exclude all sources with  $RM_{Total} < -100 \text{ rad m}^{-2}$  and  $RM_{Total} > 100 \text{ rad m}^{-2}$ , we can plot a new SF which we show in Figure 5.7. The removal of  $|RM_{Total}| > 100$  has significantly lowered the amplitude of  $SF_{Total}$  and by removing those large RM-values, smaller structures are visible in the SF especially at smaller  $\Delta\theta$ . The large RMs caused there to be much more noise in each  $\Delta\theta$  bin in the SF and so the removal lowers the error per bin and makes the rest of the signal more easily detectable.

The resulting power indices from  $SF_{Total}$  before and after the galaxy cut is shown in



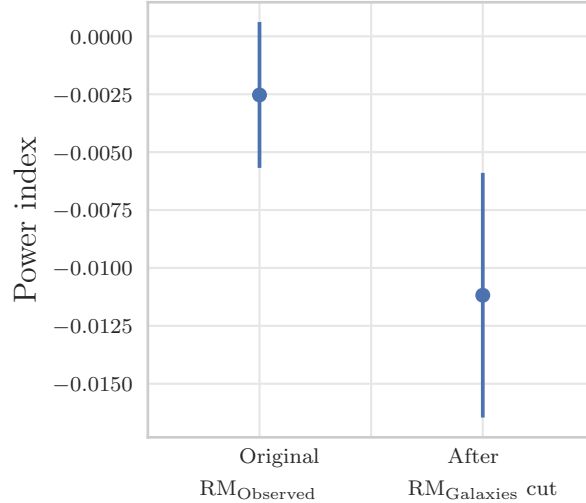
**Figure 5.6:** Histogram of  $RM_{LSS} + RM_{Source} + RM_{Error}$  (blue),  $RM_{Galaxies}$  (green) and  $RM_{Total}$  (red).



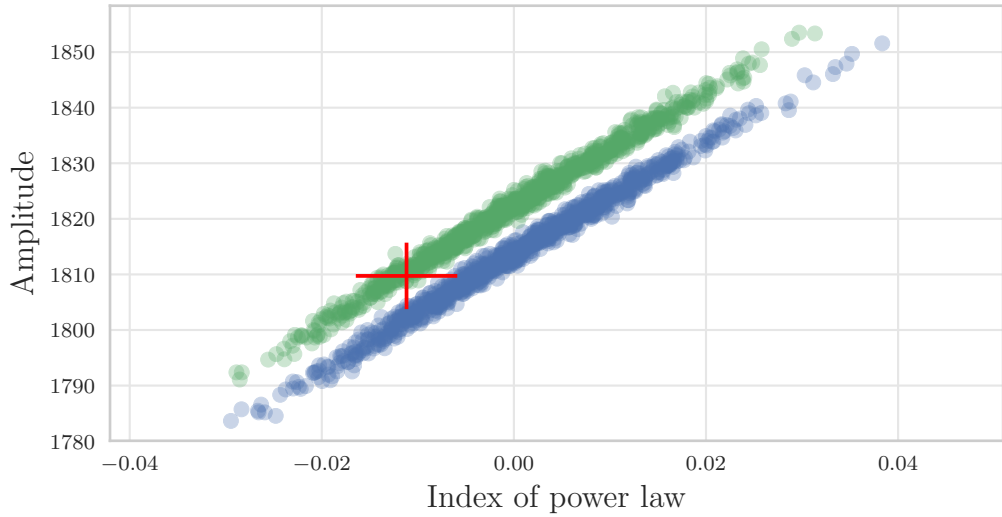
**Figure 5.7:** Comparison of  $SF_{Total}$  (blue) and  $SF_{Total}$  after we cut out all galaxy outliers of  $|RM_{Total}| > 100$  (green).

Figure 5.8 where the power index changes significantly, but the error on the power index is much higher. This is because removing the high-RM sources has allowed the fainter signal in the SF to show because there is less scatter. The SF looks less like a straight line once the faint signal is visible and the more variation in the SF, the higher the residuals of any linear fit.

It appears that finding any slope in the SF will be made easier by removing the highest RM sources but the error associated with the power index increases significantly for the less linear SF. It is also possible that there is no slope in the SF and that the signal that is observed will come from the variance in the SF. We can, however, do a shuffle test and this yields Figures 5.9 and 5.10. The p-value here is 0.14 which means that we still cannot detect a slope when removing the high-RM values, but that the significance of the result is much closer to being a detection than previous tests.



**Figure 5.8:** Comparison of power indices of  $SF_{Total}$  and  $SF_{Total}$  after we cut out all galaxy outliers of  $|RM_{Total}| > 100$  (green).



**Figure 5.9:** Distribution of indices and amplitudes of the shuffled values and our measured value after we cut out all galaxy outliers of  $|RM_{Total}| > 100$ . See Figure 5.1 for details.

If we are looking for non-linear signals then removing the high-RM galaxies should help us to detect RM<sub>LSS</sub> and this is confirmed by Figure 5.11.

If we attempt to check the ratio  $\delta$  for the SFs before and after removing high-RM sources, we get Figure 5.12 where  $\delta_{Total}$  has  $\sigma = 1.05$  and  $\mu = -0.21$  before removing  $|RM_{Total}| > 100$  while  $\delta_{Total}$  has  $\sigma = 1.64$  and  $\mu = -0.42$  after the removal. The value of  $\sigma$  for  $\delta_{Total}$  after removing  $|RM_{Total}| > 100$  lies outside the error of  $\delta_{S+E}$  but the p-value is 0.071 so although the  $\sigma$  is so large, it does not fall within the significance threshold of  $p \leq 0.05$ .

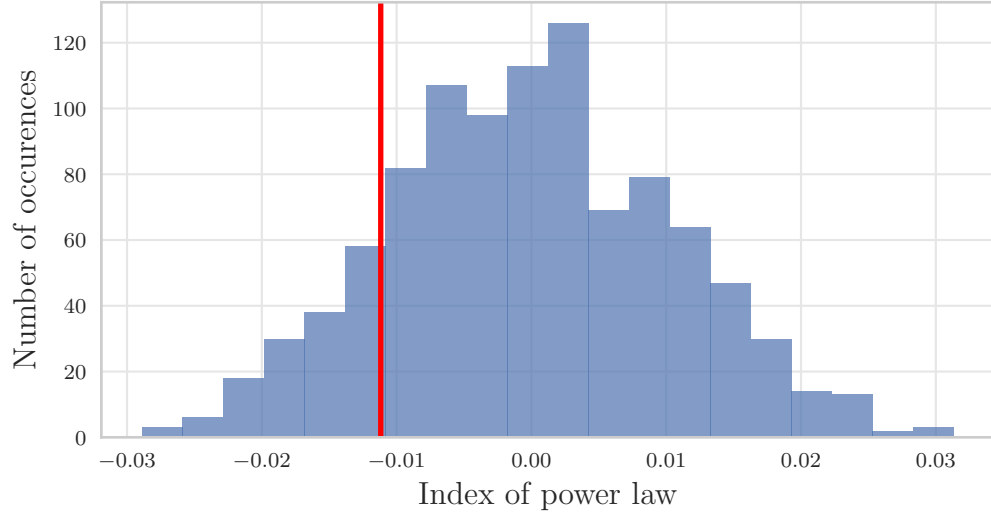


**Figure 5.10:** Histogram of indices of the shuffled values and our measured value , after we cut out all galaxy outliers of  $|RM_{Total}| > 100$ .

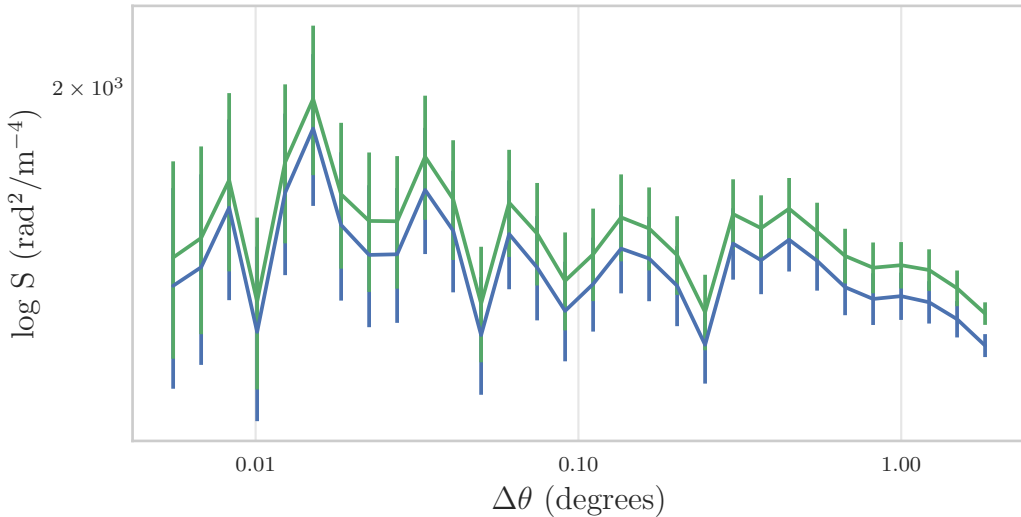


**Figure 5.11:** Comparison of  $SF_{Tracing \text{ Galaxies}}$  after we cut out all galaxy outliers of  $|RM_{Total}| > 100$  (blue) and  $SF_{Total}$  after we cut out all galaxy outliers of  $|RM_{Total}| > 100$  (green).

## 5.4 Effect of Improving RM<sub>Error</sub>

Up to this point, we have been working with an error of  $2 \mu\text{Jy}$  because this is the error expected for the wide-field surveys. If we use all of the sources that we observe and go down to an error of  $0.1 \mu\text{Jy}$  which is expected for the MIGHTEE deep field, we can reduce the noise in the SF and better see the signal. It should be noted that more sources would be seen at the lower noise, but we will compare the results here with the same sources. We will call the RM contribution from this new error  $RM_{0.1}$  and this error is compared to the wide-field error and  $RM_{\text{Source}}$  in Figure 5.13.

If we perform the shuffling once again, we obtain Figure 5.14 and Figure 5.15 where the p-value is 0.34 which is slightly larger than that of the wide-field error. This implies that there is a signal that is dwarfing the observational error, and this is likely to come

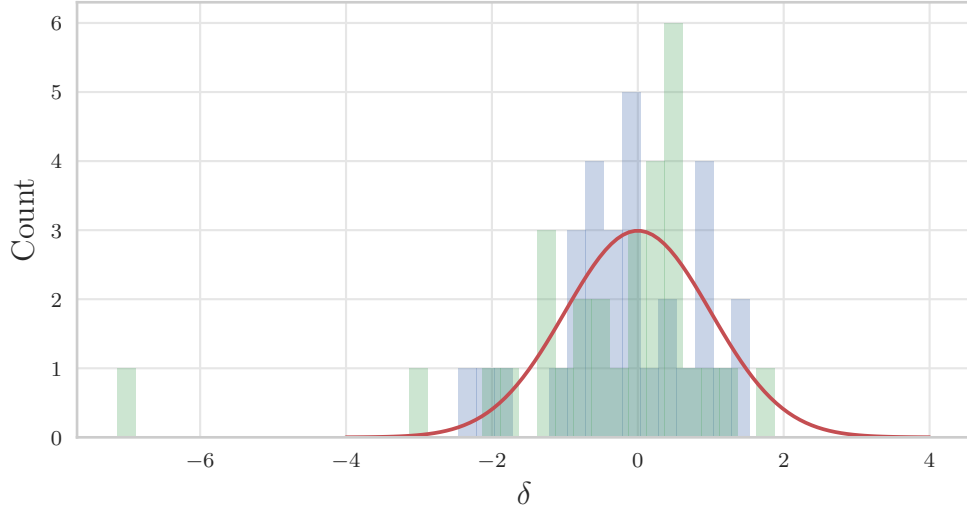


**Figure 5.12:** Histogram of  $\delta$  for  $SF_{Total}$  (blue) where  $\sigma$  has a p-value of 0.54,  $\delta$  for  $SF_{Total}$  after we cut out all galaxy outliers of  $|RM_{Total}| > 100$  (green) where  $\sigma$  has a p-value of 0.071 and a Gaussian distribution with  $\sigma = 1$  and  $\mu = 0$  (red).

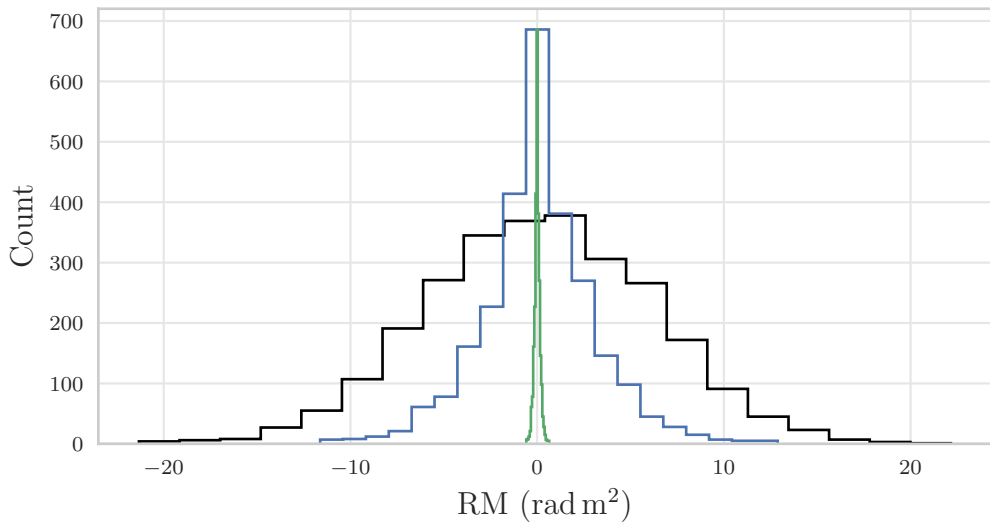


**Figure 5.13:** Histogram of  $RM_{Source}$  (black),  $RM_{Error}$  (blue) and  $RM_{0.1}$  (green).

from the galaxy signals based on Chapter 4.

We can check  $\delta$  for an observational error of  $0.1 \mu\text{Jy}$  but since the error does not change the spread of  $\delta$ , this method is unlikely to show any difference with a lower observational error. This is confirmed in Figure 5.16 where  $\delta_{Total}$  has  $\sigma = 1.05$  and  $\mu = -0.21$  at an observational error of  $2 \mu\text{Jy}$  and  $\delta_{Total}$  has  $\sigma = 1.03$  and  $\mu = -0.20$  at an observational error of  $0.1 \mu\text{Jy}$ . The p-value for  $\delta_{Total}$  is 0.554 at an observational error of  $2 \mu\text{Jy}$  and the p-value for  $\delta_{Total}$  is 0.49 at an observational error of  $0.1 \mu\text{Jy}$ . The significance of  $\sigma$  has barely changed with lower error, and it has not improved.

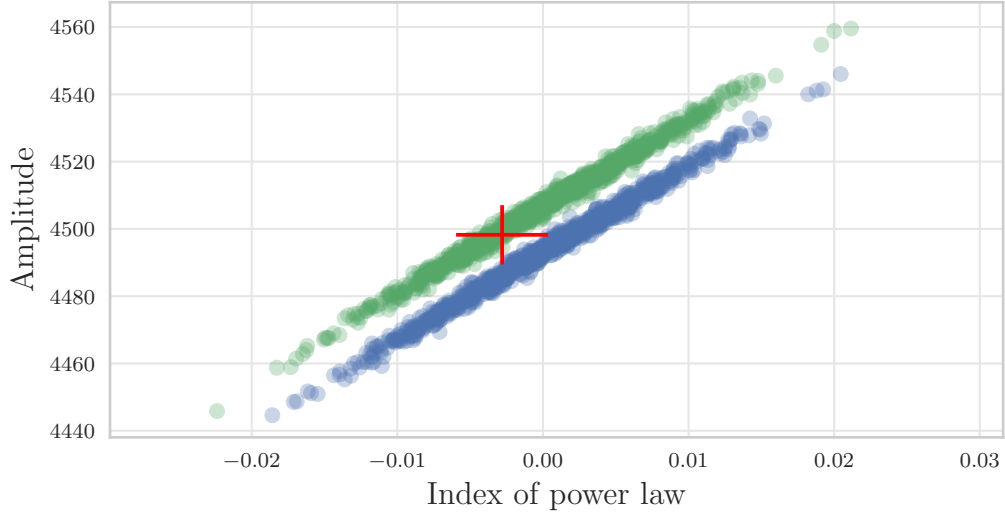


**Figure 5.14:** Distribution of indices and amplitudes of the SF from shuffled values of  $RM_{\text{Tracing Galaxies}}$  (blue),  $RM_{\text{Total}}$  (green) and the value from our observations (red) at an observational error of  $0.1 \mu\text{Jy}$ . See Figure 5.1 for details.

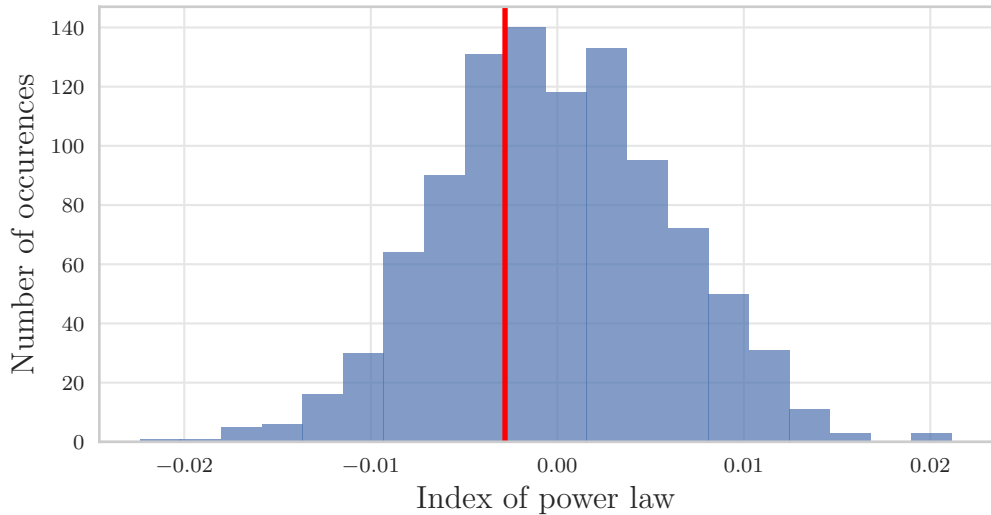


**Figure 5.15:** Histogram of indices of the SF from shuffled values of  $RM_{\text{Total}}$  and the power index from our observations (red) an observational error of  $0.1 \mu\text{Jy}$ .

## 5.5 Detectability of a stronger field

We can also investigate the shuffling test for a 100 nG field and obtain Figure 5.17 and Figure 5.18. The p-value here is 0.29 which indicates that it will not be possible to detect a slope with a stronger  $B_{\text{LSS}}$ .

At  $B_{\text{LSS}} = 100 \text{ nG}$ ,  $\delta$  looks slightly different.  $\delta_{\text{Tracing Galaxies}}$  has  $\sigma = 1.04$  and  $\mu = -0.21$  and  $\delta_{\text{Total}}$  has  $\sigma = 1.25$  and  $\mu = 0.20$  at an observational error of  $0.1 \mu\text{Jy}$ . The stronger field has an effect on  $\delta$ , but the p-value is 0.20 so the stronger field does not yield a significant detection.

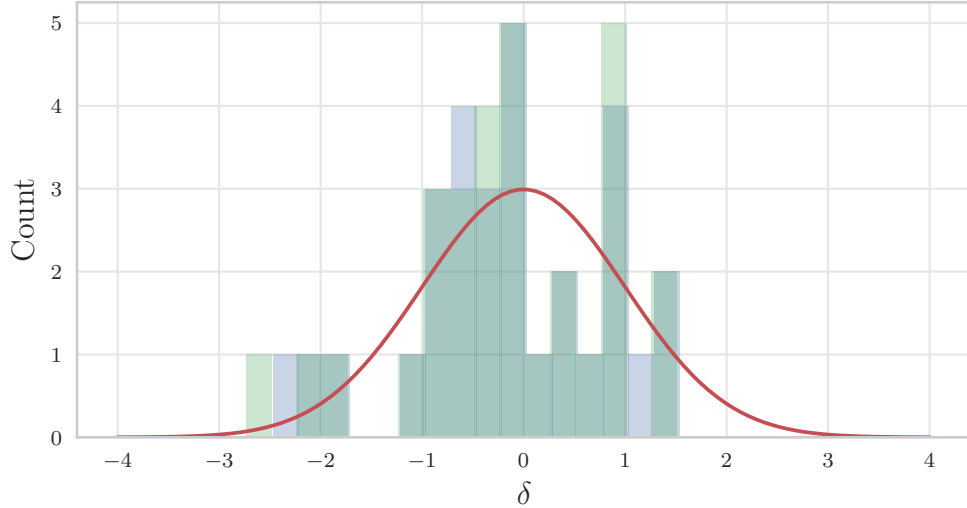


**Figure 5.16:** Histogram of  $\delta$  for  $SF_{Total}$  at an observational error of  $2 \mu\text{Jy}$  (blue) where  $\sigma$  has a p-value of 0.49,  $\delta$  for  $SF_{Total}$  at an observational error of  $0.1 \mu\text{Jy}$  (green) where  $\sigma$  has a p-value of 0.54 and a Gaussian distribution with  $\sigma = 1$  and  $\mu = 0$  (red).

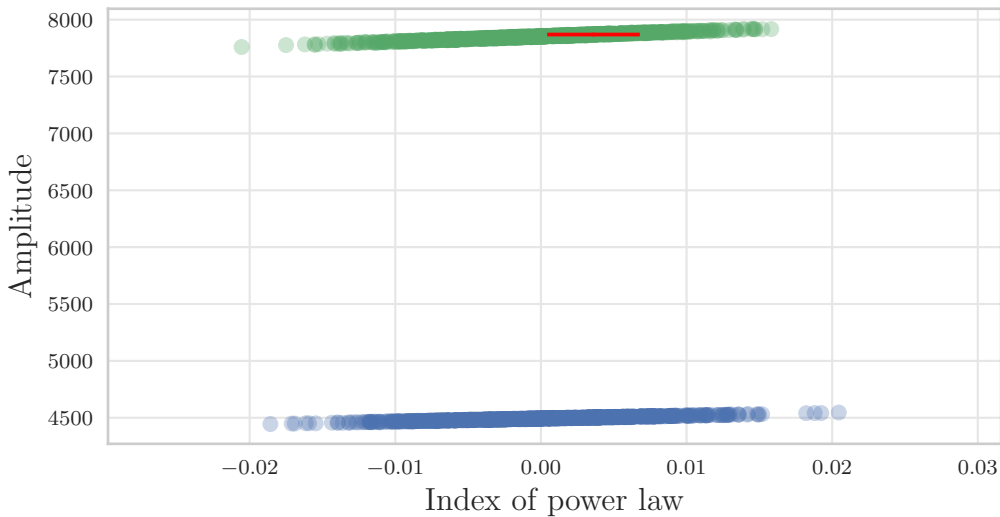


**Figure 5.17:** Distribution of indices and amplitudes of the shuffled values and our measured value, with an observational error of  $2 \mu\text{Jy}$  and  $B_{LSS} = 100 \text{ nG}$ . See Figure 5.1 for details.

## 5.6 Error on fitting a line

Variance in the SF can be an indicator of how much power is being added at distinct  $\Delta\theta$  values rather than across the SF. If we use the error on the power index as a measure of the variance, we obtain the errors shown in Table 5.1 which shows that the lower value of  $\sigma_n$  in the deep fields should increase the amount of signal that we see in the structure function. Removing the high-RM outliers in the observed signal also reveals a lot more power at distinct  $\Delta\theta$  values and to the same degree as a stronger magnetic field would reveal.

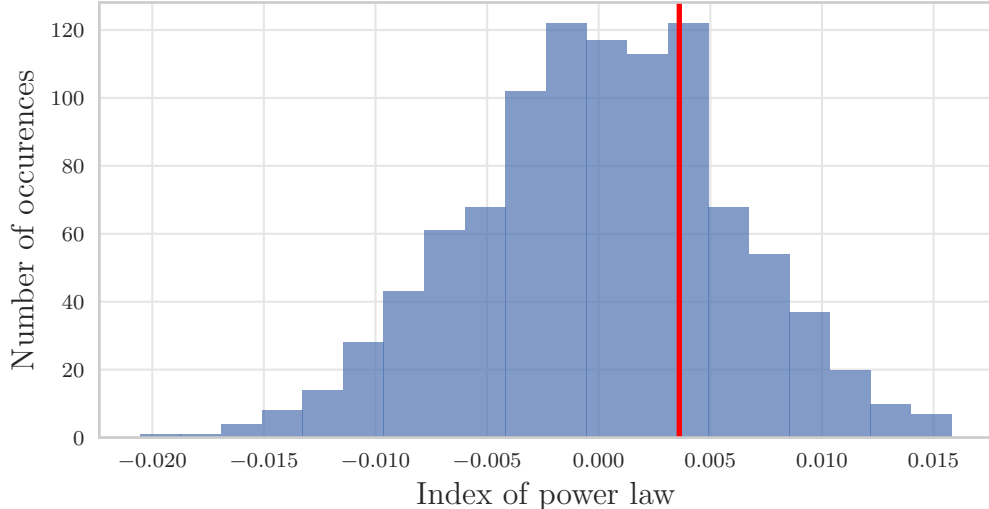


**Figure 5.18:** Histogram of indices of the shuffled values and our measured value, with an observational error of  $2\mu\text{Jy}$  and  $B_{\text{LSS}} = 100 \text{ nG}$ .

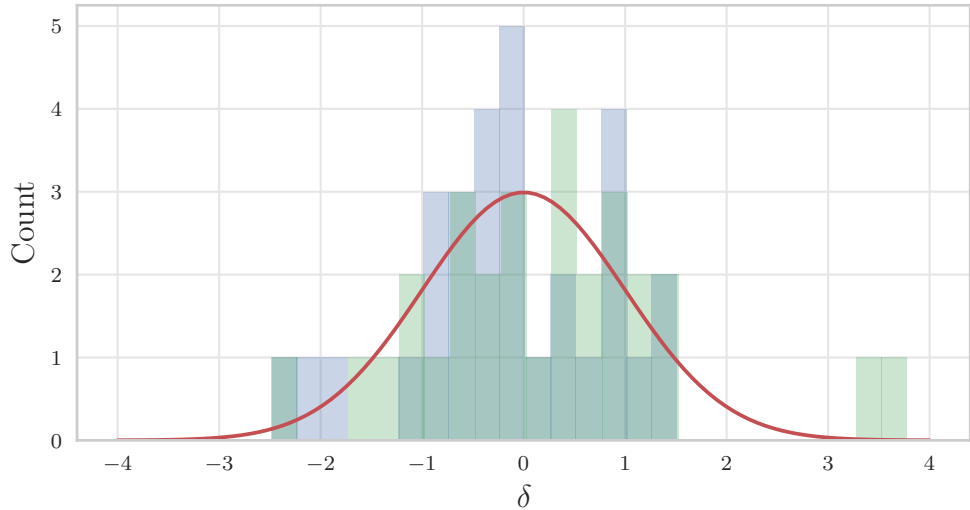


**Figure 5.19:** Histogram of  $\delta$  for  $SF_{\text{Tracing Galaxies}}$  (blue) where  $\sigma$  has a p-value of 0.56,  $\delta$  for  $SF_{\text{Total}}$  when  $B_{\text{LSS}} = 100 \text{ nG}$  (green) where  $\sigma$  has a p-value of 0.20 and a Gaussian distribution with  $\sigma = 1$  and  $\mu = 0$  (red).

**Table 5.1:** Comparison of the error on the power index for different detectability tests

| Test   | Power index | Power index Error |
|--|-------------|-------------------|
| $SF_{S+E}$   | -0.002556   | 0.001597          |
| $SF_{\text{Tracing Galaxies}}$   | -0.003186   | 0.003191          |
| $SF_{\text{Tracing LSS}}$  | 0.0007582   | 0.002112          |
| Original $SF_{\text{Total}}$   | -0.003161   | 0.003171          |
| $SF_{\text{Total}}$ when $ RM_{\text{Total}}  > 100$ removed           | -0.01141    | 0.005273          |
| $SF_{\text{Total}}$ with all sources and $\sigma_n = 0.1 \mu\text{Jy}$ | -0.003041   | 0.003184          |
| $SF_{\text{Total}}$ when $B_{\text{LSS}}=100 \text{ nG}$               | 0.012708    | 0.005678          |

# Chapter 6

## Discussion

Beginning with large-scale universe simulations, we constructed lightcones out to  $z = 1$  as a base for our model. We have developed a routine to trace the structure in the LSS, paint magnetic fields and construct RM observations to mirror the future observations that will be undertaken by the MIGHTEE project. We have simulated the magnetic fields that we expect to find in the LSS and investigated the effect that stronger, weaker and differently oriented fields would have on the SFs. We have considered the effect that observational error and galaxies will have on the SF and made calculations to predict these values.

We have also considered the possibility and challenges of disentangling the signal from  $\text{RM}_{\text{LSS}}$  from the other components of  $\text{RM}_{\text{Observed}}$ . The summary of results from the tests done to investigate this are shown in Tables 6.1 and 6.2.

We have considered that it may be possible to detect this signal as a slope, but have shown that a slope in the SF is either undetectable amongst the other signals or not present at all.

We have used the ratio  $\delta$  between  $S - \langle S \rangle$  and  $\sigma_\mu$  to measure whether the signal introduced by  $\text{RM}_{\text{LSS}}$  has noise-like variance or not. We see that noisy signals from  $\text{RM}_{\text{Source}}$  and  $\text{RM}_{\text{Error}}$  result in  $\sigma = 1.15 \pm 0.38$ .

We found that  $\text{RM}_{\text{Galaxies}}$  acted as a source of large error and so we found that removing the high and low RM outliers helped to reveal some of the underlying signals in the SF. This method yielded the largest  $\sigma$  in the  $\delta$  test but still not large enough to be a significant detection. The slope was not significant enough to discard the null hypothesis, but it was a much stronger detection than any of the others.

Considering a lower observational error was a way to look into the results that the deep-field surveys will see but, since we do not have the source counts expected for the

**Table 6.1:** Comparison of the p-value of the power-index for different shuffle tests

| Test  | Power index | p-value of power index |
|---|-------------|------------------------|
| Original $\text{SF}_{\text{Total}}$   | -0.003161   | 0.33                   |
| $\text{SF}_{\text{Total}}$ when $ \text{RM}_{\text{Total}}  > 100$ removed    | -0.01141    | 0.14                   |
| $\text{SF}_{\text{Total}}$ with all sources and $\sigma_n = 0.1 \mu\text{Jy}$ | -0.003041   | 0.34                   |
| $\text{SF}_{\text{Total}}$ when $B_{\text{LSS}}=100 \text{ nG}$               | 0.012708    | 0.29                   |

**Table 6.2:** Comparison the p-value of  $\sigma$  for the different  $\delta$  tests

| Test   | $\sigma$  | p-value |
|--|-----------|---------|
| SF <sub>S+E</sub>  | 1.15±0.38 | n/a     |
| Original SF <sub>Total</sub>                                     | 1.05      | 0.54    |
| SF <sub>Total</sub> when $ RM_{Total}  > 100$ removed            | 1.64      | 0.071   |
| SF <sub>Total</sub> with all sources and $\sigma_n = 0.1 \mu Jy$ | 1.03      | 0.49    |
| SF <sub>Total</sub> when $B_{LSS}=100 \text{ nG}$                | 1.25      | 0.20    |

deep field, this was a limited test. The change in error has no effect on the  $\delta$  test and only a small effect on the slope.

Raising the strength of the magnetic field does not improve the significance of the slope in the SF, but it does increase  $\sigma$  in the  $\delta$  test. Unfortunately,  $\sigma$  is still not large enough to fall outside of the error and so this is not a significant detection. Raising the magnetic field further would violate upper limit estimates in the literature.

The final check that we did was to look at the variance in fitting a straight line to the SF, since the less linear the SF, the higher the variance will be. We found that removing high-RM sources and increasing the magnetic field both gave higher variances and so this indicates that there was more signal at specific angular separations  $\Delta\theta$  rather than across the whole range.

The results of our tests indicate that the best method for detecting RM<sub>LSS</sub> would be to remove the sources in the observations with the highest or lowest RM-values so that the smaller-amplitude signals can be seen. The presence of B<sub>LSS</sub> may be detectable at the expected strength of 10 nG but our work shows that it will be difficult to determine the presence of a signal with a high degree of confidence.

## 6.1 Assumptions

This work is based on simulations and so is subject to limitations and assumptions as a result. Some of these limitations were due to time or computational limits and some were a result of the information that was available to us. It is likely that as computational methods and resources improve, many of these problems will be less significant.

The simulations represent gas, galaxies and halos as spherical which is a computational trade-off that most of the large simulations must make in order to be able to compute the evolution of their model within the memory constraints of their hardware. This choice means that there is no internal structure in the sources through which the light passes. In addition, it means that we model our radio galaxies as point sources rather than extended objects since there is no realistic shapes or morphology in the objects in the simulation.

To populate the sources, we needed to consider the galaxies in the simulation so that our sources are embedded in the large-scale structure. We originally intended to use a direct relation to go from the SFR of the galaxies in the simulation to radio luminosity measurements, but we found that the conversions from the literature yielded a RLF that overestimated the number of high-luminosity sources by a factor of 10. Although the

turnover was at the correct luminosity, the simulation underestimates the low-luminosity sources, and it does not match the RLFs exactly. This overestimate forced us to introduce a conversion factor between the RLF that we attained from sources in the  $z=0$  cube and the expected RLF at low redshift to yield the number of sources to match the observed RLF.

The magnetic fields in the galaxies and halos are assumed to be locally static and spherical. We only consider galaxies with SFR ( $M_{\odot} \text{yr}^{-1} > 0$ ), assuming that the rest are passive galaxies without a large-scale field. We find RM contributions by randomly sampling a distribution rather than using a model field. We did this because the magnetic field models that do exist for galaxies are complex and require more parameters than we have available. Observations of probes through galaxies also reveal patchy RM measurements with larger absolute values than the models predict, and so sampling from a distribution allows for the occasional large RM value.

Our rays passed through a significant number of halos but the current expectation for the magnetic field of a halo is a symmetrical x-shape and so a direction-dependent measurement like Faraday Rotation will largely cancel out along the path. We have therefore ignored the halos.

Turbulent fields are changing on small scales, and the field vectors point in every direction, so it is assumed that turbulent fields cancel out over the length of the ray. Therefore, we treat the signals that we see in our final RM as if they are from ordered fields in the gas and galaxies alone.

The sources of polarisation in this simulation are assumed to come only from the intrinsic polarisation of the sources and the ordered magnetic fields in the gas, galaxies and halos. We have ignored any polarisation that comes from dust or scattering because this should not be significant at the low frequencies observed.

The effect of redshift on the RM measurement has been assumed to be negligible. We have not explicitly converted any RM values into angles and so the effect of changing wavelengths between source and observer has not been considered in this work.

## 6.2 Going Forward

This work is a first step in the development of the techniques to detect the magnetic fields associated with the LSS. The error of the structure function arises from the RMS error in each angular distance bin, and so fewer sources in a bin will mean a larger error. More sources would reduce the error and make signal detection much clearer. Thus more sources with better sensitivity would improve the structure coverage, but this limitation is a function of observing area rather than the simulation.

We have overlooked the effect that redshift has on the wavelength of light and, therefore, have probably obtained upper limits on the RM measurements that could be made in observations. Future work could be made more rigorous by exploring this effect.

Another way to detect more structure is to use a larger observing area because more structure could be sampled and at a larger scale. This is computationally possible, but not to the same redshift with this simulation because the 50 Mpc cubes have to be tiled to make the pencil beams and a redshift of one is already at the tiling limit of 9 tiles.

In the MIGHTEE deep observations, the observational noise will have been reduced and so it would be worth processing this project with the deep-field parameters as a further investigation.

In the MUFASA simulations, gas particles are modelled as clumps of material of  $10^7 \text{ M}_\odot h^{-1}$  with smoothing length of a few hundred kpc  $h^{-1}$ . The smoothing kernel ensures that there is no empty space between particles, but higher resolution simulations would make a difference in increasing accuracy since the particles could be modelled as smaller spheres and allow for more structure at smaller scales. This is a computationally expensive process, however, and so such a simulation at this scale will require resources with high memory, processing and time capacity.

# References

- Akahori T., Ryu D., 2010, eprint arXiv, 1009, 570
- Akahori T., Kumazaki K., Takahashi K., Ryu D., 2014, Publ. Astron. Soc. Japan, 66, 65
- Alfvén H., Herlofson N., 1950, Cosmic radiation and radio stars [3], doi:10.1103/PhysRev.78.616, <https://link.aps.org/doi/10.1103/PhysRev.78.616>
- Appel A., 1968, in Proc. April 30–May 2, 1968, spring Jt. Comput. Conf.. pp 37–45
- Beck R., 2011, in AIP Conf. Proc.. pp 117–136 ([arXiv:1104.3749v1](https://arxiv.org/abs/1104.3749v1)), doi:10.1063/1.3635828
- Beck R., Gaensler B. M., 2004, New Astron. Rev., 48, 1289
- Beck R., Wielebinski R., 2013, Planets, Stars Stellar Syst. Vol. 5 Galact. Struct. Stellar Popul., pp 641–723
- Beck R., Brandenburg A., Moss D., Shukurov A., Sokoloff D., 1996, Annu. Rev. Astron. Astrophys., 34, 155
- Bell E. F. E., 2003, Astrophys. J., 586, 794
- Bennett C. L., et al., 2012, ] 10.1088/0067-0049/208/2/20
- Bernet M. L., Miniati F., Lilly S. J., Kronberg P. P., Dessauges-Zavadsky M., 2008, Nature, Vol. 454, Issue 7202, pp. 302-304 (2008)., 454, 302
- Bernet M. L., Miniati F., Lilly S. J., 2013, Astrophys. J. Lett. Vol. 772, Issue 2, Artic. id. L28, 6 pp. (2013)., 772
- Best P. N., Kauffmann G., Heckman T. M., Brinchmann J., Charlot S., Ivezic Z., White S. D. M., 2005, Mon. Not. R. Astron. Soc., 362, 25
- Blumenthal G. R., Faber S. M., Primack J. R., Rees M. J., 1984, Nature, 311
- Bonafede A., Feretti L., Murgia M., Govoni F., Giovannini G., Dallacasa D., Dolag K., Taylor G. B., 2010, Astron. Astrophys., 513, A30
- Bonafede A., et al., 2015, in Adv. Astrophys. with Sq. Km. Array. p. 95 ([arXiv:1501.00321](https://arxiv.org/abs/1501.00321)), <http://arxiv.org/abs/1501.00321>
- Bond J. R., Kofman L., Pogosyan D., 1995, arXiv Prepr. astro-ph/9512141

- Braun R., Walterbos R., 1969, *Astronomy and astrophysics.. Vol. 10, EDP Sciences [etc.],* <http://adsabs.harvard.edu/abs/1985A&A...143..307B><http://adsabs.harvard.edu/abs/1971A%26A....10....76B>
- Brentjens M. A., de Bruyn A. G., 2005, *Astron. Astrophys.*, 441, 1217
- Burn B. J., 1966a, *Mon. Not. R. Astron. Soc.*, 133, 67
- Burn B. J., 1966b, *Mon. Not. R. Astron. Soc.*, 133, 67
- Cantalupo S., Arrigoni-Battaia F., Prochaska J. X., Hennawi J. F., Madau P., 2014, *Nature*, 506, 63
- Caprini C., Durrer R., Fenu E., 2009, *J. Cosmol. Astropart. Phys.*, 2009, 001
- Cassano R., Brunetti G., Venturi T., Setti G., Dallacasa D., Giacintucci S., Bardelli S., 2008, *Astron. Astrophys.*, 480, 687
- Cawood M. R., Roy M., 2014
- Chamandy L., Taylor A. R., 2015, *Astrophys. J.*, 808, 28
- Coil A. L., 2013, in , *Planets, Stars Stellar Syst. Vol. 6 Extragalactic Astron. Cosmol.. Springer Netherlands, Dordrecht*, pp 387–421 ([arXiv:0604561](https://arxiv.org/abs/0604561)), doi:10.1007/978-94-007-5609-0\_8, [http://link.springer.com/10.1007/978-94-007-5609-0\\_8](http://link.springer.com/10.1007/978-94-007-5609-0_8)
- Colless M., et al., 2001, *Mon. Not. R. Astron. Soc.*, 328, 1039
- Colless M., et al., 2003, eprint arXiv:astro-ph/0306581
- Condon J. J., 1988, in , *Galact. Extragalactic Radio Astron.. Springer*, pp 641–678
- Condon J. J., 1992, *Annu. Rev. Astron. Astrophys.*, 30, 575
- Condon J. J., Ransom S. M., 2016, *Essential Radio Astronomy*. Princeton University Press, <https://science.nrao.edu/opportunities/courses/erahttp://press.princeton.edu/titles/10771.html>
- Condon J. J., Cotton W. D., Greisen E. W., Yin Q. F., Perley R. A., Taylor G. B., Broderick J. J., 1998, *Astron. J.*, 8065, 1693
- Cooper B., Price R., 1962, *Nature*, 195, 1084
- Crain R., et al., 2015, *MNRAS*, 450, 1937
- Davé R., et al., 2016, *Mon. Not. R. Astron. Soc.*, 462, 3265
- Davis M., Huchra J., Latham D. W., Tonry J., 1982, *Astrophys. J.*, 253, 423
- Donnert J., Dolag K., Lesch H., Müller E., 2008, *Mon. Not. R. Astron. Soc.*
- Dumke M., Krause M., Wielebinski R., Klein U., 1995, *A&A*, 302, 691
- Durrer R., Neronov A., 2013, *Astron. Astrophys. Rev.*, 21, 1

- ESA Carreau C., 2013, Planck history of Universe, [http://m.esa.int/spaceinimages/Images/2013/03/Planck\\_history\\_of\\_Universe](http://m.esa.int/spaceinimages/Images/2013/03/Planck_history_of_Universe)
- Feain I. J., et al., 2009, *Astrophys. J.*, 707, 114
- Fitzpatrick R., 2008, in , Maxwell's Equations Princ. Electromagn.. Chapt. Electromag
- Folk M., Heber G., Koziol Q., Pourmal E., Robinson D., 2011, in Proc. EDBT/ICDT 2011 Work. Array Databases - AD '11. ACM Press, New York, New York, USA, pp 36–47, doi:10.1145/1966895.1966900, <http://portal.acm.org/citation.cfm?doid=1966895.1966900>
- Gaensler B. M., Haverkorn M., Staveley-Smith L., Dickey J. M., McClure-Griffiths N. M., Dickel J. R., Wolleben M., 2005, ] 10.1126/science.1108832
- Gaensler B., Landecker T., Taylor A., POSSUM Collaboration 2010, in Am. Astron. Soc. Meet. Abstr.. p. 470.13, <http://adsabs.harvard.edu/abs/2010AAS...21547013G>
- Gardner F. F., Whiteoak J. B., 1966, *Annu. Rev. Astron. Astrophys.*, 4, 245
- Ginzburg V. L., Syrovatskii S. I., 1965, *Annu. Rev. Astron. Astrophys.*, 3, 297
- Govoni F., Feretti L., 2004a, ] 10.1142/S0218271804005080
- Govoni F., Feretti L., 2004b, *Int. J. Mod. Phys. D*, 13, 1549
- Grant J. K., Taylor A. R., Stil J. M., Landecker T. L., Kothes R., Ransom R. R., Scott D., 2010
- Grogin N. A., et al., 2011, *Astrophys. J. Suppl. Ser.*, 197, 35
- Hammond A. M., Robishaw T., Gaensler B. M., 2012
- Han J. L., 2004, *Magn. Interstellar Mediu.*, pp 3–12
- Han J. L., Beck R., Berkhuijsen E. M., 1998
- Hey J. S., Parsons S. J., Phillips J. W., 1946, *Nature*, 158, 234
- Hiltner W., 1949, *Science (80-.)*, 109, 165
- Hinders D. C. D. C., Craine W. B., 2014, AP statistics, 2014-2015. [https://books.google.co.za/books?id=8VoUAAAAQBAJ&q=%22standard+error+of+the+slope%22+ti83&dq=%22standard+error+of+the+slope%22+ti83&hl=en&sa=X&redir\\_esc=y](https://books.google.co.za/books?id=8VoUAAAAQBAJ&q=%22standard+error+of+the+slope%22+ti83&dq=%22standard+error+of+the+slope%22+ti83&hl=en&sa=X&redir_esc=y)
- Hoffman Y., Shaham J., 1982, *Astrophys. J.*, 262, L23
- Hogg D. W., 2000, New York, 1, 1
- Hopkins P. F., 2015, *Mon. Not. R. Astron. Soc.*, 450, 53
- Hubble E. P., 1926, *Astrophys. J.*, 64, 321
- Hubble E. P., 1934, *Astrophys. J.*, 79, 8
- Icke V., 1984, *MNRAS*, 206, 1P

- Jansson R., Farrar G. R., 2012, *Astrophys. J.*, 757
- Jarrett T. H., et al., 2016, *Astrophys. Journal*, Vol. 836, Issue 2, Artic. id. 182, 28 pp. (2017)., 836
- Jarvis M., Taylor R., MIGHTEE Collaboration 2017, in *Proc. Sci.*. pp 1–23
- Kaiser N., 1984, *Astrophys. J.*, 284, L9
- Khandai N., Di Matteo T., Croft R., Wilkins S., Feng Y., Tucker E., DeGraf C., Liu M.-S., 2015, *MNRAS*, 450, 1349
- Kim K.-T., Kronberg P. P., Dewdney P. E., Landecker T. L., 1990, *Astrophys. J.*, 355, 29
- Kirshner R. P., Oemler, A. J., Schechter P. L., Shectman S. A., 1981, *Astrophys. J.*, 248, L57
- Klein U., Fletcher A., 2015, Galactic and Intergalactic Magnetic Fields. No. March, Springer International Publishing, Cham, doi:10.1007/978-3-319-08942-3, <http://link.springer.com/10.1007/978-3-319-08942-3>
- Koekemoer A. M., et al., 2011, *Astrophys. J. Suppl.*, 197, 36
- Kolb E., Turner M., 1994, ] 10.1007/978-94-009-4015-4, p. 592
- Krause M., Wielebinski R., Dumke M., 2006a, *Astron. Nachrichten*, 327, 499
- Krause M., Wielebinski R., Dumke M., 2006b, *Astron. Astrophys.*, 448, 133
- Kronberg P. P., Bernet M. L., Miniati F., Lilly S. J., Short M. B., Higdon D. M., 2007, *Astrophys. Journal*, Vol. 676, Issue 1, Artic. id. 70-79, pp. (2008)., 676
- LaValle S. M., 2006, Planning algorithms. Cambridge university press
- Large M. I., Mathewson D. S., Haslam C. G. T., 1959, *Nature*, 183, 1663
- Lazar M., Schlickeiser R., Wielebinski R., Poedts S., 2009, *ApJ*, 693, 1133
- Lazarian A., Pogosyan D., 2015, *Astrophys. J.*, 818, 000000
- Marinacci F., Vogelsberger M., Mocz P., Pakmor R., 2015, preprint ([arXiv:1506.00005](https://arxiv.org/abs/1506.00005))
- Martin D. C., Chang D., Matuszewski M., Morrissey P., Rahman S., Moore A., Steidel C. C., 2014, *Astrophys. J.*, p. 62
- Mauch T., Sadler E. M., 2007, *Mon. Not. R. Astron. Soc.*, 375, 931
- Minter A. H., Spangler S. R., 1996, *Astrophys. J.*, 458, 194
- Naab T., Ostriker J. P., 2016, *Annu. Rev. Astron. Astrophys.*, 55, 59
- Oppermann N., et al., 2015, *Astron. Astrophys.*, 575, A118
- Owen F. N., Morrison G. E., 2008, *Astron. J.*, 136, 1889
- Pakmor R., Springel V., 2013, *Mon. Not. R. Astron. Soc.*, 432, 176

- Peebles P. J. E., 1980, The large-scale structure of the universe. Princeton university press
- Peebles P. J. E., Groth E. J., 1975, *Astrophys. J.*, 196, 1
- Peebles P. J. E., Ratra B., 2002, ] 10.1103/RevModPhys.75.559
- Rees M. J., 2006, *Most*, 398, 395
- Robert Thompson 2017, rthompson / caesar → Bitbucket, <https://bitbucket.org/rthompson/caesar>
- Roth S. D., 1982, *Comput. Graph. Image Process.*, 18, 109
- Ryu D., Kang H., Biermann P. L., 1998, *Astron. Astrophys.*, 335, 19
- Ryu D., Schleicher D. R. G., Treumann R. A., Tsagas C. G., Widrow L. M., 2012, Magnetic fields in the large-scale structure of the universe (arXiv:1109.4055), doi:10.1007/s11214-011-9839-z, <http://arxiv.org/abs/1109.4055> http://dx.doi.org/10.1007/s11214-011-9839-z
- SKA South Africa 2017, SKA Africa, <https://www.ska.ac.za/>
- Salmon B., et al., 2015, *Astrophys. J.*, 799, 183
- Schaye J., et al., 2015, *MNRAS*, 446, 521
- Schneider P., Weiss A., 1988, *Astrophys. J.*, 330, 1
- Schnitzeler D. H. F. M., 2010, ] 10.1111/j.1745-3933.2010.00975.x
- Shapley H., Ames A., 1932, *Ann. Harvard Coll. Obs.*, 88, 41
- Simonetti J. H., Cordes J. M., 1986, *Astrophys. J.*, 310, 160
- Simonetti J. H., Cordes J. M., Spangler S. R., 1984, *Astrophys. J.*, 284, 126
- Simonetti J. H., Cordes J. M., Heeschen D. S., 1985, *Astrophys. J.*, 296, 46
- Sofue Y., Fujimoto M., Wielebinski R., 1986, *Annu. Rev. Astron. Astrophys.*, 24, 459
- Soida M., Krause M., Dettmar R.-J., Urbanik M., 2011, p. 11
- Somerville R. S., Davé R., 2014
- Springel V., 2005, *Mon. Not. R. Astron. Soc.*, 364, 1105
- Springel V., Frenk C. S., White S. D. M., 2006, ] 10.1038/nature04805
- Stasyszyn F., Nuza S. E., Dolag K., Beck R., Donnert J., 2010, *Mon. Not. R. Astron. Soc.*, 408, 684
- Stepanov R., Arshakian T., Beck R., Frick P., Krause M., 2008, *A&A*, 480, 45
- Stil J. M., Krause M., Beck R., Taylor A. R., 2008, *Astrophys. Journal*, Vol. 693, Issue 2, pp. 1392-1403 (2009)., 693, 1392

- Stil J. M., Taylor A. R., Sunstrum C., 2010, *Astrophys. J.*, 726, 4
- Stil J. M., Keller B. W., George S. J., Taylor A. R., 2014, *Astrophys. J.*, 787, 99
- Stokes G. G., 1852, *Philos. Trans. R. Soc. London*, 142, 463
- Sun X. H., et al., 2014
- T. Hey and P. Walters 1988, *The Quantum Universe*. Cambridge University Press, Cambridge, [http://www.ph.unimelb.edu.au/\\$\sim\\$dnj/teaching/160mag/160mag.htm](http://www.ph.unimelb.edu.au/$\sim$dnj/teaching/160mag/160mag.htm)
- Taylor R., Salter C., 2010
- Taylor a. R., Stil J. M., Sunstrum C., 2009, *Astrophys. J.*, 702, 1230
- Taylor A. R., et al., 2015, arXiv Prepr. arXiv1501.02298
- Thompson A. C., Fluke C. J., Barnes D. G., Barsdell B. R., 2010, *New Astron.*, 15, 16
- Trippe S., 2014, *J. Korean Astron. Soc.*, 47, 15
- Vazza F., Brüggen M., Gheller C., Wang P., 2014, *Mon. Not. R. Astron. Soc.*, 445, 3706
- Vogelsberger M., et al., 2014, *Mon. Not. R. Astron. Soc.*, 444, 1518
- Wambsganss J., 1999, *J. Comput. Appl. Math.*, 109, 353
- Zehavi I., et al., 2011, *Astrophys. J.*, 736, 59
- de Lapparent V., Geller M. J., Huchra J. P., 1986, *Astrophys. J.*, 302, L1

# Appendices

# Appendix A

## Data summary

**Table A.1:** Number of objects in each section of the cone

| Section | Gas particles | Galaxies | Halos  |
|---------|---------------|----------|--------|
| 0       | 35097         | 2        | 33     |
| 1       | 276713        | 32       | 327    |
| 2       | 596517        | 23       | 457    |
| 3       | 2592045       | 247      | 2375   |
| 4       | 5083531       | 415      | 4596   |
| 5       | 3467809       | 154      | 2051   |
| 6       | 4433985       | 382      | 4894   |
| 7       | 4853226       | 317      | 4765   |
| 8       | 6580042       | 341      | 4994   |
| 9       | 10600536      | 762      | 9825   |
| 10      | 17745010      | 1464     | 15981  |
| 11      | 29192830      | 1749     | 16152  |
| 12      | 36402064      | 2206     | 25077  |
| 13      | 37426949      | 3753     | 39373  |
| 14      | 49314064      | 3700     | 25197  |
| 15      | 52036660      | 2650     | 43773  |
| 16      | 55667882      | 1997     | 25882  |
| 17      | 59914857      | 2481     | 33279  |
| 18      | 69630388      | 3918     | 50193  |
| 19      | 87207710      | 7162     | 83842  |
| 20      | 103061724     | 8268     | 100511 |
| 21      | 108910977     | 7757     | 95061  |
| 22      | 129447021     | 8493     | 106703 |
| 23      | 147308138     | 9518     | 118975 |
| 24      | 174071417     | 11092    | 139501 |
| 25      | 197547639     | 12745    | 158389 |
| 26      | 204237050     | 12973    | 163943 |
| 27      | 222876694     | 14483    | 191801 |
| 28      | 248541639     | 15887    | 211390 |
| 29      | 269034862     | 15918    | 213343 |
| 30      | 273954962     | 14093    | 186352 |
| 31      | 311210583     | 17536    | 232031 |

Table A.1: continued from previous page

| Section | Gas particles | Galaxies | Halos  |
|---------|---------------|----------|--------|
| 32      | 339293388     | 21425    | 289159 |
| 33      | 394057665     | 25905    | 359476 |
| 34      | 396177449     | 30588    | 419349 |
| 35      | 460784919     | 29660    | 418608 |
| 36      | 476560764     | 27790    | 389777 |
| 37      | 524934064     | 30156    | 436766 |
| 38      | 640156006     | 38528    | 558447 |
| 39      | 706490650     | 41048    | 599081 |
| 40      | 751110300     | 39228    | 576146 |
| 41      | 667782206     | 34390    | 517992 |
| 42      | 779346966     | 43593    | 662597 |
| 43      | 834647312     | 45251    | 693665 |
| 44      | 746506430     | 41872    | 659735 |
| 45      | 939531811     | 55172    | 865924 |